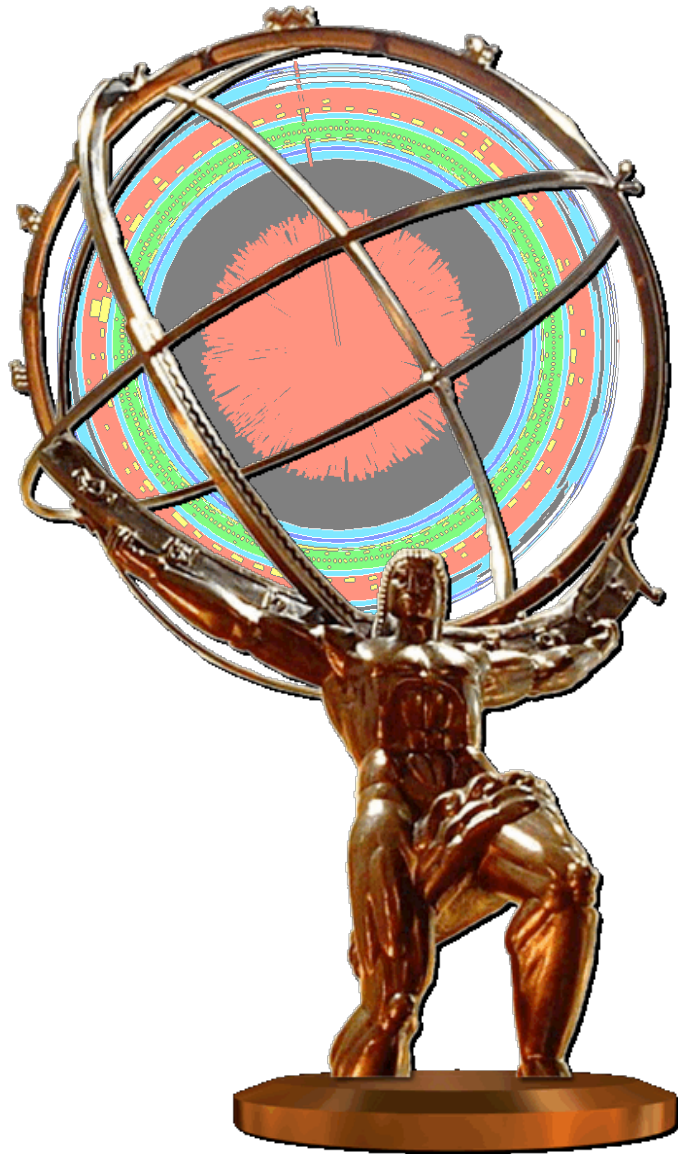


Heavy Ion Physics with the ATLAS Detector at the LHC



Heavy Ion Physics with the ATLAS Detector at the LHC

ATLAS Heavy Ion Working Group

M.D. Baker, R. Debbe, P. Nevski, P. Steinberg, H. Takai, F. Videbaek, S. White

*Physics Department, Brookhaven National Laboratory,
Upton, NY 11973*

B. Wosiek, A. Trzupek, K. Wozniak, A. Olszewski, B. Tocsek

Physics Department, IFJ PAN Krakow, Poland

L. Rosselet

Physics Department, University of Geneva, Switzerland

W. Brooks

Physics Department, Santa Maria University, Valparaiso, Chile

S. Timoshenko

Physics Department, MePHI, Moscow, Russia

V. Pozdynakov

Physics Department, JINR, Dubna, Russia

S. Milov, I. Tserruya

Physics Department, Weizmann Institute, Rehovot, Israel

S. Bathe

*RIKEN/BNL Research Center, Brookhaven National
Laboratory, Upton, NY 11973*

A. Angerami, B. Cole, N. Grau, W. Holzmann

*Physics Department, Columbia University and Nevis Laboratories,
Irvington, NY 10053*

J. Hill, A. Lebedev, M. Rosati

Physics Department, Iowa State University, Ames, IA 50011

A. Ajitanand, P. Chung, J. Jia¹, R. Lacey
Chemistry Department, Stony Brook University, Stony Brook, NY 11794

(December 10, 2008)

¹Also *Physics Department, Brookhaven National Laboratory, Upton, NY 11973.*

Abstract

The ATLAS experiment will participate in the Heavy Ion program at the Large Hadron Collider (LHC) and will use its large acceptance, high granularity calorimeters, silicon tracking detectors, and muon spectrometers to study hard scattering processes and jet quenching, quarkonia production and suppression, and global observables in Pb+Pb collisions. The longitudinal and fine transverse segmentation of the ATLAS electromagnetic calorimeter gives ATLAS unique capabilities for measuring complete jets and photons. Brookhaven National Laboratory, Columbia University, Iowa State University, and Stony Brook University propose a focused program to take advantage of ATLAS's strengths to study the physics of high-energy parton interactions with the quark-gluon plasma (QGP), the physics of Debye screening of $Q\bar{Q}$ states in the QGP, and the physics of initial particle production and thermalization to characterize the properties of the QGP created in heavy ion collisions at the LHC. The proposed program can be accomplished for modest cost, will provide substantial physics impact and will have a positive impact on the physics program at the Relativistic Heavy Ion Collider (RHIC) due to the strong involvement of the proposing institutions in the RHIC program. Participation of US groups will strengthen the existing (and growing) ATLAS heavy ion program by bringing physics and analysis expertise developed at RHIC and will allow the US Nuclear Physics program to participate in an experiment that will have substantial physics impact on the heavy ion community.

Contents

Abstract	1
1 Heavy Ion Physics at the LHC	1
1.1 The Search for the Quark Gluon Plasma: from SPS to RHIC	1
1.2 Bulk Properties of Heavy Ion Collisions through RHIC energies	2
1.3 Prospects for the LHC	7
1.4 ATLAS detector	9
1.5 ATLAS Heavy Ion program	10
1.6 Connection with RHIC and RHIC-II programs	13
1.7 Proposal structure - UNDER CONSTRUCTION	13
2 Simulations tools and Heavy ion detector occupancies	15
3 Tracking in ATLAS	16
3.1 Tracking heavy ion events with the ATLAS detector at the LHC	16
3.2 Inclusive charged particle spectra	16
3.3 Vertex reconstruction	19
4 Forward Instrumentation	21
4.1 The ATLAS Zero Degree Calorimeter	21
4.2 Physics Motivation	21
4.3 ZDC design	22
4.4 Triggering in Pb+Pb	23
4.5 Low- x physics in Pb+Pb and p+Pb with UPC	25
4.6 Physics Topics in pp Data	26
4.7 Connections to cosmic ray physics	26
4.8 Physics with forward neutrons in ATLAS	27
4.9 UPC in Pb-Pb	27
4.10 p-Pb	28
4.11 pp	29
4.12 Operations issues	30
4.13 Summary	31

5	Global Variables	33
5.1	Global physics at the LHC	33
5.2	ATLAS capabilities	36
5.3	Determination of the collision centrality	37
5.4	Charged particle multiplicity measurements	38
5.5	Transverse energy measurements	41
5.6	Elliptic flow	42
5.7	Summary	51
6	Jet Reconstruction	52
6.1	Physics motivation	52
6.2	ATLAS calorimeter and jet measurements	57
6.3	Jet reconstruction in Pb+Pb collisions with ATLAS	58
6.4	Jet reconstruction performance	61
6.5	Jet Fragmentation	67
6.6	Di-jet correlations	68
6.7	Heavy quark jet reconstruction	69
6.8	Summary	72
7	Jet Quenching	73
7.1	Recent predictions of jet quenching	73
7.2	Jet description	74
7.3	Illustrative quenching	74
8	Quarkonia	75
9	Z	76
9.1	Physics motivation	76
9.2	Introduction	76
9.3	Z^0 mass resolution.	76
9.4	Acceptance times efficiency.	77
9.5	Expected rates and yields	77
9.6	Summary	77
10	Direct Photons & Photon-Jet Correlations	81
10.1	Physics motivation	81
10.2	Photon identification	82
10.3	Isolation cuts	86
10.4	Combined photon identification and isolation cuts	88
10.5	Rate estimate	89
10.6	Photon-jet correlations	90
10.7	Unique ATLAS capabilities	91
10.8	Summary	93

11 Trigger & DAQ	94
11.1 ATLAS data acquisition system	94
11.2 Pb+Pb conditions	95
11.3 Pb+Pb minimum bias triggers	96
11.4 Rare signal triggers	97
11.5 Pb+Pb jet and photon triggers	97
11.6 Summary	103
12 Summary	104

Chapter 1

Heavy Ion Physics at the LHC

1.1 The Search for the Quark Gluon Plasma: from SPS to RHIC

The RHIC physics program has had as its goal from the very early days of the collider and detector design to identify the “Quark Gluon Plasma” (QGP) predicted by both perturbative and lattice QCD [1] and to study its properties. The idea was to use the high energies and high densities provided by the collider environment to induce large momentum transfers between nucleon constituents, leading to weaker interactions, and thus a “deconfinement” of hadronic constituents. This was thought to lead to an enormous jump in entropy (e.g. via a first-order phase transition) with observable consequences, e.g. large multiplicities, large source sizes, and changes in thermal properties of observed particle distributions. At the same time, knowledge of hadronic structure functions and perturbative cross sections led to the prediction that jets could be produced, even at the “low” (on collider scales) RHIC energies, but would be subsequently quenched by the presence of a deconfined medium.

The RHIC data appeared very rapidly after the machine started providing physics events in 2000, with the PHOBOS measurement of the charged-particle multiplicity at mid-rapidity. This was found to be on the low side of the range of predictions available at the time, which was characteristic of models with a limited role of hard processes as contributing to the total entropy. The inclusive measurements were quickly complemented by identified particle spectra and interferometric measurements, which found the particle source to be surprisingly similar to that found at lower energies. However, global measurements which characterized the collective flow of the system found that it was expanding as rapidly as ideal hydrodynamics would predict, suggestive that the system was in fact strongly-interacting, rather than weakly. At the same time, measurements of particles reflecting hard processes (e.g. high p_T hadrons) found that these were not produced according to N_{coll} scaling reflecting the small scales probed by large momentum transfers. This supported the interpretation that the medium was dense and absorptive, which was further confirmed by two particle correlations showing the disappearance of back-to-back hadrons.

The following sections will highlight examples of RHIC data that are thought to characterize features of the dynamical evolution of the system, and which point to the LHC as the natural way to extend our knowledge of the microscopic basis of the dynamics.

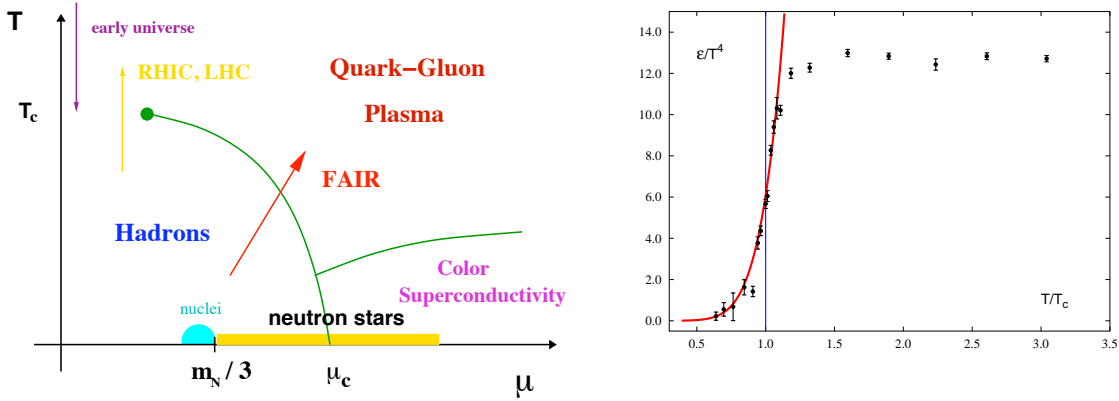


Figure 1.1: (left) Schematic phase diagram of hot nuclear matter (right) Lattice calculations showing the sudden jump in the effective number of degrees of freedom (ϵ/T^4) at T_c .

1.2 Bulk Properties of Heavy Ion Collisions through RHIC energies

1.2.1 Initial State

Conceptions of the initial state of heavy ion collisions generally fall into two classes: those which try and understand the nature of the nuclear wave function by the properties of QCD, and more phenomenological descriptions based on initial conditions for hydrodynamic calculations.

The nuclear wave function is currently understood as manifesting a “Color Glass Condensate” (for a review, see Ref.[2]) This is a high-density configuration of the predominantly low- x gluons which are produced at large beam energies. The interplay between the standard perturbative splitting diagrams are balanced by recombination diagrams at high enough densities, leading to the generation of a “saturation scale” Q_s (usually specified as Q_s^2) which characterizes the local gluon density (for a recent review, see Ref.). Regardless of whether the CGC is a proper new state of matter, it is certainly a qualitatively new regime of QCD. The techniques used to calculate incorporate classical gluon fields, indicate that it is no longer simple perturbative physics that dominates. To date, circumstantial evidence supporting the presence of a saturated initial state has been identified in low particle multiplicities in A+A[3], suppressed forward yields in d+Au, and possibly long-range rapidity correlations. More importantly, it is expected to play an even stronger role at the LHC, as the nuclear PDFs are probed down to much lower x than at RHIC.

The role of the initial state wave function is intimately connected with the dynamics of energy deposition and thermalization in the nuclear collision, a major frontier of RHIC physics. The development of many of the features of RHIC collisions, to be covered in the next sections, are now seen to be dynamical in origin. This is exemplified by the relevance of hydrodynamical behavior, which is presumably generated by strong local interactions in the dense system. It then becomes an overwhelmingly important question exactly how the system develops until the hydrodynamic limit is reached, both in the sense of which degrees of freedom are active at early times, and the theory which govern them. This should also give insight into what the relevant energy density ϵ might be as the system achieves local thermalization.

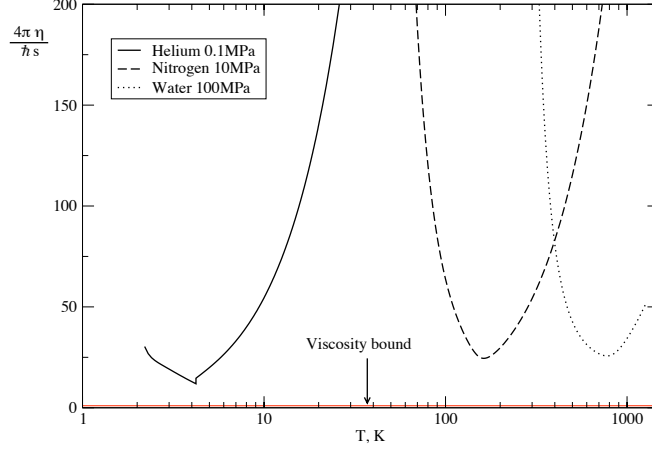


Figure 1.2: The viscosity to entropy ratio (η/s) compared to a variety of macroscopic physical systems.

The role of microscopic phenomena in the sQGP should be made manifest by measurements of its viscosity. One interesting expectation is that the system formed at RHIC is not exactly a perfect fluid, as suggested by hydrodynamic calculations, but a near-perfect one. In fact, calculations involving 10 dimensional black holes have been made and mapped onto field theory calculations using the “AdS/CFT Correspondence”. These show that the fluid has a minimal shear viscosity, characterized by $\eta/s \geq 1/4\pi$ [4]. This so-called viscosity bound, illustrated in Fig.1.2 has been derived by more standard considerations combining kinetic theory with quantum mechanics, suggesting that a system can be in equilibrium on scales no shorter than the thermal wavelength of its constituents. However, it is generally thought that the string theory calculations are somehow encoding the same quantum mechanical arguments, but in a classical gravity calculation. This again emphasizes the more general relevance of the study of the early stages of heavy ion collisions, either by direct probes of its microscopic dynamics, or via the evolution of bulk observables, to address one of the only known phenomenological applications of string theory.

Once the system is thermalized, then lattice QCD calculations are thought to be the relevant theoretical tool to understand the bulk properties of the medium, especially the equation of state (EOS). A typical lattice EOS is shown in the right panel of Fig.1.1 and shows the evolution of the quantity ϵ/T^4 , which counts the thermodynamically averaged degrees of freedom. It shows both that there is a rapid transition at a “critical temperature” around $T_c \sim 170 \text{ MeV}$ (recently raised to $T = 192 \text{ MeV}$ [?]) and that the number of degrees of freedom no longer changes in any significant way with temperature. The details of this transition, both in terms of degrees of freedom, and especially in terms of the evolution of bulk quantities like energy density and pressure, are expected to have quantifiable effects on the dynamical evolution of the system, especially if it evolves hydrodynamically.

At the same time, there is some suspicion that perturbative calculations using Hard Thermal

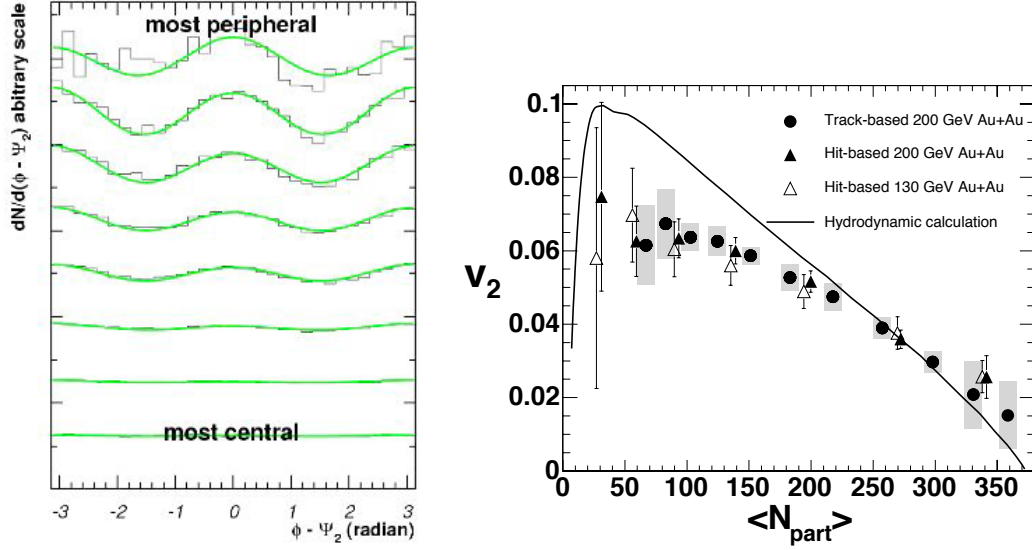


Figure 1.3: (left) Azimuthal modulation of charged particle production relative to the reaction plane (right)

Loops are able to describe the temperature dependence of the bulk variables measured on the lattice between $T \geq 2 - 3T_c$ [?]. This in principle could lead to relevant transport calculations for the dynamics of the fluid, especially at the LHC where momentum transfers will be high. However, calculations which transport individual particles that interact via perturbative cross sections are unable to generate sufficient pressure unless they artificially enhance the cross sections.

1.2.2 Elliptic Flow

If heavy ion collisions indeed form a collective system which is in local thermal equilibrium then the details of microscopic dynamics will not be important for the development of the system. Rather the “bulk” of the system (by which is meant the average behavior of typical particles) will reflect only macroscopic features of the collision, whether it be the energy and geometry of the initial state.

The azimuthal distributions of inclusive charged particles (as well as transverse energies) have been found to show a strong event-wise modulation, shown for PHOBOS data in the left panel of Fig.1.3 This is characterized by the second Fourier coefficient $v_2 = \langle \cos(2[\phi - \Phi_{RP}]) \rangle$, where Φ_{RP} is the angle of the reaction plane or event plane. RHIC measurements have compared well do calculations performed under the assumptions of ideal hydrodynamics (zero viscosity) and shown in Fig. The value of v_2 at RHIC is about three times larger than achievable with hadronic models (under the assumptions that hadronic size scales limit the formation time), already suggesting that the flow must be built up when the system is decidedly pre-hadronic in nature. Even with this simple measurement, which requires only a choice of energy density (ϵ) at a chosen thermalization time τ_0 , one can test to see how far down in collision centrality (or volume) the assumption of early local equilibrium extends. With more differential measurements, it is possible to test various

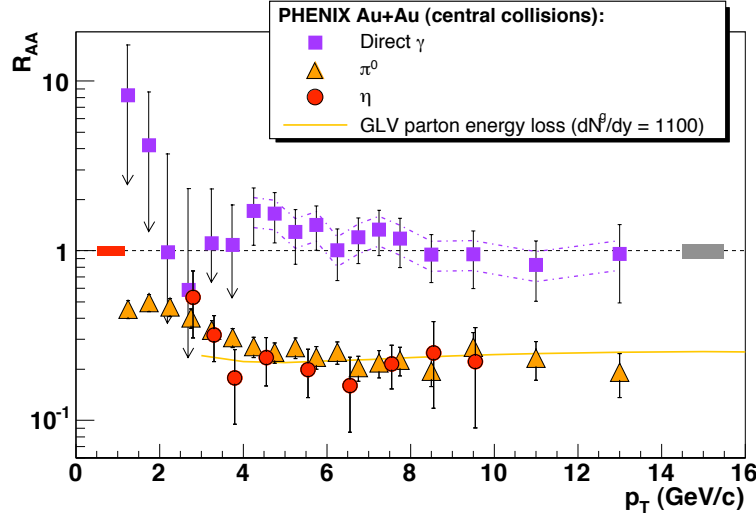


Figure 1.4: Nuclear suppression factor R_{AA} measured by PHENIX for photons, π^0 and η particles.

hypotheses about the degree of thermalization as well as the equation of state, either phenomenological or derived from lattice calculations. It is also possible to quantitatively extract estimates of the η/s ratio using the elliptic flow data data from different channels (e.g. heavy flavor)[5].

1.2.3 High p_T Suppression of Jet Fragments

Another means to probe the microscopic origins of the bulk dynamics is to study “hard probes,” physics processes resulting from large momentum transfers of quarks and gluons, to see if the nuclear environment produces different results than nucleon-nucleon systems. In this context, the latter is treated as a “null hypothesis”, where it is assumed that no medium effects are present. QCD factorization theorems predict that every binary collision of two nucleons has an equivalent chance of inducing a hard process. Under this assumption, one can calculate the nuclear modification factor:

$$R_{AA} = \frac{dN/dp_T|_{AA}}{\langle T_{AB} \rangle d\sigma/dp_T|_{pp}}$$

[Need discussion of how R_{AA} is connected to \hat{q} .

PHENIX data for identified π^0 and η have measured this quantity out to $p_T = 20$ GeV, which is shown in Fig for central events. One sees that R_{AA} is approximately constant at ~ 0.2 above 5 GeV both for π^0 and η . As a comparison probe, PHENIX also shows the normalized yield of direct photons, which should be unaffected by the strongly-interacting medium and simply reflect the incoming parton flux. As expected, the direct photons (out to 12 GeV) scale approximately with the number of binary collisions, ruling out large initial state effects.

The overall constancy of R_{AA} at high p_T suggests a geometric origin to the exact values. This has been explored by studies of correlations between high p_T hadrons, which utilize the fact that energetic hadrons are typically produced back-to-back, e.g. in proton-proton and deuteron-gold collisions, simply as a result of local energy momentum conservation. STAR found a dramatic dis-

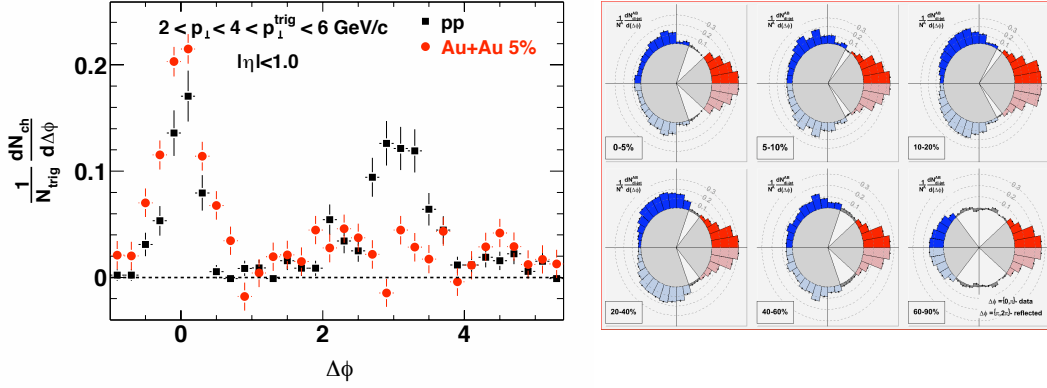


Figure 1.5: (left) Back-to-back suppression measured by STAR for trigger particles of 4 GeV and associated particles of 2.5 GeV (right) Away side modification measured by PHENIX in Au+Au reactions.

appearance of the “away side” ($\Delta\phi \sim 180^\circ$) for trigger hadrons of 4 GeV and associated hadrons of 2 GeV[6]. They also observed that the “near side” ($\Delta\phi \sim 0^\circ$) was essentially unmodified in yield or width. Together, these suggested that high p_T hadrons came from jets that fragmented near the surface of the collision region. The jets that pointed inwards were essentially absorbed completely, disappearing for the particular cuts in this figure. Assuming emission off of collisions happening near the surface was a straightforward way to explain the constant R_{AA} value at approximately the value expected by N_{part} scaling, since $N_{coll} \propto A^{4/3}$ and dropping one radial dimension ($R \propto A^{1/3}$) leads to $A^{4/3}/A^{1/3} \sim A \sim N_{part}$.

Subsequent studies of hadron correlations found an interesting effect when considering the correlation of low p_T associated particles with the high p_T trigger particle. While peripheral events show a clear “back to back” recoil of the soft particles against the hard trigger particle, more central events find a relative minimum at $\Delta\phi \sim \pi$ and two peak structures $60 - 80^\circ$ off axis[?]. Using three particle measurements, this double hump structure has been interpreted as a “Mach Cone” structure, reflecting difference between the speed of sound in medium and the speed of light (typical of hard probes)[7]. In any case, it shows a non-trivial interaction of the recoiling parton with the medium, modifying its fragmentation properties, perhaps so much that all that is predominantly observed is the conservation of energy momentum.

A major outstanding issue remaining from these studies is a quantitative determination of the transport coefficient \hat{q} which reflects the energy broadening of a fast probe via radiating gluons. The jet energies probed at RHIC so far appear to be low enough that jets pointing into the bulk are completely absorbed. This occurs in some calculations for a very large range in \hat{q} , meaning that R_{AA} measurements in themselves offer limited sensitivity to information about the local density. Of course, what sensitivity remains has been fully exploited by the RHIC experiments, in particular an analysis by PHENIX using several existing jet quenching calculations[8], an example of which is shown in Fig. [?]. There is some discussion of whether the return of back-to-back correlated hadrons at very high trigger *and* associated p_T is indicative of a “punch-through” phenomenon (i.e. no interaction going through medium)[9]. However, it is found that the forward

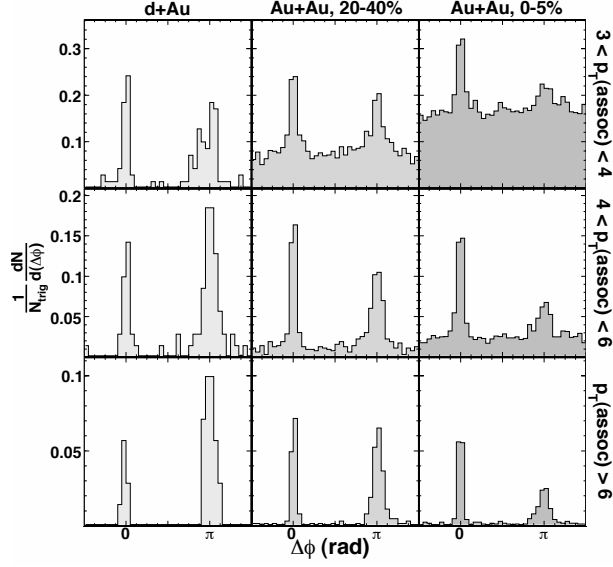


Figure 1.6: Return of back-to-back emission at high p_T measured by STAR.

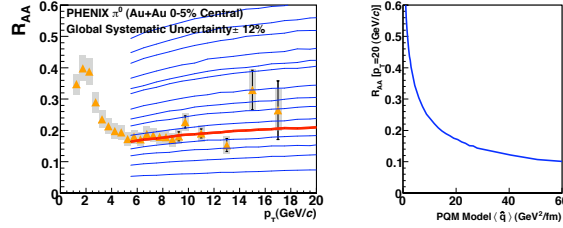


Figure 1.7: Quantitative analysis of \hat{q} using high p_T suppression data, from PHENIX.

and away fragmentation properties are both consistent with hadronization in vacuum, which suggests minimal passage through matter. This may be the result of tangential emission, where the primary hard process is formed on the edge of the reaction zone and neither parton is aimed directly into the bulk.

1.3 Prospects for the LHC

The start of the LHC Heavy Ion program in 2009 or 2010 will surely produce as dramatic a revolution in the study of the quark-gluon plasma in the laboratory as RHIC produced when it first started operation in 2000. Pb+Pb collisions at the LHC are expected to produce a quark gluon plasma with initial energy density roughly an order of magnitude larger than at RHIC [10, 11], with larger ($\times 2$) initial temperatures [10] and longer lifetimes ($\times 1.5$) for the QGP [10] than achieved at RHIC. The increase in the collision energy from RHIC to the LHC will provide a critical test of the application of saturation-inspired models in the description of a particle mul-

tiplicities (see section ??). Measurements of elliptic flow resulting from the higher initial energy densities will test our interpretation of elliptic flow results from RHIC.

Arguably, the most important component of the LHC heavy ion program will be the measurements of jet quenching and the use of jets as a tomographic probe of the medium. The increase in hard scattering cross-sections between the top RHIC energy ($\sqrt{s_{NN}} = 200$ GeV) and the LHC ($\sqrt{s_{NN}} = 5.5$ TeV for Pb+Pb) [12] will extend the p_T range accessible in quenching measurements by at least a factor of 10. For example, a single Pb+Pb run at design luminosity will produce nearly a million jets with $E_T > 100$ GeV [12]. As a result of the copious production of high-energy jets at the LHC, full jet measurements will finally be possible in Pb+Pb collisions, and these measurements should dramatically improve the understanding of jet quenching mechanisms. The energy loss bias will be reduced to the extent that a high-energy quenched jet should still be reconstructed, even if radiative energy loss produces a re-distribution of energy within the jet [13]. Direct measurement of the modified fragmentation functions of the jets [14] will provide more detailed tests of energy loss calculations, thereby reducing the current theoretical ambiguities and improving the utility of quenching measurements as probes of the QGP. Measurement of the inclusive jet E_T spectrum will, in principle, provide sensitivity to collisional energy loss [15, 16] as well as exhibit effects from non-perturbative energy loss that might transfer radiated energy to the medium [17]. The statistics for bottom and charm jets will be sufficient to perform detailed measurements of heavy quark quenching at high E_T . The rate for hard photon-jet processes will be sufficient to allow measurements of photon-tagged jet quenching for photon and jet transverse energies up to 100 GeV. Measurement of the acoplanarity of di-jet pairs at the LHC should provide sensitivity to the expected angular diffusion of high- p_T partons in the medium – an unavoidable consequence of radiative and collisional energy loss [18] that has, so far, eluded detection at RHIC. The large rates for jets will make possible the measurement of all of the above observables as a function of collision centrality, angle with respect to the event plane, and pseudo-rapidity. Taken together, these measurements will provide a degree of sensitivity to the physics of jet quenching that will be difficult to achieve at RHIC. Hard-scattered quarks and gluons may be the only probes that we have that are directly sensitive to the nature of the interactions in the medium. Thus, an improved understanding of the physics of quark and gluon interactions with the medium is essential; full jet measurements at the LHC are the most likely means to accomplish this goal.

The LHC will also provide a new opportunity to explore the physics of deconfinement through the measurement of both charm and bottom quarkonium states. In particular, the ability to measure $b\bar{b}$ quarkonia states has the potential to dramatically improve the current confused situation with experimental probes of deconfinement. Bottom production requires a Q^2 roughly a factor of ten larger than that required for charm production so the production process is harder and, in principle, more amenable to pQCD calculation though theoretical uncertainties in how $b\bar{b}$ pairs evolve into Y states persist. The relative yield of the Y and Y' states is expected to be closer than the yields of ψ and ψ' [19] making comparison of states with different nominal screening scales easier. Also, recent analyses of the temperatures at which the different quarkonia states melt [20] show that that the Y is the only state that survives to $2T_c$. The relatively low multiplicity of $b - \bar{b}$ pairs in Pb+Pb collisions at the LHC is expected to give little recombination contribution to production of Y states [19]. Thus, while it would be naive to assume that Y measurements will be completely free of complications, there is good reason to expect that the measurement of Upsilon production and suppression at the LHC will significantly advance the understanding of Debye screening/deconfinement in the QGP. Certainly, the Y states provide the first new experimental

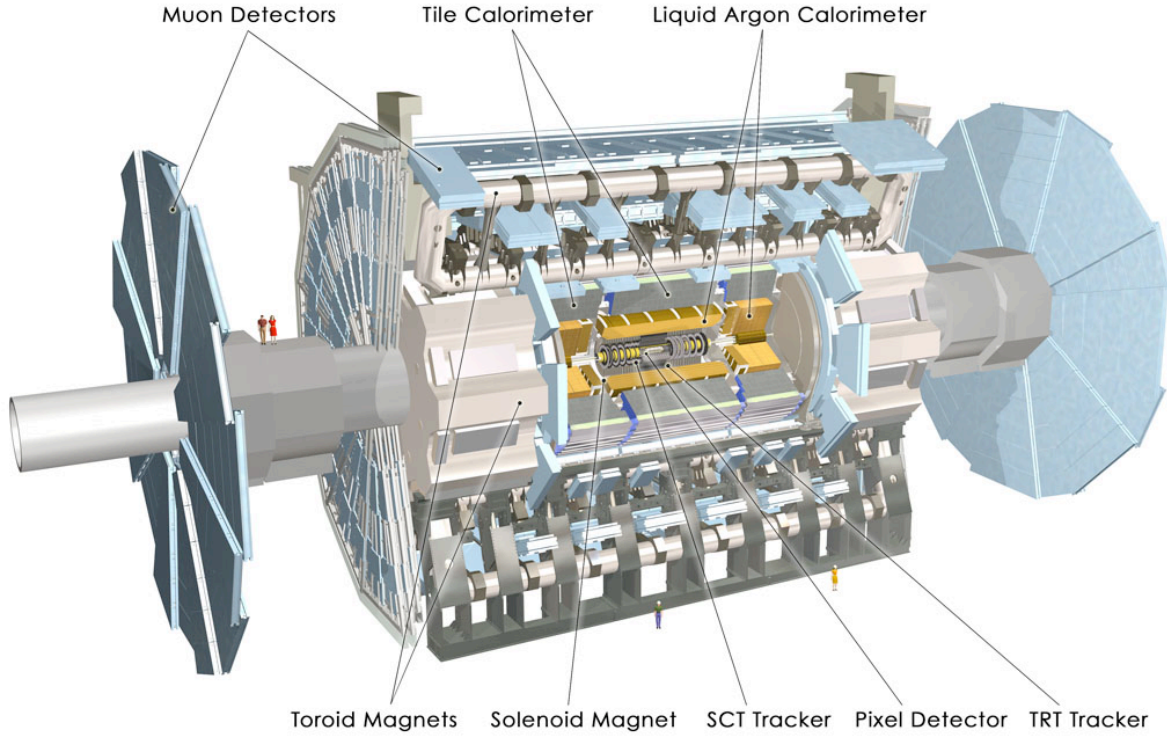


Figure 1.8: The ATLAS detector at the LHC

tool for studying Debye screening in the QGP since the advent of J/ψ suppression measurements in NA38 nearly two decades ago [21].

1.4 ATLAS detector

Figure 1.8 provides a schematic view of the ATLAS detector showing all major detector components. The detector can be viewed as having three largely independent detector systems: the inner detector, the calorimeters, and the muon spectrometers. The inner detector consists of silicon pixel (Pixel), silicon strip (SCT), and transition radiation tracker (TRT) detectors. The calorimeter system consists of barrel and end-cap liquid argon electromagnetic calorimeters, a traditional hadronic calorimeter (Tile Calorimeter), end-cap liquid argon hadronic calorimeter, and forward EM and hadronic calorimeters. The muon spectrometers consist of toroidal magnets and tracking detectors covering both the barrel and end-cap regions of the detector.

The pseudo-rapidity coverage of the ATLAS detector broken out into its various detector components is shown in Fig. 1.9. The ATLAS calorimeters allow measurement of jets over the pseudo-rapidity interval $|\eta| < 5$, identified photons over the interval $|\eta| < 2.4$ and charged particles over the interval $|\eta| < 2.5$. The muon spectrometers, covering $|\eta| < 2.7$ allow measurement of Y states over a range $|\eta| < 3.5$. A forward luminosity monitoring detector will provide $dN_{ch}/d\eta$ measurements over $5.4 < |\eta| < 6.1$. The ATLAS ZDC (see Chapter ??) will cover $|\eta| > 8$ for neutral particles, both neutrons and photons.

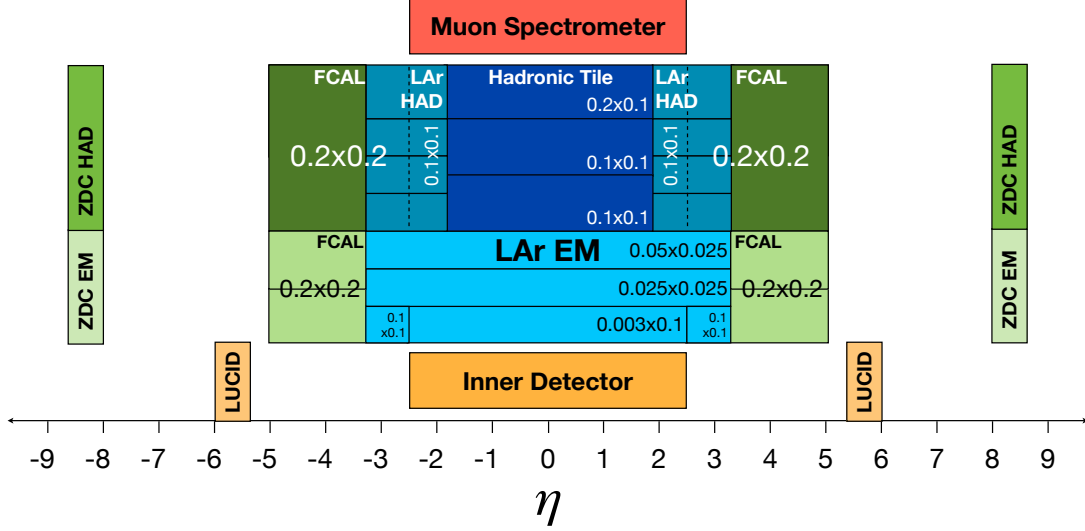


Figure 1.9: The pseudo-rapidity coverage of various components of the ATLAS detector by layer.

One of the unique components of the ATLAS detector relevant to this proposal is the liquid argon electromagnetic calorimeter shown in a diagram of the full ATLAS calorimeter system in Fig. 1.10. The electromagnetic calorimeter, broken into separate “Barrel” and “End-cap” sections as shown in Fig. 1.10, is longitudinally segmented into three layers with the first layer consisting of “strips” that are finely segmented in the η direction ($\Delta\eta \approx 0.003$). This fine segmentation of the first EM sampling layer extends over $|\eta| < 2.4$ and provides valuable separation between single photons and photon pairs produced in neutral hadron (primarily π^0 and η) decays. Because of the fine segmentation of the first sampling layer, this separation can be utilized for neutral hadron transverse momenta as large as 100 GeV/c (see Chapter ??). The longitudinal segmentation of the EM calorimeter allows for improved compensation and provides the best intrinsic jet energy resolution of the detectors at the LHC. The clear advantages of the ATLAS calorimeters for performing jet, di-jet, γ -jet, etc. measurements and the importance of the jet quenching measurements at the LHC provides an overwhelming case for ATLAS participation in the LHC heavy ion program.

1.5 ATLAS Heavy Ion program

ATLAS first started serious discussions regarding participating in the LHC heavy ion program in 2001. In the Spring of 2004, ATLAS submitted a Letter of Intent to the LHC Experiments Committee (LHCC) [22] proposing a heavy ion program that would focus on global observables and hard probes (jets, photons, and quarkonia). The eventual decision by the ATLAS experiment to participate in the LHC heavy ion program was motivated by the fact that the ATLAS detector has several advantages in carrying out heavy ion measurements – especially in the measurement of jets and photons.

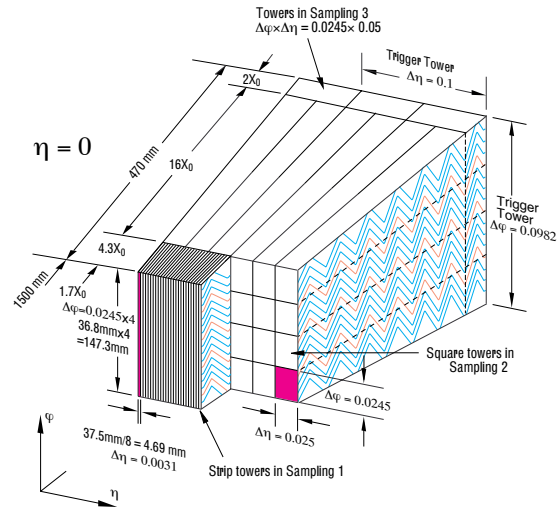
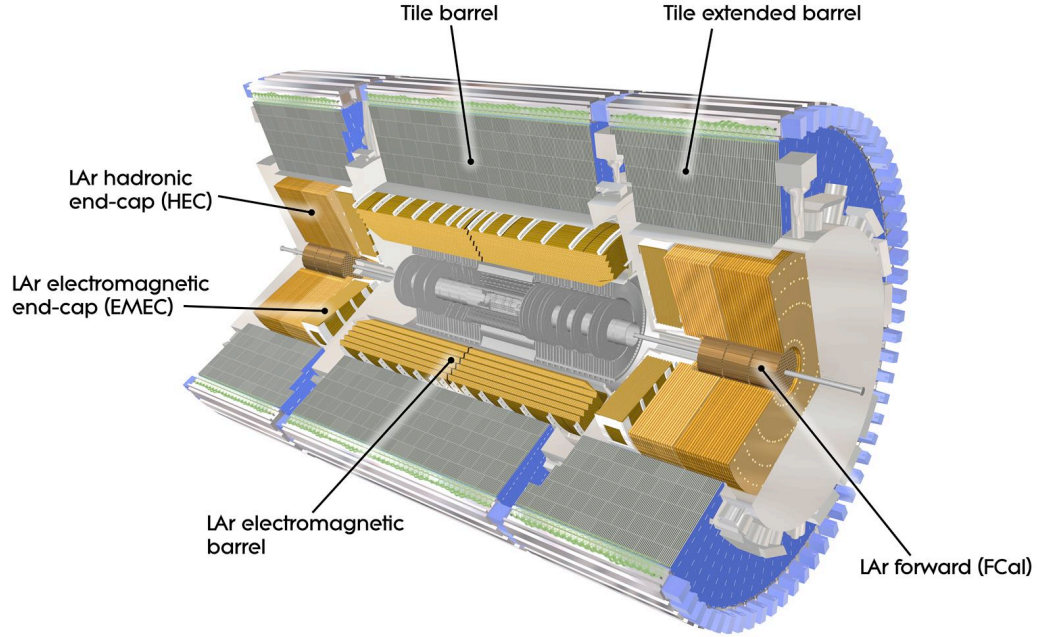


Figure 1.10: (top) Diagram of the ATLAS calorimeter system (bottom) Diagram showing longitudinal segmentation of ATLAS electromagnetic calorimeter.

- Large acceptance, high quality electromagnetic and hadronic calorimeters with fine transverse segmentation and longitudinal segmentation.
- Nearly hermetic external muon spectrometers.
- High precision silicon inner detector.
- High-rate trigger and data acquisition system designed for triggering on rare, high- p_T particles/jets.

On receiving positive encouragement from the LHCC, ATLAS made heavy ion measurements an official part of the ATLAS scientific program and established a Heavy Ion working group to carry out the goals described above.

This document describes a plan by institutions in the US and Europe to take advantage of the unique strengths of the ATLAS detector to pursue a focused study of hard processes in heavy ion collisions at the LHC with the goal of using jet quenching and quarkonia measurements to provide detailed, quantitative information about the properties of the quark-gluon plasma created in heavy ion collisions at the LHC. To accomplish this goal, we will also participate in measurements of global observables in Pb+Pb collisions as these will be essential for constraining bulk properties of the medium and providing reaction plane measurements that will be essential for performing differential measurements of quenching as a function of path length in the medium [23]. We will also participate in p+p measurements as needed to provide the necessary baseline measurements for the Pb+Pb program

We plan to participate in first measurements of charged particle $dN_{ch}/d\eta$, $dE_T/d\eta$ and charged particle, electromagnetic and hadronic elliptic flow in Pb+Pb collisions at the LHC. The $dN_{ch}/d\eta$ measurements will be performed over the range $|\eta| < 2.5$ and $5.4 < |\eta| < 6.1$. The electromagnetic $dE_T/d\eta$ measurements will be performed over the range $|\eta| < 3.2$ while the total $dE_T/d\eta$ measurements will be performed over the range $|\eta| < 5$. Charged particle v_2 measurements will be made over the pseudo-rapidity interval $|\eta| < 2.5$ while calorimetric v_2 measurements will be performed over the range $|\eta| < 5$.

We will measure jet energy spectra, jet charged particle fragmentation functions, jet charged particle j_T distributions, jet shapes, and di-jet angle and energy correlations to separately quantify collisional and radiative energy loss of hard-scattered partons in the quark-gluon plasma. We will use a combination of muon tagging and displaced vertex tagging to separately measure bottom and charm quark energy loss. A combination of direct photon identification and photon isolation will be used to perform high-statistics measurements of prompt photon production and γ -jet pairs to calibrate and further improve the precision of the jet quenching measurements and to extend jet measurements to low E_T . We propose to use the unique capabilities of the ATLAS electromagnetic calorimeter to statistically measure prompt photons down to and possibly below 10 GeV with the goal of detecting jet-conversion photons and medium-induced photon bremsstrahlung associated with jets. The wide calorimetric coverage and tracking coverage of the ATLAS detector will be used to study the medium response to the passage of high energy jets with the goal of clarifying the exciting, but poorly understood jet modifications observed at RHIC. We will make all of the above measurements as a function of collision centrality, angle with respect to the event reaction plane, and pseudo-rapidity. We will measure jets over the pseudo-rapidity range $|\eta| < 5$, photons over the range $|\eta| < 2.4$, and charged hadron fragmentation over the range $|\eta| < 2.5$.

The quarkonia portion of the proposed program focuses on measurement of Upsilon (Y) over the pseudo-rapidity range $|\eta| < 3.5$ with sufficient mass resolution to resolve the Y and the Y' states. The Y and Y' measurements will, by themselves, provide a direct probe of Debye screening of quarkonium states. Direct photon, Z , single muon, and muon tagged jet measurements will provide benchmarks for Y suppression within the Pb+Pb measurements and will be used to assist interpolation of full energy p+p Y measurements to $\sqrt{s_{NN}} = 5.5$ TeV.

1.6 Connection with RHIC and RHIC-II programs

The scientific programs at RHIC and the LHC will be complementary and, together, will provide a comprehensive study of the properties of the quark-gluon plasma over an estimated initial temperature range $T_c < T < 5T_c$. Results from both programs will be required for the development of a systematic understanding of how the QGP is formed from initial semi-hard partonic scattering and emission, how it thermalizes, how it evolves dynamically, and how it hadronizes. Results from the LHC and RHIC will surely influence the thinking about results from the other program. In particular, measurements from the LHC that test concepts developed using RHIC results will certainly have an immediate and important impact on the RHIC program.

The interaction between the RHIC and SPS Heavy Ion programs provides a good model for the positive impact that the LHC Pb+Pb program will likely have on the RHIC program. In many places, but especially in the area of jet quenching, results from RHIC stimulated analysis of SPS data that would otherwise never have been performed – often with surprising and interesting results. A good example is provided by the strong distortion of the di-hadron correlation seen at RHIC [24]. This result from RHIC stimulated similar investigations by the CERES experiment which found similar features [25, 26] in their data. The fact that a similar modification of the di-jet shape is observed at SPS energies, where the p_T range of hard processes is extremely limited and where quarks dominate, necessarily constrains theoretical interpretations of the effects. The synergy between the SPS and RHIC programs has provided a substantial net benefit for the field as a whole. However, unlike the situation at the SPS where the heavy ion program was largely shut down when RHIC started operation, RHIC will be able to take full advantage of the insights gained from the LHC program and systematically explore the consequences of those insights – something that the LHC will not be able to do because of limited heavy ion running time. The institutions participating in the ATLAS Heavy Ion program have a history of strong involvement in and leadership of the RHIC heavy ion program and will use that involvement to facilitate the feedback of advances from the LHC program to the RHIC program and vice versa.

1.7 Proposal structure - UNDER CONSTRUCTION

The remainder of this document is structured as follows: Chapter ?? more fully explains the physics motivation and goals of complete jet measurements at the LHC and summarizes the ATLAS performance in carrying out full jet measurements in a heavy ion background. Chapter ?? describes the physics motivation for direct photon and photon-jet measurements and shows the results of studies of background rejection and direct photon efficiency in heavy ion collision along with reconstructed photon-jet correlations. Chapter ?? describes in more detail the physics impact of global measurements and shows results from studies of $dN_{ch}/d\eta$, $dE_T/d\eta$, event plane

reconstruction and v_2 measurement. Chapter ?? describes ATLAS quarkonia measurements and the physics impact of these measurements. Chapter ?? describes the nearly completed ATLAS zero degree calorimeter and the contribution of the calorimeter to the ATLAS Heavy Ion program. Chapter ?? describes the specific US computing needs for heavy ion physics and describes a plan to satisfy those needs. Chapter ?? provides a management plan and describes operational needs for the ATLAS Heavy Ion program. Chapter ?? summarizes the motivation for the ATLAS Heavy Ion program and US participation in the program and summarizes the results shown in Chapters ?? through ?? from physics performance studies to illustrate the unique contributions that ATLAS will make to the LHC Heavy Ion program.

Chapter 2

Simulations tools and Heavy ion detector occupancies

Chapter 3

Tracking in ATLAS

3.1 Tracking heavy ion events with the ATLAS detector at the LHC

The ATLAS Inner Detector (ID) has been designed to track charged particles in 5 units of pseudo-rapidity centered around mid-rapidity [27]. The detector combines three technologies, closest to the beam, tracking is done with silicon pixel detectors (Pixel) arrayed in a barrel with three layers (B-layer, Layer 1 and Layer 2) and 6 end-cap sections. The Pixel end-cap sections are mounted on disks perpendicular to the beam axis and placed on both sides of the nominal interaction point. The Pixel detector is followed by the Semiconductor Tracker (SCT) consisting of double-sided silicon strip detectors arranged in four layers in the barrel, and two sets of 9 end-cap disks located on both sides of the nominal interaction point. The third tracking detector is a Transition Radiation Tracker (TRT) based on drift tubes arranged in a barrel and 2 endcaps. The ID was designed with an high granularity to cope with the high luminosity expected in p+p collisions, which leads to multiple p+p collisions in each LHC bunch crossing. The granularity turns out to be essential for tracking charged particles produced in the high-multiplicity environment of heavy ion collisions in a wide pseudo-rapidity window.

3.2 Inclusive charged particle spectra

The ATLAS inner detector can be used to estimate the momentum spectrum of inclusive charged particles, which can contribute to measurements of charged particle multiplicity, transverse energy (via the mean p_T), and elliptic flow. This section describes the application of a standard ATLAS tracking algorithm to heavy ion events. A first reconstruction of particle spectra is performed.

The ATLAS tracking algorithm uses the Kalman filter method [28] (called “xKalman”) to do a simultaneous pattern recognition and track fitting in its three detector sections. Track candidates are formed from combinations of hits in the Pixel detector. These tracklets are then propagated outward taking into account the value of the magnetic field and the effect of multiple scattering due to the material traversed. Once the outer edge of the inner detector is reached, the process can be repeated backwards to improve the quality of the track fit. In order to define the tracking efficiency, a set of quality cuts is applied to all reconstructed tracks. This particular set of cuts may well evolve once actual data is available; however, at this moment they are the following:

- A track has to be formed with at least 10 hits (from a total of 11 and 12 active layers in the Pixel and SCT barrel and end-cap sections, respectively).
- Poor quality tracks are rejected by imposing a momentum-dependent cut that rejects the upper 5% of the χ^2/NDF distribution in each momentum bin.
- The normalized distance from the perigee of the track to the event vertex is defined as

$$R_{vtx} = \sqrt{((d_0 - d_{vtx})/\sigma_{d_0})^2 + ((z_0 - z_{vtx})/\sigma_{z_0})^2}$$

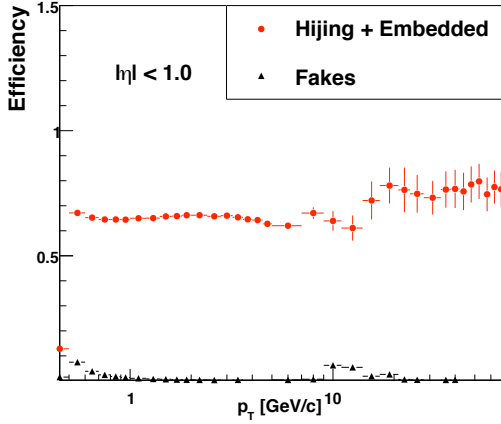
where d_0 is the distance of closest approach to the z axis in the $R\phi$ plane, z_0 the z coordinate of the track perigee, and σ_{d_0} and σ_{z_0} are the errors associated to these track parameters. All tracks have to satisfy a cut of $R_{vtx} < 3$.

- All tracks are extrapolated to the calorimeter, and have to match a tower with signal above a pre-determined threshold.
- The difference in θ and ϕ at the perigee of all track pairs is used to eliminate all but one copy from the sets of tracks that can be generated from signal deposited by a single generated particle; for each pair with $\Delta\theta < 0.005$ and $\Delta\phi < 0.01$ one track is rejected randomly.

The reconstructed tracks that satisfy the above conditions are then matched to the generated particles. The matching can be done by using two methods. The first one makes use of the difference between the pseudorapidity and the azimuthal angle at the perigee of reconstructed tracks and generated particles: a reconstructed track is compared to all generated particles and a match is declared for the pair that has the smallest value of $R = \sqrt{(\Delta\eta)^2 + (\Delta\phi)^2}$ which in turn is required to be smaller than a pre-defined value, i.e. $R < R_{cut}$. A second method matches reconstructed tracks to generated particles using the fraction of hits in the reconstructed track that are common to the generated particle. Each particle generates a set of hits and one hit can have contributions from several particles. The correspondence of a track to a generated particle is made when the track shares 50% of its hits with the particle. This method is used by the developers of the tracking algorithm and is typically used as the standard approach throughout ATLAS. Accordingly, this method provides the working definition of the tracking efficiency used here. Tracks that can not be matched to any of the generated particles, e.g. nearly straight tracks formed from random hit patterns, are then declared as fakes.

Within a window in pseudorapidity, the p_T -dependent tracking efficiency is defined as the ratio of the number of matched reconstructed tracks that satisfy all quality cuts divided by the number of generated charged primary particles in the same p_T bin. Primary particles are selected as those with the same z coordinate as the main event vertex. It is also required that the particles do not decay in the detector volume. Note that these studies have been done with a lower limit in the transverse momentum of the generated particles set at 400 MeV/c, since the tracking code has not yet been optimized for lower momenta in heavy ion collisions.

The filled circles in the left panel of Fig. 3.1 show the tracking efficiency in the pseudorapidity window $|\eta| < 1$ extracted from a sample of central Pb+Pb collisions simulated with HIJING without quenching (with $dN_{ch}/d\eta = 2700$). The tracking efficiency for particles with $p_T > 10$ GeV/c was extracted from a special sample of events where ten negative pions, selected from



Placeholder for future figure

Figure 3.1: (left) Efficiency and fake rate in $|\eta| < 1$ extracted from a sample of central ($b=2$. fm) HIJING events without quenching in the ATLAS tracking system (right, top) Tracking efficiency as function of pseudorapidity for tracks with $3 \leq p_T \leq 8$ GeV/ c extracted from the same events. (right, bottom) Fake rate as function of pseudorapidity for tracks with the same p_T as the top panel.

flat distributions in η and p_T , were merged with central HIJING events. The matching of reconstructed tracks with generated particles from this sample of embedded pions was done using the first matching method mentioned above, based on differences in η and ϕ . The filled triangles in the bottom panel of Fig. 3.1 show the rate of fake tracks found in the central sample. The impact of the matching of calorimeter tower information to tracks is most pronounced for tracks with p_T above 15 GeV/ c where the fake rate falls well below the value of 5%. The tracking efficiency has a weak dependence in pseudorapidity within the full coverage of the inner detector ($|\eta| < 2.5$). The top panel of the right side of Fig. 3.1 shows that the efficiency is 70% near midrapidity, and drops to about 55% at $\eta \sim 2$. The bottom panel of that figure shows the fake rate as function of pseudorapidity for tracks with $3 \leq p_T \leq 8$ GeV/ c . The growth of the fake rate with pseudorapidity is present at all values of p_T but it only reaches values that exceed 10% for $p_T \leq 1$ GeV/ c .

The spatial resolution of each tracking station is high (16 μm in the SCT), and the detector was designed to have low mass and minimize multiple scattering. The overall momentum resolution (defined as $\Delta p_T / p_T = |p_T^{rec} - p_T^{gen}| / p_T^{gen}$) has values as low as 2.5% around mid-rapidity for transverse momenta up to 10 GeV/ c . This resolution deteriorates slightly at high η where it reaches values of 4% for intermediate $p_T \sim 3$ GeV/ c . At high momentum, the design momentum resolution is 30% for 500 GeV/ c tracks.

The spectrum shown in Fig. 3.2 has been extracted with tracks reconstructed with the Pixel and SCT sub-detectors within a narrow pseudorapidity window ($|\eta| < 0.5$). The same quality cuts used in the definition of the tracking efficiency were imposed on the tracks used to generate this distribution. The yields were then corrected for tracking efficiency to calculate the final spectrum. There is no correction for fake tracks, but their contribution to the measured cross section has been estimated to be on the order of a few percent below 5 GeV/ c and can be kept below 10% at 10 GeV/ c and 1% at 30 GeV/ c .

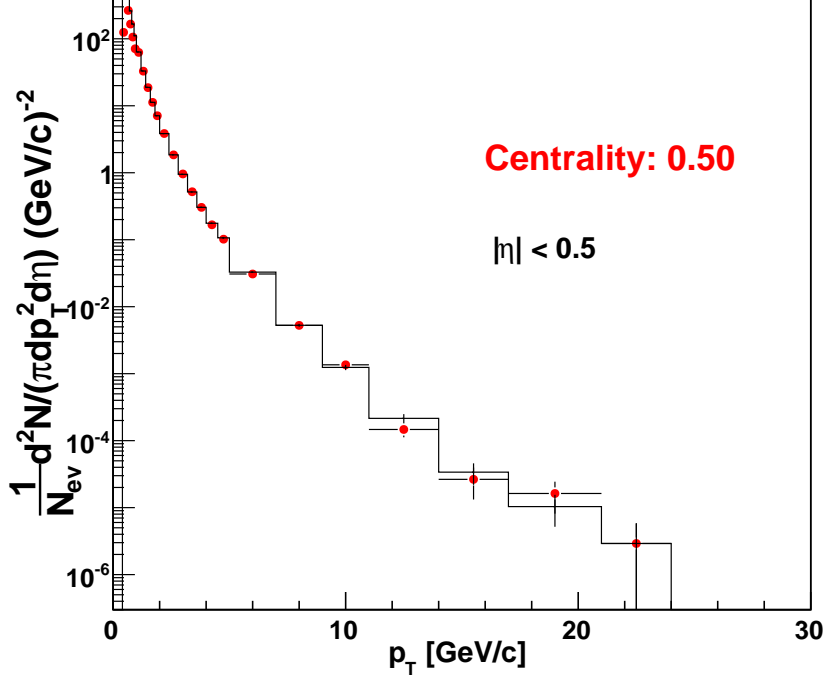
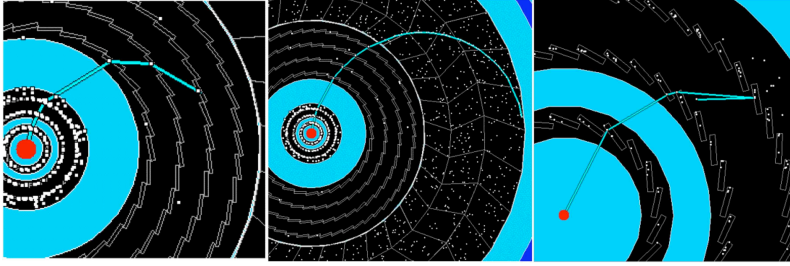


Figure 3.2: Invariant yield for a sample of central HIJING events without quenching ($dN_{ch}/d\eta = 2700$) in $|\eta| < 0.5$.

It should be noted that while most of the tracking studies performed for heavy ions so far are for particles with $p_T > 400$ MeV/c, this is not due to limitations of the ATLAS detector itself. The tracker is sufficiently large compared to the bending power of the main 2 T dipole field such that particles below $p_T < 400$ MeV/c leave full tracks in the silicon, as shown in Fig. 3.3. The main limitation in reconstructing the low p_T tracks, at present, is the implementation of the tracking code, which is currently too memory-intensive to handle the high occupancies of heavy ion events. However, this is a situation that is rapidly improving, especially with all of the work taking place for the p+p data-taking preparations. The right panel of Fig. 3.3 shows the track finding efficiency for two other ATLAS tracking algorithms (newTracking and iPatRec) run on p+p events[29]. It is observed that reasonable efficiency is found even for tracks down to 100 MeV/c. Development to extend this work to heavy ion collisions is ongoing.

3.3 Vertex reconstruction

This section will contain a brief description of the vertexing tool. This description will put an emphasis on the complexity of the task and the several choices on methods to find the vertex. We will produce figures that will mainly show 3D vertex resolution in heavy ion events. We will compare SingleAdaptive and MultipleAdaptive modes. We will investigate the efficiency of the



Placeholder for future figure

Figure 3.3: (left) Tracks of $p_T = 50, 150$ and 400 MeV/c in the ATLAS spectrometer. (right) Efficiency for particles reconstructed by two standard tracking algorithms in p+p collisions vs p_T , showing reasonable efficiency down to 100 MeV/c.

algorithm for different event centralities.

Chapter 4

Forward Instrumentation

4.1 The ATLAS Zero Degree Calorimeter

The Zero Degree Calorimeters (ZDCs) have played a crucial role in the heavy ion physics program at RHIC, and we expect the same to be true for the LHC program. The ATLAS Zero Degree Calorimeters are the sole hardware contribution to the ATLAS detector by the US ATLAS Heavy Ion program. At this time, November 2008, the two ATLAS ZDCs, one in each beam direction, have been mechanically assembled and installed in the LHC tunnel. This chapter summarizes the physics role of the ZDCs and provides a brief description of their design and implementation. Further details on the ATLAS ZDC, its design and physics simulation may be found in the original Expression of Interest [30].

4.2 Physics Motivation

The primary motivation for building the ZDCs for the ATLAS Heavy Ion program is to serve both as a high-efficiency, low-background trigger for Pb+Pb events, and as a means to characterize the centrality. The collision centrality reflects the event-by-event change in the impact parameter between the colliding nuclei. As illustrated in the left panel of Fig. 4.1, at a given impact parameter, the participating nucleons reside in the overlap region, while the rest of the nucleons continue forward as “spectators.” Central events, with the smallest impact parameters, have the largest number of participants, but yield the fewest spectator neutrons in the far forward region. Peripheral events with large impact parameter yield a far larger number of spectators. This phenomenon is illustrated in the right panel of Fig. 4.1, which shows the strong anti correlation between the ZDC neutron multiplicity and energy observed in the forward hadron calorimeter, from a fast simulation.

The spectator neutrons are also sensitive to the direction of the reaction plane, defined as the plane transverse to the beam direction with the X axis oriented along the impact parameter. This is an important method used alongside the other methods discussed in Chapter ??, but which is in principle independent of other observables[31], and thus minimizes contamination by non-flow. Coordinate readout has been implemented in the PHENIX and STAR ZDCs at RHIC by means of a shower-max detector mounted after 2 int. lengths. Data from these detectors at RHIC (see e.g. Ref. [32]) has shown that event-by-event energy flow of forward neutrons exhibits “directed

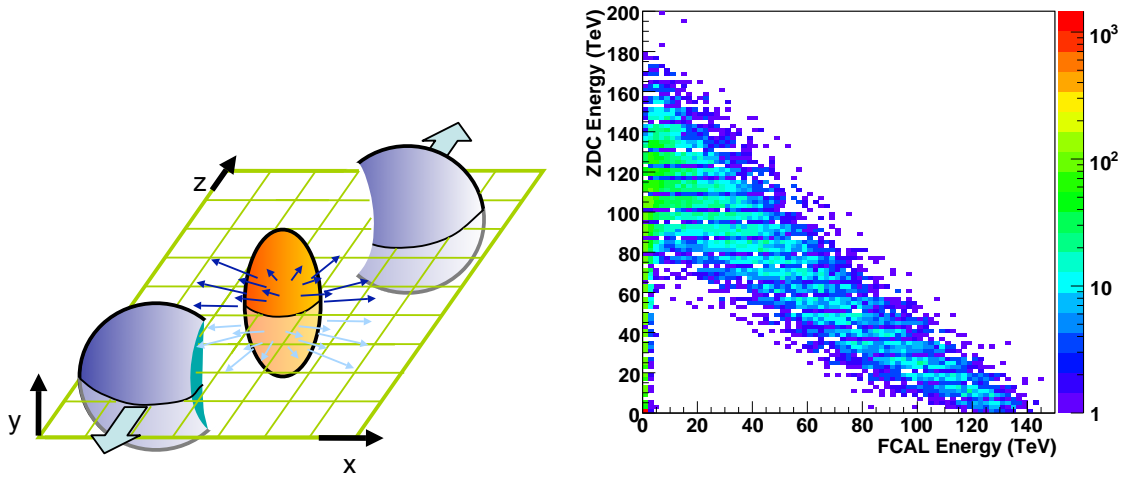


Figure 4.1: (left) Schematic of a nuclear collision, showing the participants in the overlap region and the spectator matter on the sides. The reaction plane is defined as the vector joining the nuclei centers. (right) Correlation of simulated ZDC response with the forward energy emitted into the ATLAS Forward Calorimeters.

flow”, or a $\cos(\phi)$ dependence relative to the reaction plane measured by produced particles.

It is expected to have similar or better performance at ATLAS since the ZDC has been designed from the ground-up to provide position sensitivity.

Ultra-peripheral Collisions (UPC), large impact parameter ($b = 25 - 30$ fm) events where the very strong EM fields of the Lorentz-contracted nuclei dissociate the nucleus in the opposite beam, provide an intriguing way to probe the low- x structure of nuclei with real photons, complementary to traditional DIS techniques. The detection of large numbers of forward neutrons in one direction with the ZDC, in tandem with no or possibly one (from additional photon exchange) neutron from the nucleus that emits the high energy photon, is the only known way to trigger on this kind of events. In this way, the ZDC in ATLAS opens up entirely new tools for studying the partonic structure of nuclei.

4.3 ZDC design

In order to only be sensitive to spectator neutrons, the ZDCs are located in the TAN absorbers, 140m in both directions from the nominal interaction point, as shown in Fig. 4.2. The size of the TAN dictates the dimensions of the calorimeter, and thus the detector acceptance, which effectively covers $\eta > 8$.

The ZDC module and detector design is shown in Fig.4.3. The modules consist primarily of a sandwich of tungsten radiator and quartz rods that are used to collect Cherenkov light generated

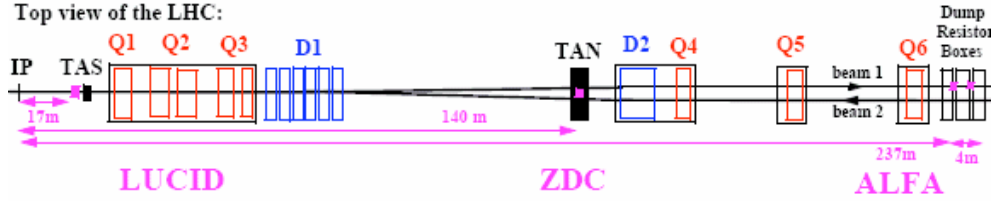


Figure 4.2: Schematic of the ATLAS beam line, showing the position of the ZDC in the far forward region.

by the electromagnetic and hadronic showers. Each ZDC detector consists of four modules, all of which are similar and have the same intrinsic energy resolution but several have particular capabilities. The three module types are

- **EM X-Y Module** This is the first module which has been provided with X-Y coordinate readout by means of quartz rods which also penetrate the tungsten plates longitudinally allowing the position location of EM showers in an 8x8 grid.
- **Hadronic X-Y Module** This is similar to the EM X-Y Module, but has 24 channels, since the showers will be much wider in this module.
- **Hadronic Standard Module** This module is comprised of quartz rods sandwiched between the tungsten plates. There is no position sensitivity in these modules, which are the rear two modules in each arm, and thus give a single energy measurement per module.

While the energy measurement is essential for event triggering and centrality selection, the position sensitivity of the front two modules provide two additional functions that are well motivated by physics issues in Pb+Pb p+Pb and p+p :

- **Directed Flow:** In heavy ion collisions the transverse coordinate measures the net p_T of the particles hitting the front face of the ZDC. This net p_T is directly related to the directed flow and the reaction plane angle.
- **Neutral Meson Reconstruction:** In p+p and p+Pb interactions, where the detector occupancy is low, the first ZDC module has impressive capability for reconstructing neutral particles which decay electromagnetically near the interaction point (IP)

4.4 Triggering in Pb+Pb

The two main triggers expected for heavy ion running are:

- **Minimum-bias Trigger:** the ZDC minimum-bias trigger is straightforward, requiring a coincidence of energy $E > 0.1 \times E_{beam} / A$ in both arms. The purpose of the trigger is to indicate an inelastic nuclear collision, either via strong or electromagnetic interactions. Similar triggers have been successfully implemented at RHIC, with high efficiency and low fake rate.

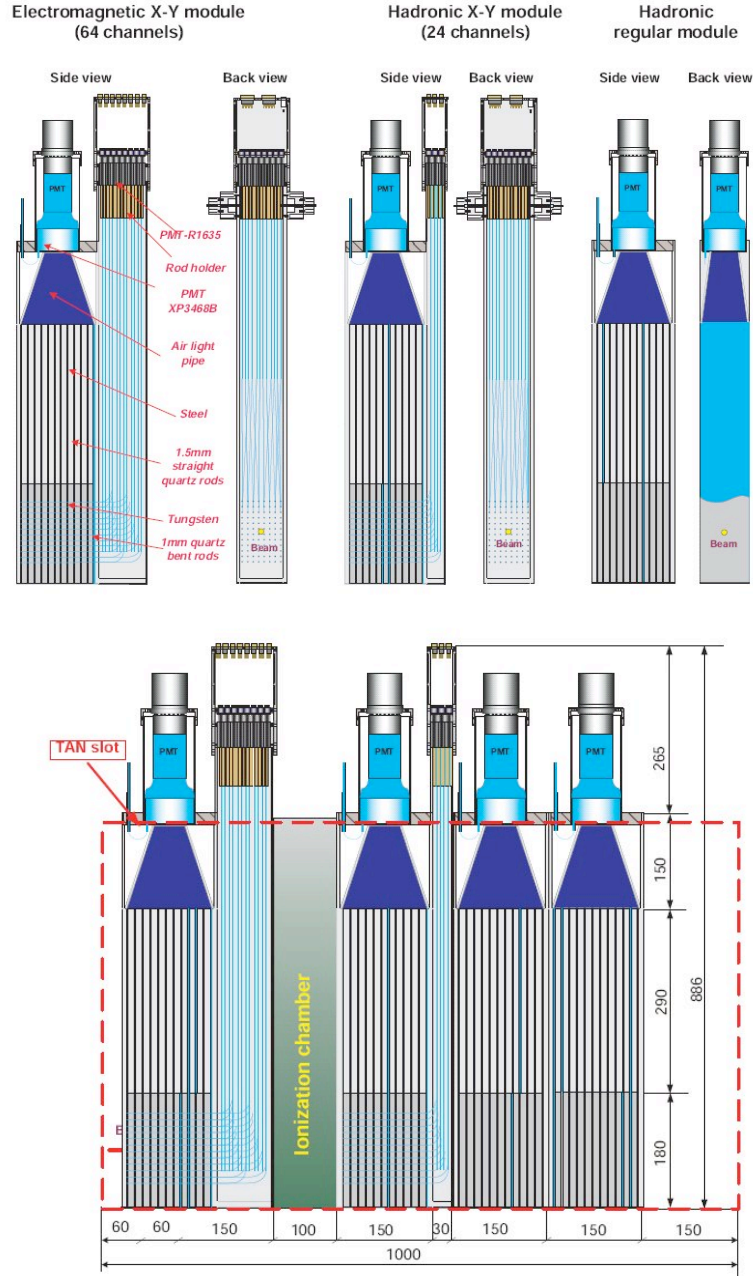


Figure 4.3: (top) ZDC module types and their designs (bottom) ZDC configuration planned for standard running the TAN absorber, from Ref. [30].

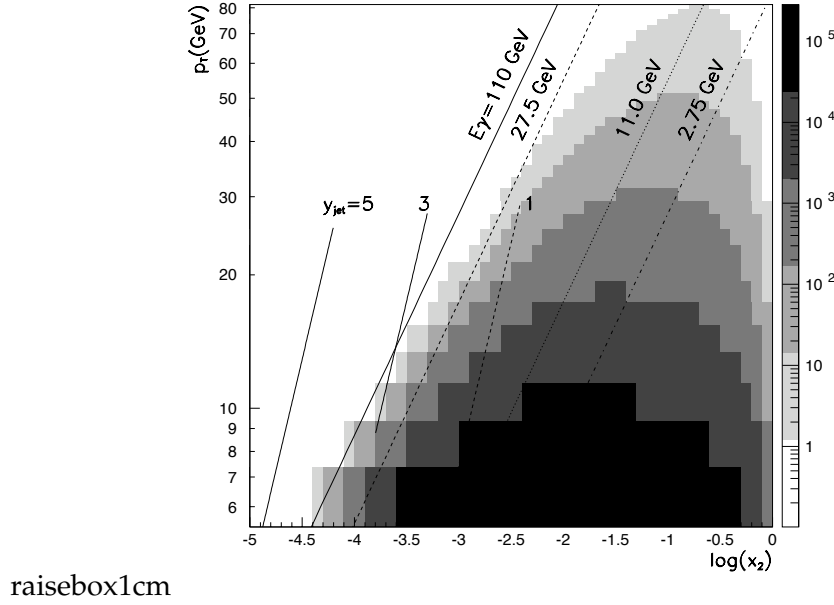


Figure 4.4: Rates of dijet production in ultra-peripheral collisions at the LHC, from Ref. [33].

- **UPC quarkonia production:** This trigger is based on detecting a J/Ψ or Y produced in coincidence with a ZDC signal above threshold. In PHENIX, one electron candidate in the central detector was required (corresponding to one J/Ψ decay) in coincidence with one or more ZDC clusters. A similar strategy should be appropriate for ATLAS where the calculated fraction of events with one or more neutrons (due to an additional photon exchange) is roughly 50%.

Of course, trigger development and commissioning is highly contingent on experimental and physics working conditions, and it might be found that the final running conditions are somewhat different than RHIC. Thus, it is crucial to have the flexible ATLAS multi-level trigger system which can allow the integration of ZDC triggers with other ATLAS triggers.

4.5 Low- x physics in Pb+Pb and p+Pb with UPC

As discussed in Section 4.2 the collision of Pb ions at LHC energies will provide a large sample of ultra-peripheral (UPC) interactions, which are similar to DIS events, but with real photons. These present an opportunity to make measurements of nuclear (in Pb+Pb) and even nucleon (in p+Pb) PDFs at very small x (down to $x = 10^{-6}$), as well as to study diffractive dissociation off nuclei by photons. The signature of diffraction dissociation is that one nucleus exchanges a color neutral object (ie 2 gluons) and therefore it is separated by a rapidity gap from the rest of the event. Diffractive events are expected in 50% of the dijet photoproduction sample and 10% in the PbPb case. It would be interesting to test this prediction. This has been discussed in detail in Ref. [33]. Aside from providing important insights into the initial conditions of heavy ion colli-

Figure 4.5: Reconstructed neutral meson decays in the ZDC acceptance for p+p collisions at full LHC energy.

sions by testing models of the nuclear wave function, e.g. based on the Color Glass Condensate, these measurements are of interest in their own right. Similarly, in p+Pb collisions, the density distribution of partons inside the proton can be measured in a kinematic regime similar to HERA. Ref.[33] includes specific calculations including realistic p+Pb luminosities. An example of this is shown in Fig. 4.4 where rate of jet production in UPC collisions as a function of x and photon p_T for a nominal one month Pb+Pb run. For these measurements the ZDC (1 arm) together with jets in the central detector provide a trigger. It is important to provide something like the rapidity gap requirement used by PHENIX in the trigger. We are exploring the possibility of doing this with the FCAL. Another aspect of the trigger we are studying is how low p_T a jet trigger could be used in relatively quiet events selected by the rapidity gap trigger. In this event sample we will have 2 classes- ie events with one isolated nucleus(non-diffractive) or two isolated nuclei (diffractive). By isolated we mean possibly emitting at most one neutron with a rapidity gap in the FCAL. In non-diffractive events ZDC multiplicity can be used to determine which nucleus emitted the photon since the other nucleus will emit many neutrons. In diffractive events both nuclei will emit one or no neutrons so you can't tell.

4.6 Physics Topics in pp Data

Although the ZDC has been designed for measurements with heavy ions there are many topics in pp physics that could be addressed with early data even at low luminosity. We discuss those of interest to the cosmic ray community in the next section. It is a good thing to explore such a program

4.7 Connections to cosmic ray physics

While the ZDC will of be great use in the p+p program as a luminosity monitor, there are also useful measurements that can be made in minimum bias p+p collisions that are of great interest to the cosmic ray community.

- The forward distribution of neutrons in p+p interactions reflects the event-by-event inelasticity. This is of great importance for Cosmic Ray physicists trying to calibrate HiRes, Agasa and Pierre Auger data for showers above 10^{16} eV using hadronic models. While some data exists on the x_F distribution of neutrons between $0.2 < x_F < 1.0$ at the ISR, and preliminary results are in preparation from PHENIX, this would be a very important measurement at the LHC.
- The x_T and p_T distribution of π^0 and η mesons in the far forward direction also of great interest for model builders of high energy cascades primarily interested in interpreting cosmic ray data. The ATLAS ZDC has a large acceptance in these parameters as shown in Ref. [30]

and therefore should provide useful empirical information needed to constrain model parameters. As an example, Fig. 4.5 shows the mass distribution of di-gammas from a sample of 1M PYTHIA events and using a simulation of the full ZDC response.

Considering that the p+p program will get underway in Summer 2008, and possibly several years ahead of the heavy ion program, these topics will be the first major application of the ZDC in ATLAS, and thus essential preparation for the heavy ion program.

4.8 Physics with forward neutrons in ATLAS

4.9 UPC in Pb-Pb

A General feature of UPC is that in Heavy Ions the electromagnetic cross sections are larger than in pp because they are roughly proportional to Z^2 . Also there is no competition from the larger diffractive rate.

They are characterized by the presence of at least one rapidity gap along one beam direction (the one that emits the photon). In diffractive processes, such as quasi-elastic J/ψ or Y production: $\gamma + A \rightarrow J/\psi + A, J/\psi + A^*$, or diffractive di-jet photoproduction, there are gaps along both beam directions. For trigger purposes it is useful to consider only those events where a second soft photon was exchanged exciting one of the nuclei -which then emits a neutron. This reduces the cross section by a calculable amount-typically 50%.

Quasielastic J/ψ or Upsilon photoproduction: In this process, one ion emits a spectrum of photons - usually calculated using the Weizsacker-Williams method- followed by the usual picture for photoproduction off a hadron. For example, the photon materializes into a heavy quark $q\bar{q}$ pair which exchange of a two gluon ladder with the target ion. Then they materialize as a vector meson.

Three processes are of interest - the coherent onium production, production of onium at moderate t with break up of the nucleus, and large p_t production of onium with a rapidity gap between the onium and the produced hadronic system.

(i) *Coherent production.* The four momentum(t) transfer distribution is steep, as expected for coherent production off a large target. In the leading twist approximation the coherent cross section is expressed through generalized gluon pdf in the nucleus - providing sensitivity to the gluon shadowing effects. As a result the coherent cross section integrated over t is $\propto A^{4/3}$ with a reduction of the A dependence due to the gluon shadowing which may reduce power to $A^{1.1}$. In the limit of strong gluon field the regime of the complete absorption is expected to set in (Black Disk regime) with a dramatic change of A -dependence of the cross section to $A^{2/3}$. The technical problem with this process is that for coherent processes it hardly possible to determine which of the nuclei emitted the photon, which effectively limits the range of probed energies to $W^2 \gamma N = 2m_V \cdot E_N$. Two other processes allow one to avoid this problem.

Incoherent onium production

In this process a two gluon ladder is attached to one nucleon of the nucleus which receives a substantial transverse momentum and is knocked out of the nucleus. This process is accompanied with emission of several neutrons (~ 4) [?]. Hence detection of these neutrons allows one to determine which of the nuclei emitted the photon and hence perform studies of onium production at larger W than in the process (i). This process is also very sensitive to the onset of the black disk

regime as in this case transition from the regime of color transparency $\sigma \propto A$ to the regime of strong absorption $\sigma \propto A^{1/3}$ corresponds to as strong change of the A-dependence as in the case of process (i).

Large p_t onium production This process is expected to be dominated by an exchange of the two gluon ladder with one parton of the target leading production of hadrons in the nucleus fragmentation region followed by rapidity gap. Neutron production in the nucleus decay allows one to trigger on such diffractive events, and determine which of the nuclei fragmented hence resolving ambiguity mentioned above. Since J/ψ produced in this kinematics have rather large transverse and longitudinal momenta acceptance to such J/ψ 's should be reasonable. These processes provide a fastest way to tracking fast small color dipoles through strong gluon fields at the LHC and would allow one to determine the onset of the black disk regime for dipoles of the transverse size of the order 0.25 fm [?].

Experimental Issues Because of the limited acceptance in p_t , the measurement with Upsilon's is the most likely to be useful. One would trigger on two high- p_t muons, at least one neutron in either ZDC and rapidity gaps-possibly using the FCAL. Even so, more about the detailed rapidity and p_t acceptance needs to be studied. The trigger rate is probably small- possibly comparable to 0.5% σ_{inel} as in PHENIX.

4.10 p-Pb

In this case the dominant process is photoproduction off the proton since the photon coupling is so much stronger. Quasi-elastic production off the proton is also of general interest. There was a lot of work on it at HERA. ATLAS would extend the data to the highest energies and resolve many open issues like the W dependence of the cross section. Also it may help to separate quasielastic $\gamma + p \rightarrow J/\psi + p$ and inelastic diffractive processes $\gamma + p \rightarrow J/\psi + M_X$ as a significant fraction of inelastic diffractive final states ($\sim 40\%$) will contain leading neutrons. It will allow one to produce more reliable measurements of the t dependence of the quasielastic process (which for large t becomes a correction to the inelastic diffraction) and also to measure the ratio of inelastic and elastic diffraction at small t which measures fluctuations of the gluon density in protons at small x [?]. For the large t onium production it will allow one to measure the energy dependence of the BFKL pomeron at large t [?]

Other processes in the pPb scattering where neutrons would be useful are diffractive processes with production of dijets - for example direct photon production of two jets. It would be possible to study the fraction function [?, ?] for the process $\gamma p \rightarrow 2jets + X + n$ (which satisfies the Collins factorization theorem [?]) for the case when a gluon is removed from the proton. In the inclusive dijet production the neutron multiplicity could serve as a tool for selecting more peripheral and more central collisions.

The hard p Pb collisions (production of dijets, etc) will allow measurement of nuclear pdfs down to small x . In parallel with UPC measurements of the same quantities it will allow one to test QCD factorization in the dijet production. The measurement of the neutron multiplicity will help to separate peripheral and central p-Pb collisions.

4.11 pp

Inclusive Neutron cross section:

There is renewed interest in this topic since both H1 and ZEUS measured this cross section with their forward neutron calorimeters. They measure $\frac{d\sigma}{dx/dp_t^2}$ and find a disagreement of a factor of 2 with the ISR when both results are divided by the corresponding inelastic cross sections. Also they observed that for most kinematics the spectrum of neutrons produced when a gluon was removed from the target was practically the same as for the quark removal which indicates dominance of the fragmentation processes over the triple region processes. At the same time for the neutrons with x_F very close to one the pion exchange may give the dominant contribution as suggested by several authors, see e.g. Kaidalov, and Kopeliovich, Soffer et al. The complication of the hadronic processes as compared to the DIS that colliding protons can be involved in multiple soft and hard collisions which will screen production of the leading baryons. This effect is likely to be enhanced at the LHC where interaction at central impact parameters is strongly absorptive. Hence it would be very interesting to study to what degree Feynman scaling is violated for the neutron production when energies are increased from ISR/RHIC energies to LHC energies.

The centrality argument suggests that leading neutrons can be used as a tool for selecting peripheral events. Alternatively one can argue that a veto for production of leading baryons can be used to enhance the contribution of very central pp collisions which are characterized by very high small x gluon densities [?].

Overall, detection of neutrons provides a unique tool for the study of super long range correlations in rapidity - on the scale 20 units!! A sample of simple questions:

- If the leading neutrons are produced in peripheral collisions there should be a positive correlation between production of leading neutrons in two fragmentation regions which should be strongest at large $|x_F| \geq 0.7$.
- The dijet production at central rapidities is dominated by collisions at small impact parameters. Hence one can expect the decrease of leading neutron multiplicities in both fragmentation regions.
- Larger than average central multiplicities are likely to originate from more central collisions. How would the forward neutron spectrum/ differential multiplicities would change with an increase of the central multiplicity?

One would also be able to use neutrons in the studies of the photoproduction of Υ in pp collisions. Similar to the AA case one would be able to use them to select diffractive dissociation and resolve the forward backward photon ambiguity. Also it would allow one to measure processes of inelastic diffraction with production of Υ .

Experimental issue: The trigger would simply be either ZDC with say 0.1*pbcm in energy and a central interaction trigger like MBTS.

Of course the rate will be high so it is part of the minbias suite. Measuring the p_t distribution- which we have to integrate over to get the cross section- is an issue. The acceptance should be checked with HERA and ISR data or PYTHIA.

$\pi - \pi$ elastic scattering: As mentioned above, inclusive neutron production at very large x_F and small p_t proceeds by pion exchange at large impact parameters. For this reason, if we observe 2 leading neutrons and pions in the central detector we are really measuring the $\pi - \pi$

elastic cross section at very high energy and potentially out to high t . This is a unique and very interesting measurement. Experimental details: Its not yet clear whether this is possible. The trigger would have to be a ZDC coincidence with rapidity gaps since it would be hard to trigger on the pions. So this trigger rate should be compared with the calculated cross section. This is under study.

Topics in Hard Diffraction:

In diffractive collisions one of the beam protons often leaves the collision intact. A fraction of the time it is excited to a system with additional pions The $N^*(1400)$ is the lowest lying state and there is a continuum falling off as $1/M^2$. The spectrum is reasonably well known at the Tevatron, though extrapolations to the LHC are strongly model dependent. Very little is known about double diffraction when both nucleons are excited to higher mass states leaving large rapidity gap in between. Measurement of the neutrons in both ZDCs provides a nearly model independent method of studying these cross sections. First one measures multiplicity of neutrons in single diffraction, and next uses a factorization approximation - independence of neutron multiplicity in two diffractive clusters (assumption valid in all current models) to determine the ratio of double and single diffraction. An interesting information on the mechanism of diffraction maybe provided also by a study of the correlation of the transverse momenta of the neutrons. Indeed it is usually expected that the t -dependence of double diffraction is very broad $\sim \exp(B_{dd}t)$, $B_{dd} \sim 2\text{GeV}^{-2}$. If so the relative transverse momentum of the two clusters is, on average, of the order of $\sim 1\text{GeV}$, which maybe reflected in nonzero value of $\langle \vec{p}_{n1t} \cdot \vec{p}_{n2t} \rangle$. One can consider this quantity both for the case of fixed \vec{p}_{n1t} and vary it. Also one can study if for different masses of the produced hadronic systems provided one gets information on rapidity interval filled by hadrons from other components of the detector

There are still some open questions about data from the Tevatron where one would have liked to measure the leading proton as well as the antiproton. A lot is at stake for the LHC. With the neutron there is the possibility of accessing directly the question of what fraction of the exclusive dijet cross section is really exclusive. This makes a huge difference for the search for exclusive Higgs at the LHC.

4.12 Operations issues

The ZDC is an extremely radiation-hard calorimeter. It has been tested up to $\sim 5\text{GRad}$ absorbed dose and will have an essentially infinite lifetime during the Pb+Pb operation of the LHC. Unfortunately the detector is not expected to survive more than a few months of operation at LHC p+p design luminosity. The light attenuation in the optical systems will become significant in the visible wavelengths and as a result the resolution of the device will deteriorate. This is a possible way to operate the ZDC but it will substantially limit the usefulness for a long term heavy ion program. Therefore, once the p+p luminosity of the LHC reaches $10^{33}\text{cm}^{-2}\text{s}^{-1}$ the ATLAS ZDC will be removed for high luminosity runs and replaced for heavy ions or for special low luminosity p+p runs. In order to minimize occupational dose to those replacing the ZDCs during these transitions, a remote handling scheme is being designed to eliminate radiation exposure. During high-luminosity stores the ZDCs will be relocated to a shielding enclosure and will be replaced by copper absorber bars in the TAN.

During the first period of 43 bunch operation, the ATLAS ZDC will have its first module re-

placed by a module from the LHCf detector (~ 30 cm long). This allows the LHCf experiment to carry out its program during the first few weeks of operation of the machine. When their program is completed, the corresponding ATLAS ZDC module will then be re-inserted and the full program of measurements will continue.

4.13 Summary

The Zero Degree Calorimeters (ZDCs) will play a crucial role in the heavy ion physics program at the LHC.

- The ATLAS Zero Degree Calorimeters (ZDCs) are the main hardware contribution to the ATLAS detector from Brookhaven National Laboratory and the US ATLAS Heavy Ion program.
- The ZDC will provide an event trigger, centrality characterization, reaction plane determination, and UPC capabilities in Pb+Pb collisions
- It also provides unique capabilities for forward neutron and hadron production in p+p collisions, of great interest to cosmic ray physics
- The two ATLAS ZDCs, one in each beam direction, have been mechanically assembled and installed in the LHC tunnel.
- Operations issues are known and being addressed in collaboration with ATLAS management.

Bibliography

- [1] V. M. Budnev, I. F. Ginzburg, G. V. Meledin and V. G. SerboPhys. Rept. 151974181
- [2] G. A. Schuler and T. SjöstrandNucl. Phys. **B**4071993539
- [3] A. Donnachie and P. V. LandshoffPhys. Lett. **B**2961992227

Chapter 5

Global Variables

This chapter will discuss the ATLAS capabilities for measuring several “global” observables, by which are meant: charged-particle multiplicities, transverse energy, and elliptic flow. Of course, a precise estimation of event centrality is an essential part of measuring any of these variables, and so will also be discussed. Global variables have the paradoxical role of being integrals of particle number and energy in the final state, but which appear to reflect dynamical quantities (e.g. entropy, transverse energy) established much earlier in the system evolution. Most importantly, they provide access to aspects of the system relevant to understanding the nature of the strongly coupled fluid. The particle multiplicities should be directly relevant to the initial state entropy. The elliptic flow reflects a combination of the equation of state (EOS) as well as the shear and bulk viscosities.

Global variables will certainly be the focus of Day-1 physics activities at the LHC, when heavy ion collisions are delivered to the experiments sometime in 2009 or 2010. Even with low to moderate luminosity, 50 Hz taken to tape will amount to 2 million Pb+Pb events per day, providing sufficient data within a few days to test extrapolations of RHIC data to LHC energies. As part of this process, the measurements of similar variables in proton-proton collisions (which will most likely be the first data published from the ATLAS detector) will be essential preparation for heavy ion data taking, trigger preparation, and analysis – and work on this is already underway.

5.1 Global physics at the LHC

While it is difficult to calculate features of soft particle production from first principles in the complicated environment of a heavy ion collision at high energies, it is found that global observables follow relatively simple patterns which may eventually give some insight into the bulk (and generally non-perturbative) sector of QCD. At the same time, measurements of inclusive charged particle density will be essential for an empirical understanding of particle production in these collisions, and will help constrain the gluon densities that will be needed for jet quenching calculations.

Various predictions for inclusive particle production at the LHC have been made, that test the applicability of different theoretical approaches already applied at RHIC. Three of these predictions for $\rho(s) = (dN_{ch}/d\eta)/(N_{part}/2)$ are shown in Fig. 5.1, overlaid on data from p+p and A+A collisions. The first is the simple $\log(s)$ trend that is often invoked as a description of data from

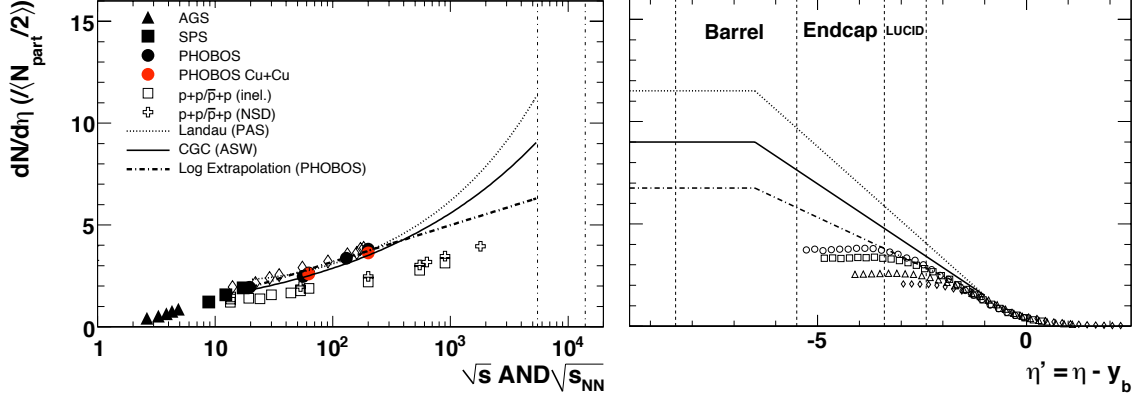


Figure 5.1: (left) Data for $dN_{ch}/d\eta(|\eta| < 1)$ vs \sqrt{s} for A+A and p+p collisions, compared with three theoretical extrapolations [34, 35, 36]. (right) Capabilities of ATLAS detector, in the rest frame of one of the projectiles, compared with RHIC data. The lines show how extended longitudinal scaling behavior might appear, given the mid-rapidity predictions of the three models in the left panel.

AGS to RHIC energies, and thus may well be relevant at the LHC [37]. This extrapolates to a value of around 6.5 at $\sqrt{s_{NN}} = 5520$ GeV, which is the lowest value considered. The second is a functional form suggested by Color Glass Condensate-based models, $\rho(s) = N_0 s^\lambda$, with λ being extracted from scaling violations measured at HERA [34]. With parameters taken from Ref. [34], which misses the RHIC data by about 10%, one gets $\rho(s) \sim 9$, corresponding to $dN_{ch}/d\eta \sim 1600$. Finally, Carruthers' version of Landau's hydrodynamical model gives a functional form proportional to $s^{1/4}/\sqrt{\log(s)}$ with no free parameters[35]. Tuned to the RHIC data, as was done in Ref. [36], this function extrapolates to $\rho(s) \sim 11.5$. Clearly, within a few days of first LHC running, entire classes of models may be excluded, and new data will be added to this compilation. This example illustrates that essentially every measurement of global variables will contribute to our understanding of heavy ion collisions, a situation which is unique to the heavy ion program, even with p+p, and especially if the machine ramps up slowly, exploring different energies for short periods of time.

At RHIC there was a general expectation that particle production and transverse energy would arise from a combination of soft processes and semi-hard process, each with a distinct scaling with the nuclear geometry. Soft processes are thought to deal with long wavelength excitation processes and thus scale with the number of excited (or "wounded") participant nucleons. Semi-hard processes, or mini-jets, while at a lower energy scale than usually considered for isolated jets, are thought to scale with the number of binary collisions (which exceed the number of participant pairs $N_{part}/2$ by a factor of ~ 10). These assumptions are the basis for the "two-component" model for inclusive particle production:

$$\frac{dN}{d\eta} = n_{pp} \left[(1-x) \frac{N_{part}}{2} + x N_{coll} \right] \quad (5.1)$$

At the same time, RHIC data on ratios of $\rho(s)$ at different N_{part} and different \sqrt{s} , have shown

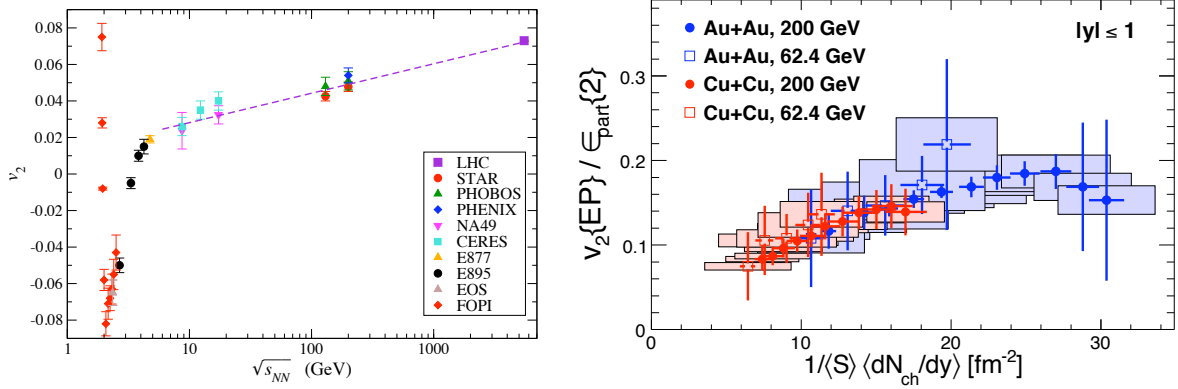


Figure 5.2: (left) Compilation of data on v_2 vs. \sqrt{s} in heavy ion collisions, from Ref. [34]. (right) Data for v_2/ϵ vs. the areal density of charged particles, for two energies and two colliding systems, from Ref. [40].

that $\rho(s)$ “factorizes” as $f(s)g(N_{part})$ [38]. This is apparently at odds with the two-component model, even at RHIC, but the interpretation remains controversial. Thus, the LHC will provide the definitive test of the role of semi-hard processes in the entropy of the sQGP. The addition of E_T measurements as a function of centrality will provide additional insights into whether there is an increase in transverse activity due to the presence of minijets scaling with N_{coll} .

While the previous discussion involved the inclusive charged particle multiplicity near mid-rapidity, the large acceptance will also play a crucial role in the elucidation of global properties. One key observation away from mid-rapidity at RHIC was that of “extended longitudinal scaling” [39]. This phenomenon, shown in the right panel of Fig. 5.1, characterized by the fact that the normalized inclusive yields are invariant with energy when viewed in the rest frame of one of the projectile, by plotting yields as a function of $\eta' = \eta - y_b$, where y_b is the beam rapidity. It is also observed that while the phenomenon is observed at all centralities, the invariant yield vs. η' varies with centrality. The same figure also shows how the various ATLAS sub-detectors are situated in η' space, illustrating the dramatic extension to large negative η' as well as the overlap in the forward region. While the silicon and tracking detectors only extend to $\eta = 2.5$, the calorimeters provide measurements out to $\eta = 5$, and the LUCID detector (Cerenkov tubes) should provide multiplicity measurements of primaries out to $\eta = 6$, overlapping the RHIC data.

Elliptic flow, which is manifest as a significant anisotropy in the event-by-event azimuthal distribution of inclusive particles, is one of the more striking phenomena observed at RHIC. The azimuthal modulation is typically characterized by the second Fourier coefficient v_2

$$\frac{dN}{d\phi} \propto 1 + 2v_2 \cos(2[\phi - \Psi_{RP}]) \quad (5.2)$$

where Ψ_{RP} is the angle of the “reaction plane” (defined by the vector connecting the centers of the colliding nuclei). This quantity has been measured over a wide range of energies, collision systems, and centralities by all of the RHIC heavy ion experiments and several AGS and SPS experiments. A compilation of v_2 vs. \sqrt{s} for minimum-bias heavy ion collisions, is shown in the left panel Fig. 5.2, from Ref. [34]. While there is a non-monotonic behavior observed below

$\sqrt{s} = 4 - 5$ GeV, above this energy (including the AGS, SPS, and RHIC data) a logarithmic rise is observed. The further energy dependence is difficult to predict from first principles, as it depends on the details of the initial state and on the EOS. It has been suggested by some authors that the logarithmic rise could continue to higher energies (reaching $v_2 \sim 0.7$ at LHC energies for minimum-bias samples), while others have suggested that the “hydro limit” may already have been reached at RHIC, implying no further rise in v_2 . This hypothesis has been tested by correlating v_2/ϵ (where ϵ is a measure of the spatial eccentricity of the initial state) with $dN_{ch}/dy/S$ (where S is the area of the nuclear overlap region), shown in Fig. 5.2 from Ref. [40]. This plot seems to show a constant rise of elliptic flow as the areal density of charged particles increases, but some still see a flattening at large value of $dN_{ch}/dy/S$. Finally, some authors predict that elliptic flow at the LHC may even decrease [41]. As with the multiplicity predictions, only the LHC will provide enough of a lever arm to really test these hypotheses.

5.2 ATLAS capabilities

The ATLAS detector has unprecedented acceptance and hermeticity for the measurements of global variables. Whereas at RHIC, experiments have had to make serious choices optimizing acceptance vs. capability (e.g. choosing large aperture tracking and limited calorimetry, or vice versa), the ATLAS detector has a full 10 units of rapidity coverage for calorimeter, both electromagnetic (EM) and hadronic, and 5 units of rapidity for tracking. There is also substantial forward coverage beyond the central detector, with the LUCID counter being staged in from $5.3 < |\eta| < 6$ and especially the ZDC being built by the ATLAS Heavy Ion group, which detects neutral particles with $|\eta| > 8$ [39]. The ZDC also has a position-sensitive front face that can be used to estimate directed flow (v_1), as discussed in Chapter ??.

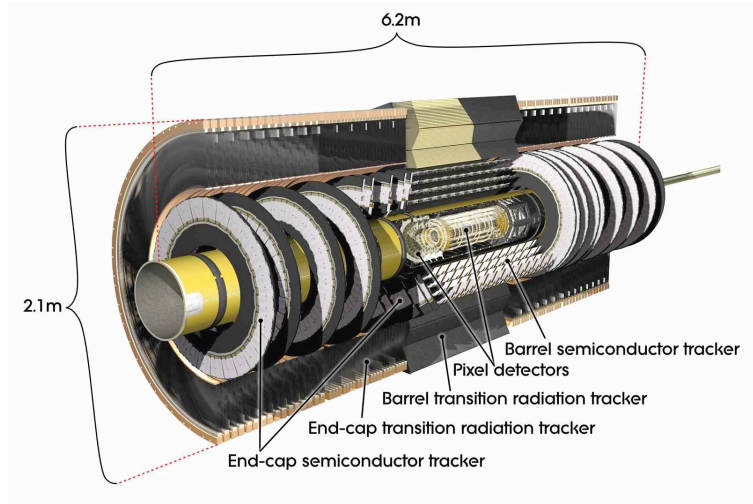


Figure 5.3: Layout of the ATLAS Inner Detector, with the Pixel detector, SCT detector, and TRT indicated.

The ATLAS Inner Detector (ID) has been designed to track charged particles in 5 units of

pseudo-rapidity centered around mid-rapidity [27]. The detector combines three technologies, closest to the beam, tracking is done with silicon pixel detectors (Pixel) arrayed in a barrel with three layers (B-layer, Layer 1 and Layer 2) and 6 end-cap sections. The Pixel end-cap sections are mounted on disks perpendicular to the beam axis and placed on both sides of the nominal interaction point. The Pixel detector is followed by the Semiconductor Tracker (SCT) consisting of double-sided silicon strip detectors arranged in four layers in the barrel, and two sets of 9 end-cap disks located on both sides of the nominal interaction point. The third tracking detector is a Transition Radiation Tracker (TRT) based on drift tubes arranged in a barrel and 2 endcaps. The ID was designed with an high granularity to cope with the high luminosity expected in p+p collisions, which leads to multiple p+p collisions in each LHC bunch crossing. The granularity turns out to be essential for tracking charged particles produced in the high-multiplicity environment of heavy ion collisions in a wide pseudo-rapidity window.

5.3 Determination of the collision centrality

The event-by-event characterization of centrality is a fundamental observable in heavy ion physics, since most global observables closely track the event geometry as controlled by the impact parameter (the distance b between the centers of the two colliding nuclei). A simple example is the charged particle multiplicity which predominantly scales proportionally to the number of participating nucleons (N_{part}), but has sub-dominant contributions that seem to scale proportionally to the number of binary collisions (N_{coll}). This simple fact implies that the total energy will correlate very tightly with any of the three standard event centrality observables (N_{part} , N_{coll} and b). Figure 5.4 shows in the top panel the correlation between the energy deposited in electromagnetic (EM, $|\eta| < 3.2$), hadronic (HAD, $|\eta| < 3.2$) and forward calorimeters (FCAL, $3.2 < |\eta| < 4.9$) and the collision centrality as measured by N_{coll} , N_{part} and b for HIJING Pb+Pb collisions at $\sqrt{s_{NN}} = 5.5$ TeV. The HIJING [42] simulated events include the ATLAS detector response obtained with a full Geant4 simulations [43]. The energy is particularly large in the FCAL due to the longitudinal boost of forward-going particles ($E \sim m_T \cosh(y)$). A monotonic correlation between the energy deposited in various calorimeter systems and the centrality parameters can be seen. Similar strong correlation with centrality is observed for silicon clusters recorded in the pixel and strip detectors ($|\eta| < 2.5$).

The strong correlation implies that one can bin each of these variables into percentile bins, each corresponding to 5% of the total cross-section (i.e. the most central 0-5% events, 5-10%, etc.), and relate these to similar percentages of the N_{part} , N_{coll} and b distributions. This is a standard technique used by all heavy ion experiments [44], which only requires the multiplicity or energy depositions to vary monotonically with the impact parameter. Ultimately the limiting factor in a precise estimation is the uncertainty in knowing what fraction of the total inelastic A+A cross section is sampled by the experimental trigger, something that is difficult for all LHC experiments. However, if one assumes this can be determined precisely, then one can bin the HIJING variables and extract the width of the centrality variable distributions in each bin, as shown in the bottom panel Fig.5.4. One can see that for a wide centrality range, the parameters are estimated with an accuracy of the order of 10%.

The Zero Degree Calorimeter (ZDC), discussed in Chapter ??, will also be an important contribution to the characterization of event centrality. Most importantly, it will provide a high efficiency

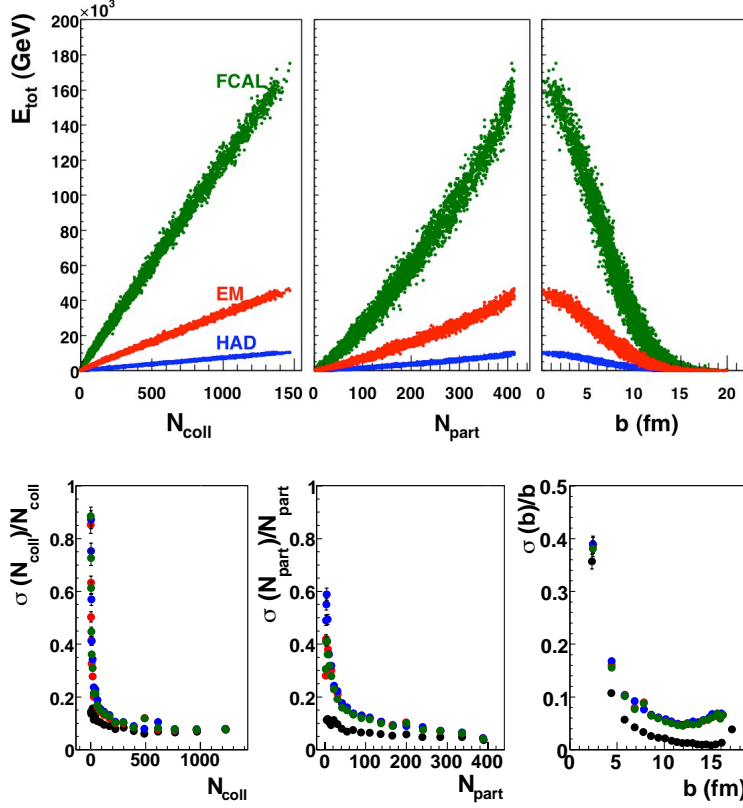


Figure 5.4: (top panel) Correlation of the total energy measured by the FCAL (top), EM calorimeter (middle), and Hadronic Calorimeter (bottom) correlated with N_{part} , N_{coll} and impact parameter (b). (bottom) Normalized width of distributions of N_{part} , N_{coll} and b , corresponding to bins in E_{tot} for FCAL, EM, and HAD. Filled black circles correspond to the cuts made directly on the centrality variable (N_{coll} , N_{part} or b), red (blue, green) correspond to the cuts on the total energy deposited in EM (HAD, FCAL) calorimeter.

minimum bias event trigger for Pb+Pb collisions, which will be important for reducing the systematic errors on centrality observables. It will also provide the total spectator energy, which should anti-correlate with the energies in the other ATLAS calorimeters, thus verifying the assumption that the multiplicity or energy deposition varies monotonically with the impact parameter.

5.4 Charged particle multiplicity measurements

The measurements of the primary charged particle pseudo-rapidity density, $dN_{ch}/d\eta$, as a function of the collision centrality will be performed at the start of the LHC running with heavy-ion beams. These measurements will provide crucial information on the underlying physics and determine the initial energy and entropy densities. In addition charged particle multiplicities are also sensitive to dynamical effects like jet quenching and nuclear shadowing.

The measurement of $dN_{ch}/d\eta$ can be performed with the silicon tracker of the ATLAS detector, covering pseudo-rapidity range $|\eta| < 2.5$. While it would be desirable to use the standard ATLAS tracking algorithms to estimate the total yield of charged particles, two issues arise. The first is simply that the algorithms have not yet been optimized for tracks lower than $p_T < 400$ MeV. The second is that while tracks can be reconstructed, as shown in the previous section, there is a substantial fake rate, which will have to be tuned using detailed Monte Carlo simulations. Beyond this, it is desirable to have a method which requires fewer choices than the standard tracking, in order to rapidly measure the track densities in real data under the tight time constraints of early minimum bias running. The limits of the tracking system to register particles at low values of transverse momentum ?? require the use of different approaches, of varying redundancy.

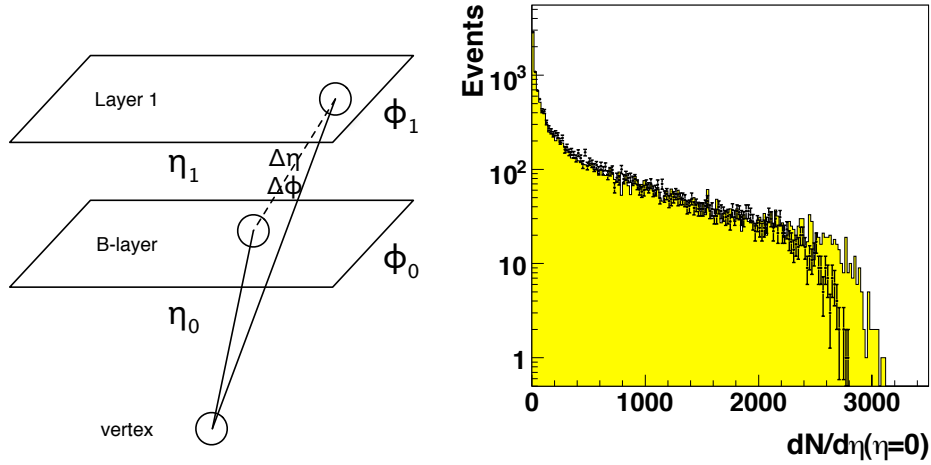


Figure 5.5: (left) Schematic diagram showing how tracklets are defined (right). Distribution of $dN_{ch}/d\eta$ from HIJING events (open histogram) and reconstructed using the tracklet method event-by-event, but without efficiency corrections (yellow histogram)

One approach which can be used to reduce the complexity of the problem is the “tracklet” method, most notably used in heavy ion collisions by the first PHOBOS paper [45]. As shown in the left panel of Fig. 5.5, the idea is to use the event vertex (determined by whatever means are available, e.g. with higher p_T tracks), and use this to seed vectors based on correlated hits in the first two Pixel layers (B layer and Layer 1). A tracklet is thus a three point track characterized by the event vertex, the η and ϕ of the hit in the inner-most pixel layer, and residuals $\Delta\eta$ and $\Delta\phi$ between that hit and a hit in Layer 1. The residuals are used both to cut away non-correlated hits (in this case $\Delta\eta < 0.08$ and $\Delta\phi < 0.8$), as well as to estimate the track momentum in low-multiplicity events. The set of tracklets selected by this method can then be used to estimate the particle density, with very little background. A distribution of the uncorrected number of tracklets integrated over $|\eta| < 1$ compared with HIJING truth is shown in the right panel of Fig. 5.5. This shows that even without efficient correction, the tracklet method gives a good estimate to the event-by-event multiplicity, allowing the study of fluctuations as well as mean values.

Efficiency is largely controlled by the efficiency of the silicon detector, which is very high.

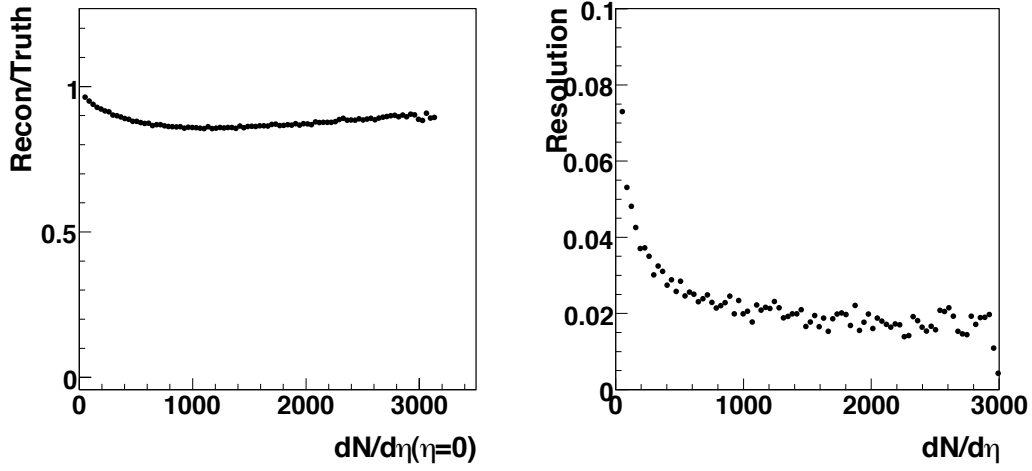


Figure 5.6: (left) Tracklet resolution at $|\eta| < 1$ for raw MC and reconstructed simulation data. (right) Multiplicity distribution

However, although using three hits in addition to the primary vertex provides some redundancy, a large occupancy (e.g. as one might expect in heavy ion collisions) can lead to fake tracks, especially when choosing only the closest hit in Layer 1 for each hit in Layer B. To estimate this, an equivalent sample of truth tracks is extracted by looking at stable charged hadrons (proton, pion and kaon). The η , ϕ and p_T are all relevant for this study. Comparisons of the total yield (integrated over all p_T and within $|\eta| < 1$) relative to the MC truth are shown in Fig.5.6.

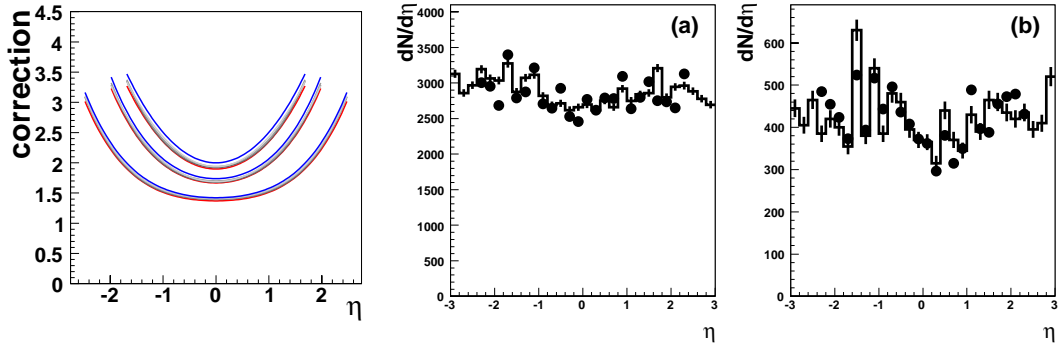


Figure 5.7: Correction functions for the three pixel layers from samples of Pb+Pb collisions with different centralities. For each band, corresponding to the pixel layer, the low curve is for the most central sample ($b = 2$ fm), and the upper curve is for the most peripheral sample ($b = 10$ fm), while functions derived for all other samples fall in the area between these two curves (left). Comparison of the reconstructed charged particle density distribution obtained from the first pixel layer clusters (dots) with the true distribution (histogram) for a central event with $b = 2$ fm (middle) and peripheral event with $b = 10$ fm right).

The another approach was to use the clusters reconstructed in the silicon pixel layers. The clustering procedure accounts for the fact that a charged particle traversing the detector usually leaves signal in more than one pixel. The pseudo-rapidity distribution of the clusters shows a significant excess as compared to the generated distribution of the primary charged particles. This excess can be attributed to particles originating in secondary interactions and the effects of the magnetic field. Therefore, in order to extract pseudo-rapidity distribution of the primary particles, the Monte Carlo based correction factors had to be applied. These correction factors are defined as

$$C(\eta) = \frac{(dN_{ch}/d\eta)_{rec}}{(dN_{ch}/d\eta)_{true}}. \quad (5.3)$$

They have been calculated for five samples of simulated HIJING Pb+Pb collisions with impact parameters $b = 2, 5, 7, 8$ and 10 fm for each of the three pixel layers. A smooth functional dependence was fitted to the calculated $C(\eta)$. The shape of the correction function reflects the distribution of the material in the detector, indicating that secondary particle production gives dominant contribution to the observed excess in the $dN_{ch}/d\eta$ distribution of pixel clusters. Thus-determined correction functions weakly depend on centrality (variation within less than 5%), as illustrated in Fig. 5.7.

The correction functions were then used in the reconstruction of $dN_{ch}/d\eta$ distributions on an event-by-event basis for events with different centralities. Examples for the two such events with impact parameters $b = 2$ and $b = 10$ fm are shown in Fig. 5.7 together with the comparison to the true distribution for primary charged particles. The estimated reconstruction errors are of the order of 10-15%. Previously [22], we have also shown that with this reconstruction method we can correctly reproduce much higher particle densities as well as variations in the shape of the $dN_{ch}/d\eta$ distribution.

5.5 Transverse energy measurements

The transverse energy flow as a function of pseudo-rapidity should also provide insight into the dynamics of nucleus-nucleus collisions. The hermetic and granular calorimetric system of the ATLAS detector allows for measuring energy depositions in a wide range of pseudo-rapidity, out to $|\eta| = 5$, including both electromagnetic (EM) and hadronic (HAD) energy. The simplest method for extracting $dE_T/d\eta$ uses sum of calibrated transverse energies deposited in calorimetric cells calculated as a function of η . The correction factors for acceptance cracks and energy deposits from particles produced in interactions with the detector material should be applied. They can be calculated as $(dE_T/d\eta)_{rec}/(dE_T/d\eta)_{true}$, thus in a similar way as correction factors used to derive $dN_{ch}/d\eta$ (see Section 5.4). They have been calculated for samples of events with different centralities and were found to be independent of centrality. The final corrections, averaged over all centralities, are then applied in the reconstruction of $dE_T/d\eta$ for single events. Figure 5.8(left) shows as an example the comparison of the corrected measured $dE_T/d\eta$ with the generated one for a single Pb+Pb event with $b = 2.3$ fm. A good agreement can be seen in the pseudo-rapidity range $|\eta| < 4.9$.

We have applied also another method which is independent of the Monte Carlo corrections and is based on the use of the algorithm developed to reconstruct the missing transverse energy

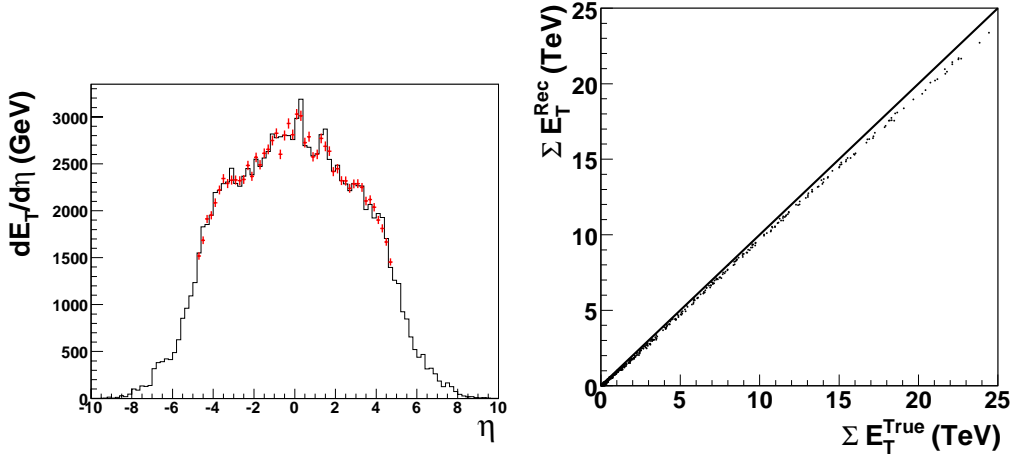


Figure 5.8: Comparison of the reconstructed $dE_T/d\eta$ distribution (points) with the true distribution (histogram) for a central event with $b = 2.3$ fm (left), and the reconstructed total transverse energy in $|\eta| < 4.9$ (dots) versus the true one (right).

in pp collisions [46]. With this algorithm the total transverse energy (ΣE_T) is calculated summing calibrated energy deposits of all calorimeter cells that survive the noise cut. The energy of the reconstructed muons in the muon spectrometer is also accounted for and the corrections for the energy loss in the detector material are applied. With this method we can reproduce the total transverse energy in $|\eta| < 4.9$ with an accuracy better than 10%.

5.6 Elliptic flow

When two nuclei collide with non-zero impact parameter, the initial spatial anisotropy of the overlapping region leads to a momentum anisotropy in the final state, providing that the system evolves collectively with significant re-interaction between produced particles. This anisotropy arises due to the pressure gradients built in the initial stage of the system evolution. The stronger pressure gradients in the direction of the reaction plane (shorter axis of the overlap almond-like region) lead to a preferential in-plane particle emission. This final state momentum anisotropy can be quantified by studying the Fourier decomposition of particles' azimuthal angle distribution:

$$E \frac{d^3N}{dp^3} = \frac{1}{2\pi} \frac{d^2N}{dp_T^2 dy} \left(1 + 2 \sum_{n=1}^{\infty} v_n \cos [n(\varphi - \Phi_{RP})] \right), \quad (5.4)$$

where φ is the azimuthal angle of the particle and Φ_{RP} denotes the azimuthal angle of the reaction plane defined by the impact parameter, (\vec{b}), and the beam axis (z). The second Fourier coefficient, $v_2 \equiv \langle \cos 2[n(\varphi - \Phi_{RP})] \rangle$, referred to as elliptic flow, measures the elliptical shape of the distribution of particles' momenta in the transverse plane.

Widely used standard method [47] of measuring the final state azimuthal anisotropy requires the estimation of the azimuthal angle of the reaction plane, Φ_{RP} , which is not directly measurable.

The knowledge of the reaction plane is also important for other than elliptic flow studies, like e.g. jet quenching. Therefore, in the next sub-section we discuss the procedure to estimate the reaction plane. Then, the methods used to reconstruct elliptic flow signal are described.

The analysis is based on the HIJING generated events with implemented flow effects via redistribution of the particles' azimuthal angles in order to get the desired elliptic flow signal. Several fully simulated event samples with different flow effects have been produced. These include samples with the flow signal dependent on centrality, pseudo-rapidity and transverse momentum as deduced from the RHIC data extrapolated to the LHC energy. For this input flow signals five centrality selections were applied by fixing the impact parameter values within the range from 2.3 fm up to 10.7 fm. In addition several samples with constant flow values of 3%, 5% and 10% have been also simulated for different centralities of Pb+Pb collisions.

5.6.1 Reaction plane reconstruction

Anisotropic effects are due to a truly collective motion which means that the emission of every produced particle in a given event is correlated with the reaction plane of that event. This multi-particle correlation gives rise to the inter-particle correlations providing the basis for the estimate of the reaction plane. For each event we determine the angles, conventionally called event plane angles:

$$\Psi_n = \frac{1}{n} \tan^{-1} \left(\frac{\sum w_i \sin(n\varphi_i)}{\sum w_i \cos(n\varphi_i)} \right), \quad (5.5)$$

where the sums run over all particles in an event. The weights, w_i , are introduced to account for some acceptance biases and to get the best estimate of the Φ_{RP} , e.g. for calorimetric measurements the weights are taken as $w_i = E_{T,i}$. The flow signal, v'_n , measured using the n^{th} harmonic event plane, Ψ_n , is then given as: $v'_n = \langle \cos n(\varphi_i - \Psi_n) \rangle$, where the brackets denote average over all particles in all events. An event plane angle of each order fluctuates around the true reaction plane angle, Φ_{RP} , due to the finite particle multiplicity. Thus, the flow value, v'_n , has to be corrected by the reaction plane resolution, $\langle \cos n(\Psi_n - \Phi_{RP}) \rangle$. The correction is found by calculating an event plane angle in two distinct sub-event regions, N and P , in every event, where for example sub-event N covers $\eta < 0$ while sub-event P covers $\eta > 0$. The following relation between the two event plane angles, Ψ_n^N and Ψ_n^P and the reaction plane resolution holds if any correlations not due to flow are assumed to be negligible:

$$\langle \cos[n(\Psi_n^N - \Psi_n^P)] \rangle = \langle \cos[n(\Psi_n^N - \Phi_{RP})] \rangle \langle \cos[n(\Psi_n^P - \Phi_{RP})] \rangle. \quad (5.6)$$

When the two sub-events have similar multiplicity then the resolution correction for each sub-event is

$$R \equiv \langle \cos[n(\Psi_n^N - \Phi_{RP})] \rangle = \langle \cos[n(\Psi_n^P - \Phi_{RP})] \rangle = \sqrt{\langle \cos[n(\Psi_n^N - \Psi_n^P)] \rangle}, \quad (5.7)$$

and the resolution corrected flow signal:

$$v_n = \frac{v'_n}{\sqrt{\langle \cos[n(\Psi_n^N - \Psi_n^P)] \rangle}}. \quad (5.8)$$

For the subsequent study of the elliptic flow the order n in the above equations should be substituted by 2.

With the ATLAS detector, the reaction plane angle and its resolution can be determined using different detector sub-systems since all of them have a complete 2π coverage in the azimuthal angle. Table 5.1 shows the reaction plane resolution obtained with different detector sub-systems for the sample of simulated Pb+Pb collisions with constant flow of 5% for the three centrality classes: peripheral, $b = 10 - 12$ fm, more central, $b = 6 - 8$ fm, and central, $b = 2 - 4$ fm. One can see that resolution corrections are small (not very different from unity) particularly for central collisions. The resolution worsens for more peripheral events, but still corrections are not unreasonably large.

Sub-system	η - coverage for sub-events	Resolution correction		
		$b = 10 - 12$ fm	$b = 6 - 8$ fm	$b = 2 - 4$ fm
EM-Barell1	$0.2 < \eta < 1.5$	0.29 ± 0.06	0.70 ± 0.02	0.81 ± 0.01
EM-EndCaps	$1.5 < \eta < 3.2$	0.57 ± 0.03	0.88 ± 0.01	0.93 ± 0.01
HAD-EndCaps	$1.6 < \eta < 3.2$	0.25 ± 0.07	0.59 ± 0.03	0.74 ± 0.02
FCAL0	$3.1 < \eta < 4.8$	0.60 ± 0.03	0.89 ± 0.01	0.93 ± 0.01
Pixel, 1st layer	$0.2 < \eta < 2.6$	0.56 ± 0.03	0.87 ± 0.01	0.92 ± 0.01
SCT, 1st layer	$0.2 < \eta < 1.6$	0.36 ± 0.05	0.71 ± 0.01	0.76 ± 0.01
Reconstructed tracks	$0.2 < \eta < 2.0$	0.45 ± 0.04	0.85 ± 0.01	0.92 ± 0.01

Table 5.1: Resolution corrections calculated for different sub-systems for the simulated events with different centralities and with the constant flow of 5%.

For illustration Fig. 5.9 shows the distribution of the difference between the true reaction plane and the event plane angle, $\Delta\varphi = \Phi_{RP} - \Psi_2^N$, where the event plane angle is determined from the different detector sub-systems.

The systematic study of the event plane resolution have been performed for all simulated samples. The best resolution (correction close to unity) is obtained, as expected, for the samples with stronger flow signal, i.e. 10% constant flow or using the sample of central events with a flow signal extrapolated from RHIC data.

5.6.2 Elliptic flow reconstruction from the event plane method

As discussed in the previous section, the elliptic flow parameter, v_2 , is obtained from Eq. 5.8 with $n = 2$:

$$v_2 = \frac{v'_2}{\sqrt{\langle \cos[2(\Psi_2^N - \Psi_2^P)] \rangle}}. \quad (5.9)$$

As mentioned before, two separate sub-event regions, N and P , are used to find the event plane angles, Ψ_2^N and Ψ_2^P (see also Table 5.1). In order to avoid autocorrelations, the flow signal, v'_2 is measured for signals recorded in the $P(\eta > 0)$ hemisphere with respect to the event plane angle determined from the $N(\eta < 0)$ hemisphere and vice versa. With the suit of detectors pos-

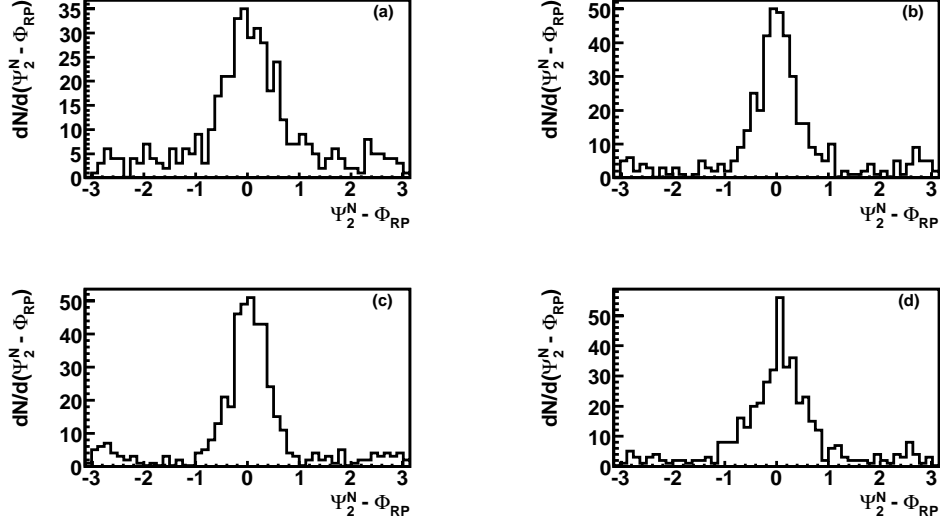


Figure 5.9: Distribution of the difference, $\Delta\varphi = \Psi_2^N - \Phi_{RP}$, where Ψ_2^N is obtained from EM-Barrel1 (a), FCAL0 (b), pixel layer 1 (c), and from the reconstructed tracks with $p_T > 0.5$ GeV/c (d).

sessing the full azimuthal symmetry, we can reconstruct the flow with different combinations of the detectors used for the event plane estimate and the flow signal measurement.

As an example we show the analysis in which the flow is calculated from azimuthal angles of pixel clusters from the innermost pixel layer while the event plane angle is calculated from the energy weighted azimuthal angles of the calorimetric cells in the first layer either of the electromagnetic barrel or of the forward calorimeter. Fig. 5.10 shows the azimuthal angle distributions of the silicon clusters measured with respect to Ψ_2 for peripheral ($b = 10 - 12$ fm) data samples with input v_2 of 3%, 5% and 10%. A clear flow signal can be visible, more pronounced for the samples with stronger input flow. For these samples with the constant flow values, the reconstructed flow signal was correctly found to be independent of the event multiplicity, pseudo-rapidity, and transverse momentum.

Method		Input v_2		
		0.03	0.05	0.10
pixel clusters (φ) FCAL0 (Ψ_2)	v_2^{rec}	0.018 ± 0.003	0.034 ± 0.002	0.070 ± 0.002
	v_2^{rec} / v_2^{true}	0.60 ± 0.10	0.68 ± 0.04	0.70 ± 0.02
tracks (φ) FCAL0 (Ψ_2)	v_2^{rec}	0.031 ± 0.004	0.047 ± 0.003	0.100 ± 0.002
	v_2^{rec} / v_2^{true}	1.00 ± 0.10	0.94 ± 0.06	1.00 ± 0.02

Table 5.2: Resolution corrected v_2 averaged over $|\eta| < 2$ obtained from pixel clusters and reconstructed tracks.

In the Table 5.2 we show the resolution corrected reconstructed flow signal from this analysis,

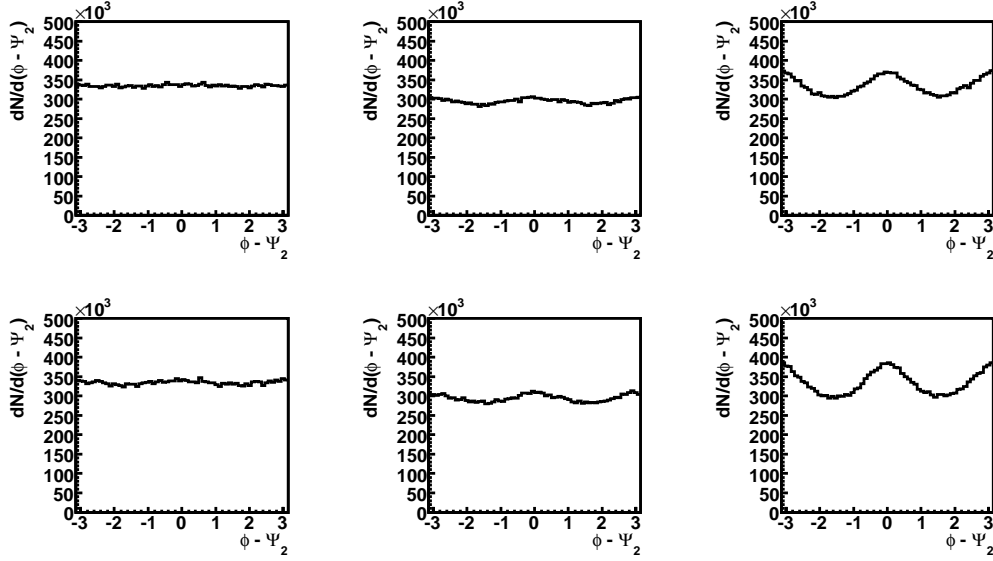


Figure 5.10: Distribution of $\phi - \Psi_2$, where ϕ is the azimuthal angle of pixel clusters and Ψ_2 is obtained from EMB1 (upper panel) or FCAL0 (lower panel) for the simulated data with 3% (left column), 5% (middle column) and 10% (right column) constant input flow.

v_2^{rec} , averaged over $|\eta| < 2$. The ratios of the reconstructed to the true flow value are also listed. One can see that using silicon clusters we underestimate the flow signal, by about 30%. This underestimation is approximately independent of the magnitude of the flow signal. The Monte Carlo corrections are needed to account for this suppression. The dilution of the flow calculated with pixel clusters is due to the signals not correlated with the reaction plane.

The elliptic flow can be also studied with the reconstructed tracks. This imposes the limit on the lowest transverse momentum of 0.5 GeV/c. Lower part of Table 5.2 shows the resolution corrected elliptic flow signal calculated for the azimuthal angles of the reconstructed tracks, averaged over $|\eta| < 2$ for the three samples of simulated events with constant flow. One can see that the input flow signal is well reproduced (within 10%), and there is no need for other than the event plane resolution corrections.

Fig. 5.11 shows the comparison of the reconstructed and the true v_2 values as function of pseudorapidity for a sample of peripheral Pb+Pb collisions with generated flow of 5%. A good agreement between the generated and reconstructed magnitude of the flow signal calculated from the reconstructed tracks shows our capability of measuring differential flow effects with a very good accuracy in peripheral collisions. On the contrary, using pixel clusters and energy depositions in the forward calorimeters results in underestimation of the flow magnitude, a similar effect as observed for the integrated flow studies (see Table 5.2).

Transverse momentum dependence was also studied for samples with different centralities and with the generated flow in agreement with the extrapolation of RHIC data. Results are shown in Fig. 5.15, in comparison to the input flow signal and results obtained from other analysis methods. For peripheral collisions the event plane method correctly reproduces the generated

flow in a wide range of particle transverse momenta. For central collisions, we observe that the reconstructed flow signal is larger than the generated one, especially for low transverse momenta. This effect is likely due to the large contribution of fake tracks among the reconstructed tracks in central Pb+Pb collisions. The ongoing work on the optimization of the tracking algorithm should result in the reduction of fake tracks, and consequently a better agreement between the true and reconstructed flow signals for central collisions.

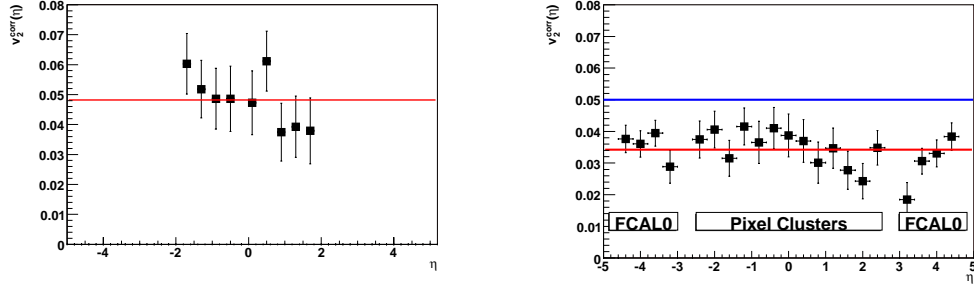


Figure 5.11: Pseudorapidity dependence of the reconstructed elliptic flow signal calculated from reconstructed tracks (left) and from pixel clusters and forward calorimetric cells (right) for a sample of peripheral events ($b = 10 - 12$ fm) with input flow of 5%. The reaction plane was estimated from signals in the first layer of forward calorimeters.

5.6.3 Elliptic flow from two-particle correlations

A method, alternative to the event plane method, uses the Fourier decomposition of the distribution in the azimuthal angle difference, $\Delta\varphi = \varphi_1 - \varphi_2$, between pairs of charged particles [48, 49]:

$$\frac{dN_{ch}}{d\Delta\varphi} \propto (1 + \sum_{n=1}^{\infty} 2v_n^2 \cos(n\Delta\varphi)). \quad (5.10)$$

The method allows the determination of the elliptic flow without event-by-event estimation of the reaction plane and can be used when the azimuthal coverage of the detector is not complete. In this analysis the reconstructed charged particles tracks, with $|\eta| < 2$ and $p_T > 0.5$ GeV, are used to form pairs. A two-particle azimuthal correlation function is defined as

$$C(\Delta\varphi) = \frac{N_{corr}(\Delta\varphi)}{N_{uncorr}(\Delta\varphi)}, \quad (5.11)$$

where $N_{corr}(\Delta\varphi)$ is the $\Delta\varphi$ distribution for charged particle pairs observed in the same event, and $N_{uncorr}(\Delta\varphi)$ is the $\Delta\varphi$ distribution for particle pairs which are formed from the two tracks selected from different events. Centrality dependence of the two-particle correlation function is illustrated in Fig. 5.12 for samples with input flow of 5%. The reconstructed magnitudes of the elliptic flow signal, obtained from fits to $C(\Delta\varphi)$ are listed in Table 5.3. One can see that the input flow is well reconstructed in peripheral collisions, although with large statistical errors. Obviously

much higher statistics is needed for the study of two-particle correlations. For more central collisions ($b = 6 - 8$ fm) the reconstructed v_2 is significantly larger than the input value of 5%. Even stronger effect is observed for collisions with impact parameter ranging from 2 to 4 fm. Clearly, the two-particle correlation method is very sensitive to autocorrelations induced by high level of falsely reconstructed tracks.

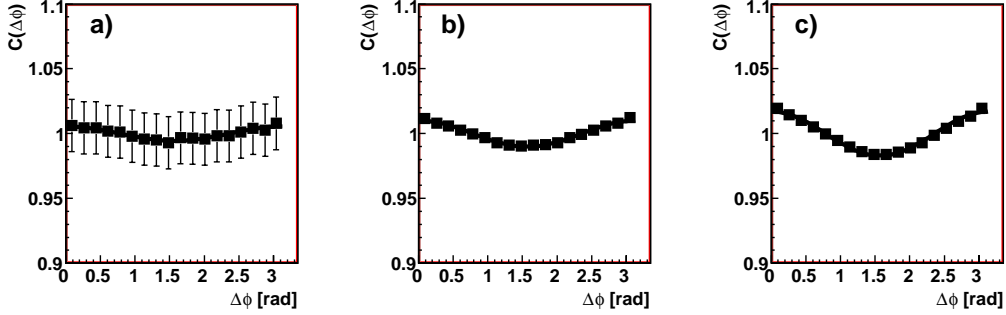


Figure 5.12: Correlation functions for samples with input flow of 5% and impact parameter range (a) $b = 10 - 12$ fm, (b) $b = 6 - 8$ fm and (c) $b = 2 - 4$ fm.

b range [fm]	Input v_2	Reconstructed v_2
10 - 12	3%	4.0 ± 4.0
10 - 12	10%	9.0 ± 2.0
10 - 12	5%	5.0 ± 3.0
6 - 8	5%	7.1 ± 0.4
2 - 4	5%	9.2 ± 0.1

Table 5.3: Elliptic flow obtained from the two-particle correlation method for different samples of Pb+Pb collisions.

The two-particle correlation method was also used to study the p_T dependence of the flow magnitude for samples of events with different centralities and with the generated elliptic flow as extrapolated from RHIC data. Results are shown in Fig. 5.15. Similar conclusions as those related to the event plane method can be drawn. For peripheral collisions the two-particle correlation method well reproduces the generated p_T dependence of the elliptic flow, while for more central collisions the reconstructed flow signal is larger than the true one, particularly at low transverse momenta due to autocorrelation effects induced by fake tracks.

5.6.4 Elliptic flow with the Lee-Yang Zeros method

The standard method for analyzing anisotropic flow, described above, is to correlate particles with an estimate of the reaction plane angle Φ_{RP} , where this estimate is obtained also from correlations

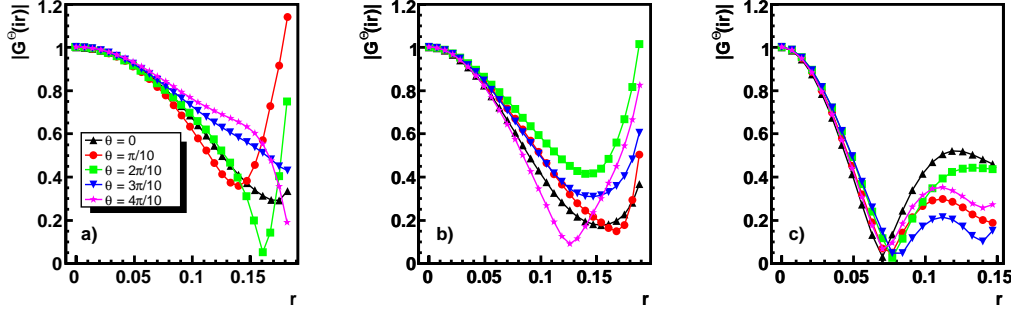


Figure 5.13: $|G^\theta(ir)|$ versus r for peripheral samples ($b = 10 - 12$ fm) with the generated v_2 of 3% (a), 5% (b) and 10% (c). In each plot the curves are calculated for different θ values as indicated in the legend.

among the produced particles. So essentially the global collective behavior is studied via two-particle correlations, which are sensitive to various non-flow correlations. The Lee-Yang Zeros method [50, 51] was proposed in order to extract flow effects from the correlations between a large number of particles, not influenced by non-flow correlations. The method is based on searching for minima in the complex plane of a generating function of azimuthal correlations, defined as:

$$G^\theta(ir) = \prod_{i=1}^{N_{ch}} [1 + irw_i \cos(2\phi_i - 2\theta)], \quad (5.12)$$

where r is a real positive variable, θ is an arbitrary angle in the range from 0 to $\pi/2$ and w_i are weights (in this study assumed to be equal 1). $|G^\theta(ir)|$ is plotted as a function of r for different θ values. The elliptic flow is directly determined by the location of the first minimum, r_0 :

$$v_2 \equiv \frac{j_{01}}{N_{ch}r_0}, \quad (5.13)$$

where $j_{01} \approx 2.405$ is the first root of the Bessel function $J_0(x)$. Fig. 5.13 shows the dependence of $|G^\theta(ir)|$ on r for samples of peripheral events and with constant input flow of 3, 5 and 10%. Similar dependencies, but for samples with different centralities and input flow of 5% are depicted in Fig. 5.14. Table 5.4 summarizes the elliptic flow values calculated from Eq. 5.13. In most cases the generated elliptic flow is well reproduced. Only for the sample of most central events the reconstructed v_2 is larger than the input v_2 , indicating that the method is not able to remove autocorrelations. For the sample of peripheral events ($b = 10 - 12$ fm) and low input v_2 (3%), the output $v - 2$ is determined with a large error, but in this case we reach the limit of Lee-Yang Zeros method applicability. Nevertheless, the performance of the Lee-Yang Zeros method is much better as compared to the two-particle correlation method (Table 5.3).

. The Lee-Yang Zeros method was also used to study the p_T -dependence of elliptic flow. The simulated data samples with different centralities and with the generated flow obtained from extrapolation of RHIC measurements were used in this study. The elliptic flow values obtained from this method are presented in Fig. 5.15, together with the results from the event plane method and

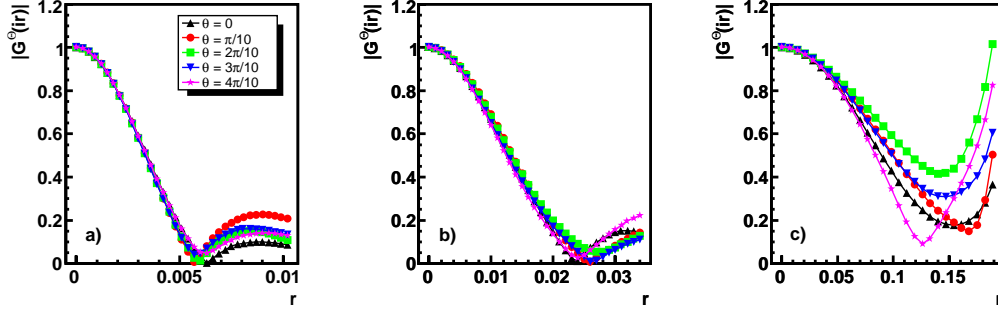


Figure 5.14: The same as in Fig. 5.13 for samples with constant input flow of 5% and different centralities: $b = 2 - 4$ fm (a), $b = 6 - 8$ fm (b) and $b = 10 - 12$ fm (c).

b range [fm]	Input v_2	Reconstructed v_2
10 - 12	3%	4.0 ± 1.0
10 - 12	10%	10.0 ± 0.3
10 - 12	5%	5.0 ± 0.9
6 - 8	5%	5.4 ± 0.2
2 - 4	5%	7.7 ± 0.2

Table 5.4: Elliptic flow obtained from the Lee-Yang Zeros method for different samples of Pb+Pb collisions.

from two-particle correlations, and compared to the generated $v_2(p_T)$ dependence. All methods give consistent results which reasonably well agree with the generated data for peripheral and mid-central Pb+Pb collisions. For the most central collisions all methods consistently overestimate the elliptic flow values in the range of $p_T = 0.5 - 1.0$ GeV. This discrepancy, as already discussed is due to the autocorrelation effect caused by tracking algorithm imperfections.

5.6.5 Outlook

The ATLAS detector offers an excellent capability of measuring azimuthal anisotropies in the transverse momentum distributions of produced particles. As have been shown here, various analysis methods can be applied, characterized by different efficiencies, dependency on Monte Carlo corrections and sensitivity to non-flow correlations. It is also planned to apply the method based on a cumulant expansion (up to the 4th order) of multi-particle correlations [52]. This method, as the method of Lee-Yang Zeros, does not require the estimate of the reaction plane and, to a large degree, allows the elimination of low-order non-flow correlations. A systematic comparison of various methods will provide a reliable estimate of the non-flow contribution and the measure of elliptic flow directly comparable to the hydrodynamic model calculations.

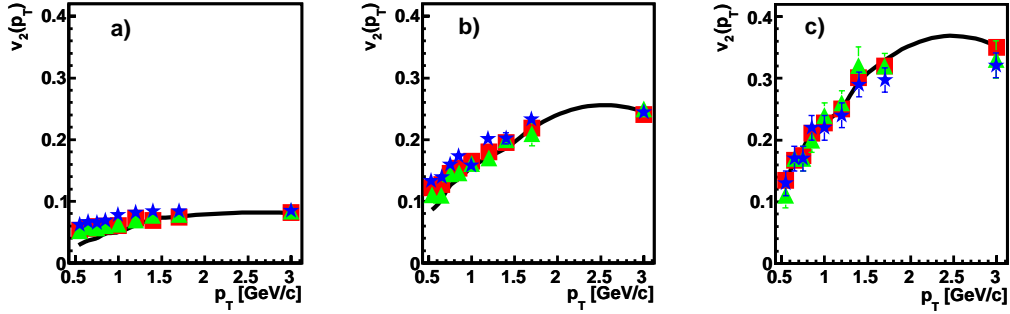


Figure 5.15: Transverse momentum dependence of the reconstructed v_2 from the event plane method (squares), two-particle azimuthal (stars) and the Lee-Yang Zeros methods (triangles) for Pb+Pb collisions with (a) $b = 2.3$, (b) 7.0 and (c) 10.7 fm.

5.7 Summary

We have shown that the ATLAS detector is well suitable for studying global observables in heavy ion collisions. Notice, that most of the discussed analysis techniques can be also applied for minimum-bias pp collisions and thus tested on the real data before the start of heavy-ion runs.

The centrality parameter for heavy-ion collisions can be estimated using the energy deposits in the central and forward calorimeters as well as signals or reconstructed tracks in the silicon tracker. Charged particle pseudo-rapidity density can be determined, on an event-by-event basis, using the innermost pixel layer with an accuracy of about 10% in the η range from -2.5 to 2.5 . The transverse energy flow $dE_T/d\eta$ and the total transverse energy can also be precisely measured in single events over the broad η range.

The measurements of the collective particle flow can be performed using various analysis techniques and different detector sub-systems. An attractive possibility, not yet studied in detail, is to measure the elliptic flow of photons, which can be separated from hadrons thanks to the fine transversal and longitudinal segmentation of the electromagnetic calorimeter. The another possibility, left for the future studies, is the potential measurement of the elliptic flow fluctuations.

Chapter 6

Jet Reconstruction

This chapter describes the physics motivation for complete jet measurements in heavy ion collisions at the LHC extending the discussion from the introduction, and shows results for ATLAS jet reconstruction performance in Pb+Pb collisions. It also shows results on measurements of jet fragmentation properties, di-jet correlations, and heavy-flavor tagged jets.

6.1 Physics motivation

As emphasized in Chapter 1, a major aspect of the heavy ion physics program at the LHC is the extension and clarification of the understanding of the effects of hot, dense QCD matter on hard probes, specifically jets. Prior to RHIC startup, several groups predicted the energy loss of a fast-moving, colored parton traversing a colored medium via perturbative gluon bremsstrahlung and multiple elastic scattering, leading to “jet quenching” [53, 54].

Evidence for this pQCD energy loss has been established through the measurement of high- p_T single particle suppression [55]. The suppression is quantified by the nuclear modification factor, R_{AA} , defined as the ratio of single particle yields in Au+Au collisions, Y_{Au+Au} , compared to p+p single particle rates, Y_{p+p} , scaled by the number of binary nucleon-nucleon collisions (N_{coll}):

$$R_{AA} = \frac{Y_{Au+Au}}{\langle N_{coll} \rangle Y_{p+p}}. \quad (6.1)$$

The nuclear modification factor for three different particle species, measured by PHENIX, is shown in the left panel of Fig. 6.1: direct photons, which do not strongly interact in the nuclear medium, are not suppressed while a factor of 5 suppression is measured in π^0 and η production. The level of π^0 suppression is apparently consistent with a particular pQCD energy loss model [56]. However, it has been argued, many models of energy loss can describe this data even when the details of the mechanism and implementation differ greatly between those models[57].

Further evidence for jet quenching comes from the azimuthal correlation of two high- p_T particles. These serve as a proxy for direct jet reconstruction, which is difficult at RHIC due to the high-multiplicity underlying event. Two-particle correlations in p+p suggest that high- p_T particle production is dominated by hard scattering [6, 60]. Two high- p_T particles from the trigger jet are correlated at $\Delta\phi \sim 0$ while two high- p_T particles at $\Delta\phi \sim \pi$ are fragments from a di-jet pair. Such

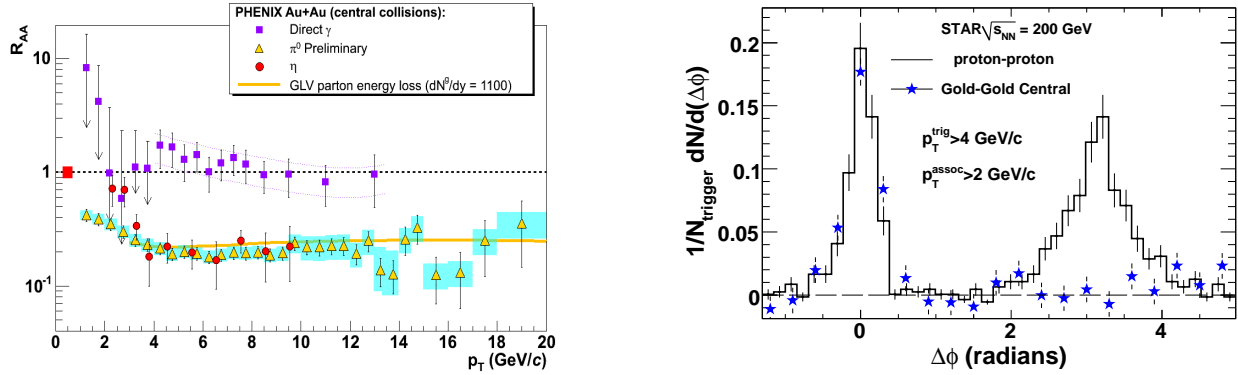


Figure 6.1: (left) Nuclear modification factor for direct photons, π^0 , and η [58]. $R_{AA} < 1$ is evidence of jet energy loss. (right) Azimuthal angle ($\Delta\phi$) correlations of two high- p_T charged hadrons [59] with trigger hadron $p_T > 4$ GeV/c and associated hadron $p_T > 2$ GeV/c. The recoil jet (at $\Delta\phi \sim \pi$) is strongly suppressed in central Au+Au compared to p+p correlations [6].

correlations are seen in the histogram on the right panel of Fig. 6.1. Measurements of these correlations in Au+Au indicate a substantial suppression of the recoil jet at $\Delta\phi \sim \pi$ while the trigger jet is essentially unmodified, as shown by the blue stars. These results suggest that the trigger jet originates from the surface of the interaction region and is unaffected by the nuclear environment while the recoil jet traverses a significant length in the medium and appears to be largely absorbed [6].

In addition to the suppression of light quarks and gluons, a quantitatively similar suppression of single, non-photonic electrons, dominantly from charm and bottom quark decays, has been observed (see the left panel of Fig. 6.2) [62, 5]. Since the heavy quark mass kinematically suppresses forward gluon radiation (a phenomenon known as the “dead cone”), heavy quark energy loss was expected to be much less than that for light quarks [63]. A comparison of the fractional energy loss from collisions and radiation of different quark species expected at the LHC is shown in the right panel of Fig. 6.2. Unfortunately, interpretation of the single, non-photonic electron suppression is not straightforward. Large uncertainties arise in calculating the charm cross-section in next-to-leading-log (NLL). Therefore, a theoretical understanding of the relative contribution of charm and bottom at a fixed electron p_T is not well constrained. Experimentally several early measurements of the charm-to-bottom ratio exist, but suffer from large statistical and systematic uncertainties.

Since these initial discoveries of energy loss of high- p_T particles, measurements sensitive to the medium’s response have been made utilizing jets as probes of the medium. As shown in the left panel of Fig. 6.3, lower- p_T azimuthal correlations in Au+Au show a yield peaked at $\Delta\phi \sim \pi \pm 1.1$ rad as a “shoulder”, non-existent in p+p and d+Au [24]. One possible explanation of this additional yield at these large angles is the existence of a Mach cone generated by a supersonic jet traversing the medium [64, 65]. The Mach angle is fixed by the speed of sound in the medium and, therefore, should not depend on the p_T of the particles, consistent with recent RHIC data [66]. The “shoulder” position shows a common centrality dependence at different collision energies and for different colliding species. Because the medium is similar for the energies and species considered, this indicates that the effect is a universal property of the produced medium, like the speed of

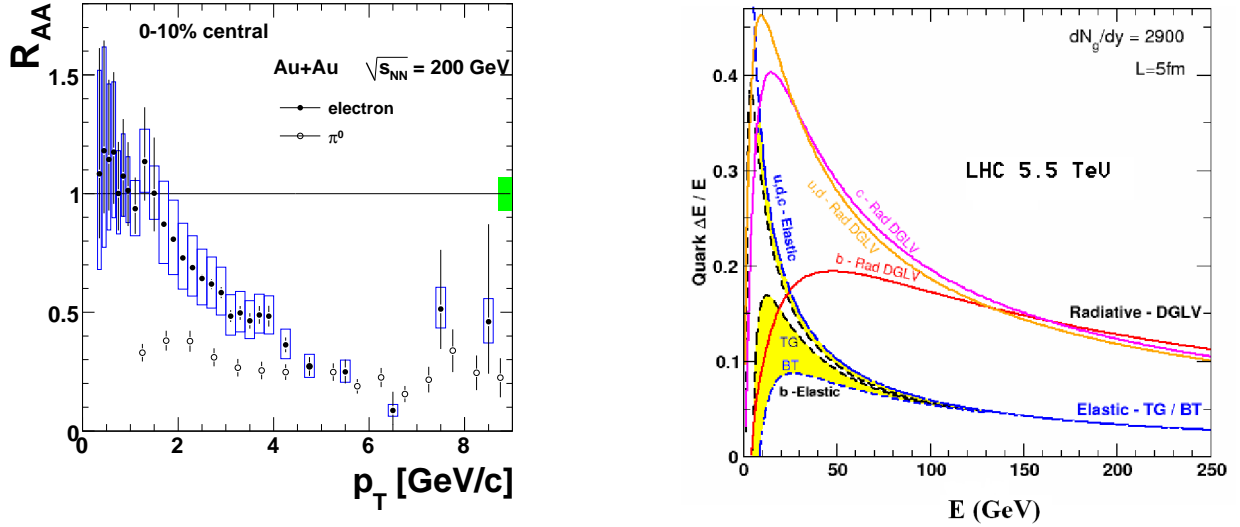


Figure 6.2: (left) The measured single particle suppression for non-photonic electrons (mainly from semi-leptonic decay of charm and bottom mesons) and π^0 s from PHENIX Collaboration [5]. (right) The calculated radiative and collisional energy loss in $\Delta E/E$ for various flavor of quarks at the LHC from Ref [61].

sound, which would be similar across energies and geometries. Three-particle correlations, which are sensitive to differences between conical emission and bent/deflected jets, are consistent with conical emission[67, 68].

The right panel of Fig. 6.3 shows two-particle correlations in $\Delta\phi$ and $\Delta\eta$, which reveal an extended “ridge” in η associated with the trigger jet [69]. In fact, this ridge may extend over least 4 units in $\Delta\eta$ [70]. Despite the increasing number of confirming experimental measurements, the interpretation of this observation is still debated. It should be noted that these results on the medium response are statistically determined from correlations rather than event-by-event. No direct observation of a cone or a ridge has been made in a single event.

With all of these exciting discoveries there are surprisingly few details that are currently understood about the energy loss mechanism. Debate continues about the dominance of gluon radiation over elastic scattering at momentum scales relevant to RHIC measurements. For example, within a given model, experimental data can tightly constrain the transport coefficient or the color charge density of the medium [8]. However, models still vary greatly between each other, *e.g.* estimates of the transport coefficient differ by a factor of ~ 10 . This is due to the fact that R_{AA} shows little sensitivity to the underlying energy loss mechanism; its observed value can be reproduced by almost all existing models [57].

Understanding energy loss is also experimentally challenging because two-particle correlations are “energy-loss biased”. That is, a high- p_T particle has a higher probability of being detected if it loses relatively little energy due to fluctuations in the number of scatterings (punch-through) or traversing a short path length in the medium by being emitted tangentially. Requiring two high- p_T particles exacerbates this single particle bias by requiring a second high- p_T particle from the recoil jet in the same event. Some combination of these effects probably dominates high- p_T two-particle correlations [57].

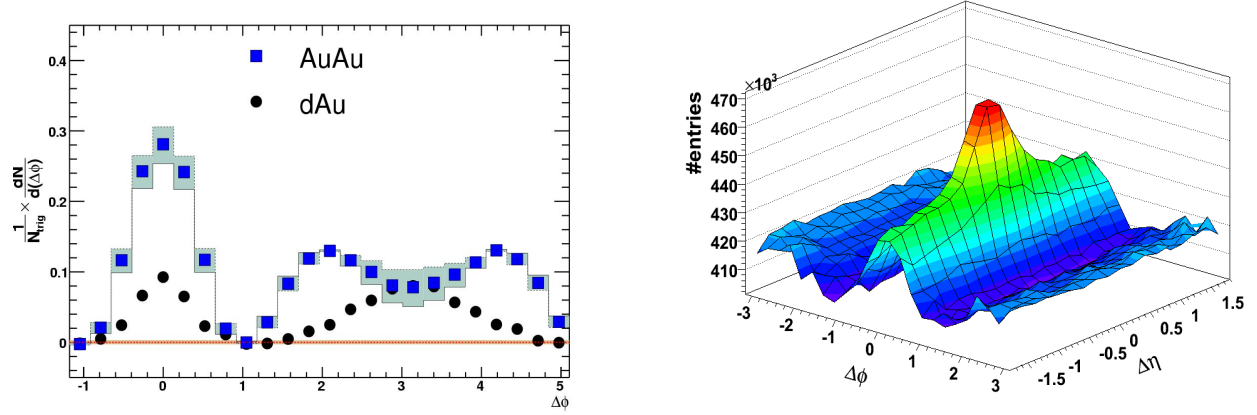


Figure 6.3: (left) Lower- p_T azimuthal correlations in central Au+Au showing a large yield at $\Delta\phi \sim \pi \pm 1.1$ rad [71]. (right) $\Delta\phi \times \Delta\eta$ correlations showing an extended “ridge” in $\Delta\eta$ [69]. The p_T ranges are $3 < p_T < 4$ GeV/c for trigger hadrons and $p_T > 2$ GeV/c for associated hadrons.

These experimental constraints can be overcome at the LHC where copious high- E_T jets will be available that should be visible above the background. This will allow, for the first time, direct jet reconstruction in a heavy ion environment on an event-by-event basis. By fully reconstructing the jet, the entire energy of the primary, hard-scattering process, including the energy lost by the primary parton, should be measurable. This will significantly reduce the energy loss biases. Of course, this assumes that the lost energy remains inside the jet cone, but this is the current expectation from standard energy loss models [13].

Once full jet reconstruction is available, jet tomography will be performed. Energy loss via gluon bremsstrahlung will be tested by studying the effects of energy loss on fragmentation functions, $D(z)$. Here, z is the longitudinal momentum fraction of a jet carried by a fragment. An example of a modification of the $D(z)$ in medium [72] is shown in Figure 6.4. The characteristic pattern for energy loss is the suppression of high- z (high- p_T) fragments whose lost energy is transported to lower- z (lower- p_T) fragments. The ratio of the modified $D(z)$ to the vacuum $D(z)$ is below 1 at high z and above 1 at low z .

Another tool to study gluon bremsstrahlung is by measuring the hard radiation from the interaction of the jet with the medium. This is done via the j_T distribution. Here, j_T is defined as the transverse momentum of a fragment with respect to the jet axis. The high- j_T distribution is dominated by parton splitting in the fragmentation chain and should be enhanced by the additional hard radiation from jet-medium interactions. An example of the possible modification of the j_T distribution [13] is shown in Figure 6.5. The plot shows different j_T distributions (labeled as k_t) for gluons from jet fragmentation and energy loss with different gluon energy cuts and different maximum angles from the original parton. Even with a 5 GeV cut on the gluons, which cuts away much of the underlying event background, additional gluons are measured at large j_T resulting from the hard gluon radiation in the jet.

Collisional energy loss can be studied by looking at the jet R_{AA} . If all of the lost energy was recoverable by jet reconstruction, the jet spectrum should scale with N_{Coll} like the direct photon spectrum (see Figure 6.1). Consequently, any energy lost not recoverable by full jet reconstruction, will result in the softening of the jet spectrum. Collisional energy loss results in energy imparted

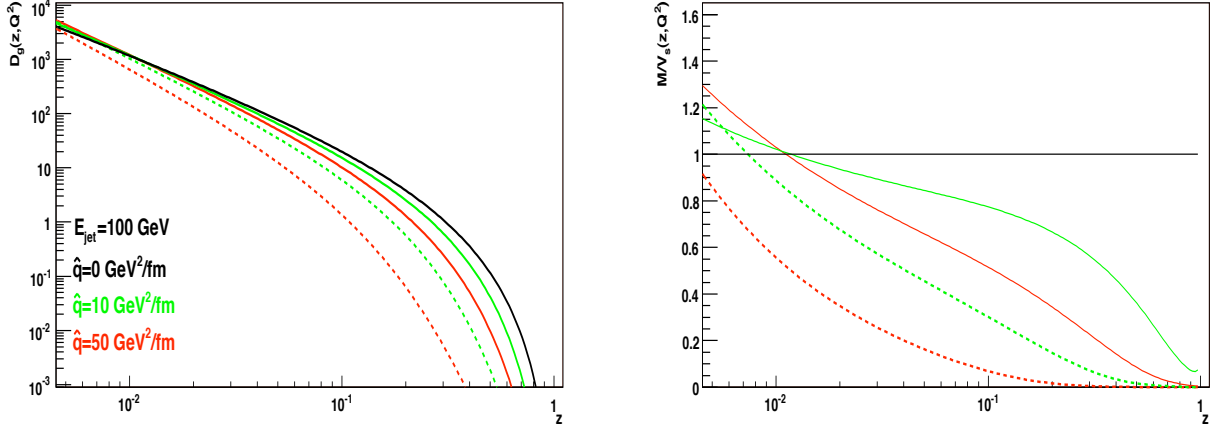


Figure 6.4: (left) Gluon to pion fragmentation functions in vacuum (black), in medium with $\hat{q} = 10\text{GeV}^2/\text{fm}$ (green) and $\hat{q} = 50\text{GeV}^2/\text{fm}$ (red) for 100 GeV jets passing through 2 fm of medium (solid) and 6 fm of medium (dashed). (right) The ratio of the in-medium modified fragmentation functions to the vacuum [72].

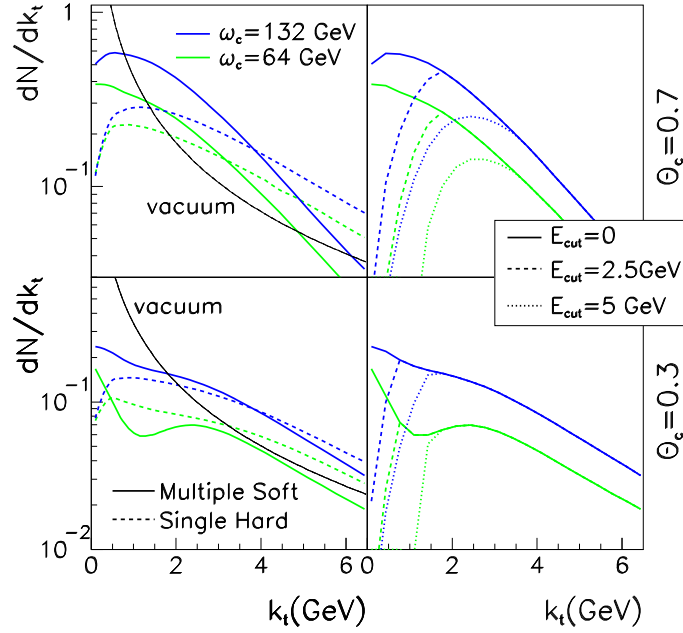


Figure 6.5: Gluon transverse momentum with respect to the jet axis (j_T in the text) distributions for different energy (E_{cut}) and angular cuts (θ_c) of the gluons. The vacuum distribution is shown in the thin solid lines. The different colored lines indicate two different medium transport properties (ω_c). Dashed lines indicate medium response and different energy cuts. Hard, in-medium gluon radiation results in increased yield at large k_t (j_T).

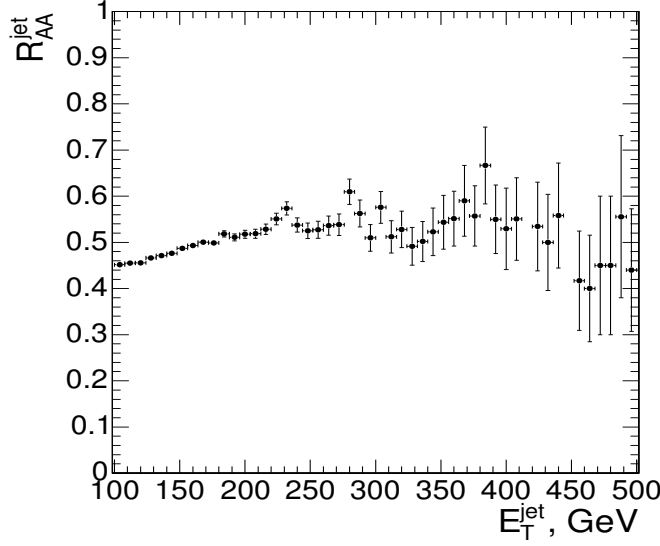


Figure 6.6: Calculated jet (cone size $R = 0.5$) R_{AA} in central Pb+Pb collisions from Ref. [15] including effects from both collisional energy loss and radiative energy loss outside the jet cone.

to the medium and, thus, not radiated within the jet cone. This softening can be measured like the single particle suppression by measuring the jet R_{AA} . An example of such jet $R_{AA} < 1$ from collisional energy loss is shown in Figure 6.6. Clearly with these observables jet reconstruction opens up new avenues of studying energy loss at the LHC.

6.2 ATLAS calorimeter and jet measurements

The ATLAS calorimeter is uniquely suited to perform full jet measurements and, thus, to make important and unique contributions to the understanding of jet energy loss and medium response to jets. The calorimeter (see Fig. is nearly hermetic, covering 2π in azimuth, with the barrel and end-caps covering $|\eta| < 3.2$, and the forward calorimeters (FCAL) covering $3.2 < |\eta| < 5$. An active pre-sampling layer in front of the electromagnetic calorimeter improves the energy resolution for electromagnetic showers that originate in the inner detector. The calorimeter is longitudinally segmented with three electromagnetic and three hadronic measurements over most of the coverage of the calorimeter. The longitudinal segmentation of the calorimeter provides improved separation between electromagnetic and hadronic showers and is helpful in Pb+Pb collisions where the soft hadron background ranges out faster with depth than electromagnetic showers. In particular, because of the 2 T magnetic field, soft particles impact the front of the calorimeter at a shallow angle and deposit a large fraction of their energy into the first layers of the electromagnetic calorimeter. On average 60% of the background energy is deposited within the pre-sampler and first electromagnetic layer with the result that the second and third electromagnetic layers are less sensitive to soft hadron background.

As noted in Section the fine η segmentation of the first electromagnetic layer ($\Delta\eta \approx 0.003$ in the barrel) is particularly valuable for carrying out jet measurements. The typical energy deposit

in one of the cells in the first electromagnetic layer in a central HIJING [73] Pb+Pb event is ≈ 30 MeV while the peak energy deposit for a 1 GeV photon is typically a factor of 10 larger. Thus, electromagnetic showers from neutral hadrons and or prompt photons can be easily distinguished from the Pb+Pb underlying event (see Section).

6.3 Jet reconstruction in Pb+Pb collisions with ATLAS

The goal of the heavy ion jet analysis is to use algorithms developed for p+p measurements so that the calibrations obtained from p+p data can be used for Pb+Pb measurements with only modest adjustments. Currently, two complementary jet reconstruction algorithms are being explored: a seeded cone algorithm [74, 75] and an implementation of the k_T algorithm [76, 77, 78] optimized for fast execution time (Fast- k_T [79]). The cone and k_T algorithms differ significantly in the way they find jets, in their sensitivity to jet shape, and in the way they are adapted to the underlying event in Pb+Pb collisions. The use of multiple jet algorithms with different sensitivity to jet shape provides essential control over systematics in Pb+Pb jet measurements, especially as we do not know *a priori* the nature of the underlying event or the effects of jet quenching on the jet shape.

6.3.1 Seeded cone algorithm

The seeded cone algorithm operates on calorimeter towers. Towers are defined from energy sums of all the calorimeter layers within $\Delta\eta \times \Delta\phi = 0.1 \times 0.1$. The towers within a given radius $R = \sqrt{\Delta\phi^2 + \Delta\eta^2}$ of the seed tower are clustered and iterated on until a convergence of the 4-vector of the jet is reached. For this algorithm, the underlying event background must be subtracted prior to reconstructing the jets. An η -dependent average cell energy, $\langle E_T^{\text{cell}} \rangle(\eta)$ is calculated for each layer of the electromagnetic and hadronic calorimeter. The $\langle E_T^{\text{cell}} \rangle(\eta)$ values are obtained excluding cells from high- E_T towers and the neighboring regions to prevent jets from biasing the background estimates. After the $\langle E_T^{\text{cell}} \rangle(\eta)$ values have been subtracted from all calorimeter cells, the resulting background-subtracted tower energies are input into the seeded cone algorithm to reconstruct jets. In this analysis, a cone of $R = 0.4$ and a seed tower energy threshold of 5 GeV are used. An example of the results of the background subtraction procedure is shown for a single event in Fig. 6.7.

The iterative cone jet algorithm will produce a candidate jet only when the transverse energy inside the cone is a local maximum in (η, ϕ) . However, in the presence of heavy ion background, not all such maxima are true jets. Our studies of the behavior of the ATLAS seeded cone algorithm indicates that it is not particularly sensitive to fluctuations in the number of soft particles in the cone but is sensitive to hard or semi-hard particles in the underlying event, particularly correlated particles arising from mini-jets and charm or bottom hadrons. Figure 6.8 shows an example of such a jet compared to a real jet from PYTHIA. The “raw” candidate jets returned by a standard cone algorithm, therefore, need to be subjected to background discrimination before they can be accepted as true jets. The HIJING generator without quenching produces a large number of mini-jets and heavy quarks, thereby generating an underlying event for which correlated fluctuations are relatively common. Thus, it provides a valuable testing ground for procedures to reject fake jets.

The characteristics of the raw fake jets returned by the cone algorithm were studied using a separate sample of HIJING events generated without quenching but with a cut on the maximum

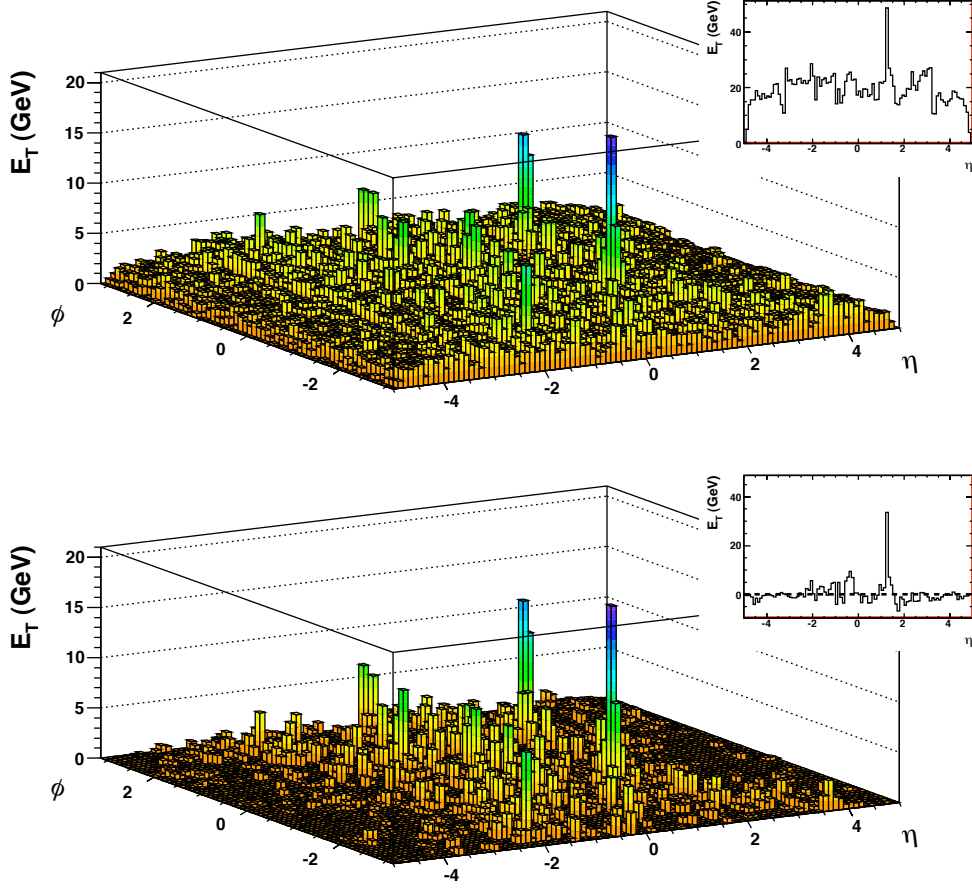


Figure 6.7: (top) Tower energies for a PYTHIA [80] di-jet event embedded into a HIJING event without quenching. (bottom) Tower energies in the same event after layer- and η -dependent subtraction of $\langle E_T^{\text{cell}} \rangle$ to remove the underlying event. The background-subtracted tower energies are then used as input to the seeded cone algorithm. The inset figures show the η -dependence of the energy in the towers integrated over $-0.5 < \phi < -1.5$ rad, which picks out the jet at $\phi \sim -1$ rad. The large background from the underlying event is suppressed by the background subtraction.

p_T , $p_T < 10$ GeV/c, of outgoing partons in hard scattering processes. In this sample of events, all jets reconstructed above 10 GeV/c are in principle fake jets returned by the cone algorithm¹. Several variables sensitive to the energy profile in the jet were evaluated. The most useful variable for rejecting fake jets was found to be j_T^{Sum} , which is defined as

$$j_T^{\text{Sum}} = \sum_{\text{cell}} E_T^{\text{cell}} \sin R_{\text{cell}} \quad , \quad (6.2)$$

where $R_{\text{cell}} \equiv \sqrt{\Delta\phi^2 + \Delta\eta^2}$ is the jet cone angle between the cell and the jet axis. This variable

¹In reality, HIJING also produces jets and/or high- p_T hadrons from hard gluon radiation off a “soft” string. These are removed with cuts on the maximum hadron p_T for the fake jet analysis.

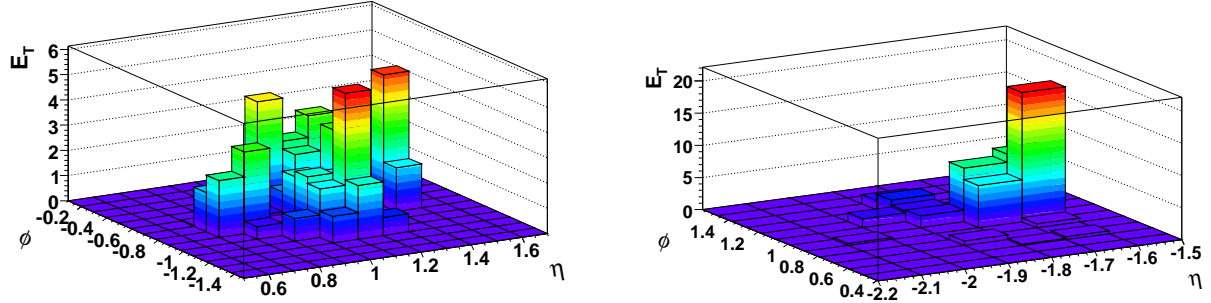


Figure 6.8: Demonstration of difference between false and true candidate jets returned by the iterative cone algorithm. (left) E_T distribution in $\Delta\eta \times \Delta\phi = 0.1 \times 0.1$ towers for a false jet resulting from nearby above-average E_T towers. (right) A similar distribution for a real jet (with an atypically asymmetric fragmentation).

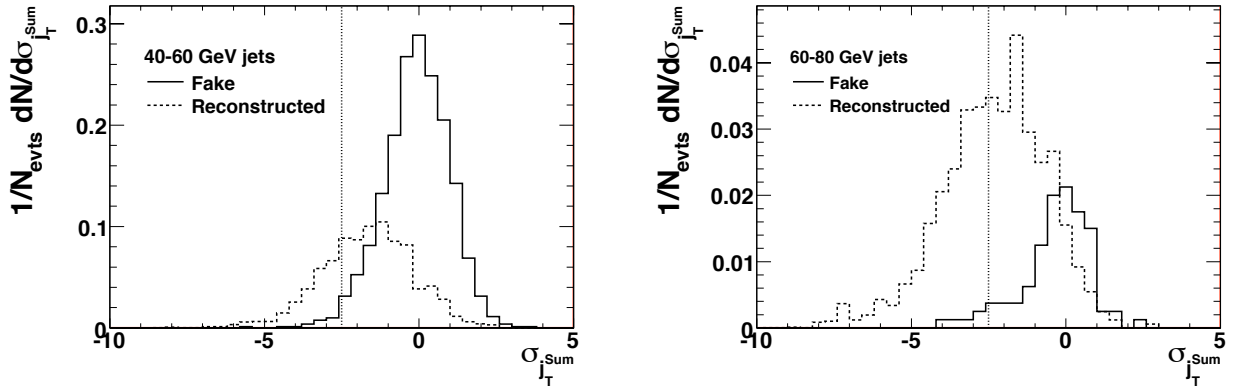


Figure 6.9: Comparison of the E_T -dependent $\sigma_{j_T^{\text{Sum}}}$ cut (see Eq. 6.3) for two different jet energies 40-60 GeV (left) and 60-80 GeV (right). Jets with $\sigma_{j_T^{\text{Sum}}} > -2.5$ are removed.

assigns higher weights to cells with larger energy or cells at large angles from the jet axis. For real jets, j_T^{Sum} depends both on the jet energy and on the angular distribution of fragments in a jet, but in a non-trivial way due to the narrowing of the jet cone with increasing energy. For fake jets we find that j_T^{Sum} is roughly proportional to the E_T of the false jet. The dependence of the separation between real and fake jets on jet E_T is removed by making an E_T -dependent cut:

$$\sigma_{j_T^{\text{Sum}}} = \frac{j_T^{\text{Sum}}(E_T) - \langle j_T^{\text{Sum}} \rangle(E_T)}{\sigma(E_T)}, \quad (6.3)$$

where $\langle j_T^{\text{Sum}} \rangle(E_T)$ and $\sigma(E_T)$ are the E_T -dependent average value and width, respectively, for the *fake* jet j_T^{Sum} distribution. Figure 6.9 shows the distribution of $\sigma_{j_T^{\text{Sum}}}$ for false (solid) jets and real (dashed) jets. The false jet distributions are centered at 0 and have widths of 1 as seen from Eq. 6.3. With increasing cone E_T energy the separation of the real and fake jets increases. A cut of $\sigma_{j_T^{\text{Sum}}} > -2.5$ rejects most of the fake jets, but also produces an E_T -dependent efficiency loss that

is particularly severe at low E_T . Such a cut can be tuned to optimize between the desired purity and efficiency and also on the characteristics of the background. We note that the actual Pb+Pb background is likely to have substantially lower level of correlated fluctuations than produced by HIJING without quenching. The background rejection technique described here can, then, be used with a less restrictive cut on the discriminator variable and with a corresponding improved efficiency at low p_T .

6.3.2 k_T algorithm

The k_T algorithm [76, 77, 78] finds jets by recursively clustering towers until a cut-off criterion is reached. The extent of clustering can be controlled by a parameter, D , which was chosen to be $D = 0.4$ for the studies presented below. A particular advantage of this algorithm is that no fixed geometry (e.g. a cone) is imposed on the reconstructed jet. In the case of the Fast- k_T algorithm [79], the underlying event is handled in a completely different way from the cone algorithm. Following Cacciari and Salam [79], the jet reconstruction is performed directly on heavy ion events without background subtraction. In addition to real jets, the background towers are clustered into soft jets as shown in Fig. 6.10 for a HIJING [73] embedded PYTHIA[80] event. There are two jets from the embedded PYTHIA event which are clearly visible above the heavy ion background. The different shaded regions denote the jet candidates in this event (bottom left panel), most of them are jets primarily composed of background. The bottom right panel shows, for each jet, the ratio of maximum to average tower energy, E_T^{max}/E_T^{avg} , within the jet, plotted as function of the jet η . Clearly, this variable distinguishes between the PYTHIA jets and background jet candidates. It should be noted that this ratio for a jet with a Gaussian distribution in R is $1/\sigma$, where σ is the width of the energy profile in R . Therefore the background jets are much wider than the signal jets, as expected, and have lower values of E_T^{max}/E_T^{avg} . The η dependence of the ratio is parameterized as $r(\eta)$ and shown as the solid line in the lower right panel of Fig. 6.10. The difference between the actual E_T^{max}/E_T^{avg} and the parameterization is calculated for each jet candidate. This results in a difference distribution with a mean (μ) and a root-mean-square (RMS). A cut

$$(E_T^{max}/E_T^{avg} - r(\eta)) < \mu + 2 \times RMS$$

selects background jets. These jets are then used to estimate the underlying event background which is subsequently subtracted from the real jets.

6.4 Jet reconstruction performance

6.4.1 Method of evaluation

The performance of the seeded cone and k_T algorithms was evaluated through an extensive simulation study. In the simulation, a merged event is constructed by embedding a PYTHIA di-jet event into a simulated Pb+Pb HIJING event without quenching and without a hard scattering cut which would remove mini-jets. In heavy-ion collisions, the performance of the jet reconstruction algorithm is very sensitive to fluctuations in the underlying background. Thus mini-jets, heavy quarks, and other correlated sources produce many fake jets at low E_T . The HIJING events likely represent an upper limit of the event multiplicities (in $dN_{ch}/d\eta$) comparing to other models at the

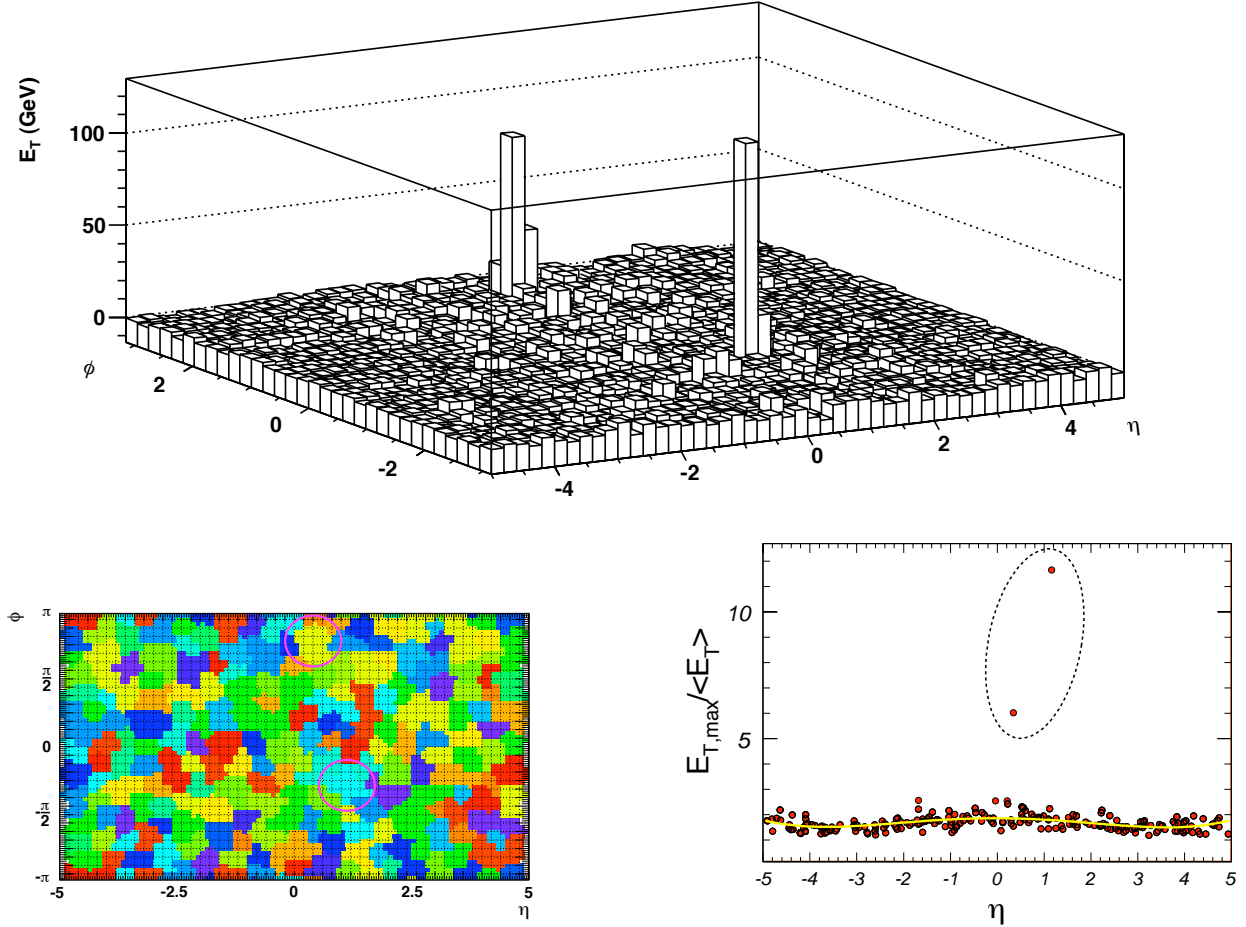


Figure 6.10: (top) Tower energies from a single PYTHIA di-jet event embedded in an event from unquenched HIJING with $dN_{ch}/d\eta = 2700$ at mid-rapidity and run with the Fast- k_T algorithm. (lower left) Each of the different, colored patches represent a jet defined by the algorithm. Every tower, even those with energy predominantly from the underlying event, is incorporated into a jet. (lower right) Distribution of maximum-to-average tower energy in reconstructed jets for this event. The two embedded PYTHIA jets (indicated by the circled points and areas) are distinguishable from the fake, background jets in this variable.

LHC (see Fig.). These simulations therefore represent a “worst case scenario” for the underlying background in Pb+Pb collisions.

Merging jets into background events occurs after each event is passed through a full GEANT simulation of the ATLAS detector. The merged events are then passed through the reconstruction chain and data analysis software. The resulting jets from the merged events are matched to the truth jets, which are defined as the jets found with the same jet algorithm with the PYTHIA final state particles as input. A match is found if the reconstructed jet and truth jets are close enough in angular space ($R = \sqrt{\Delta\phi^2 + \Delta\eta^2} < 0.5$). If multiple reconstructed jets are matched to the same

b (fm)	$dN_{ch}/d\eta _{ \eta <0.5}$
2	2700
4	2200
6	1700
8	1070
10	460

Table 6.1: Fixed impact parameter values used to produce HIJING events and their corresponding mid-rapidity ($|\eta| < 0.5$) charged particle multiplicity.

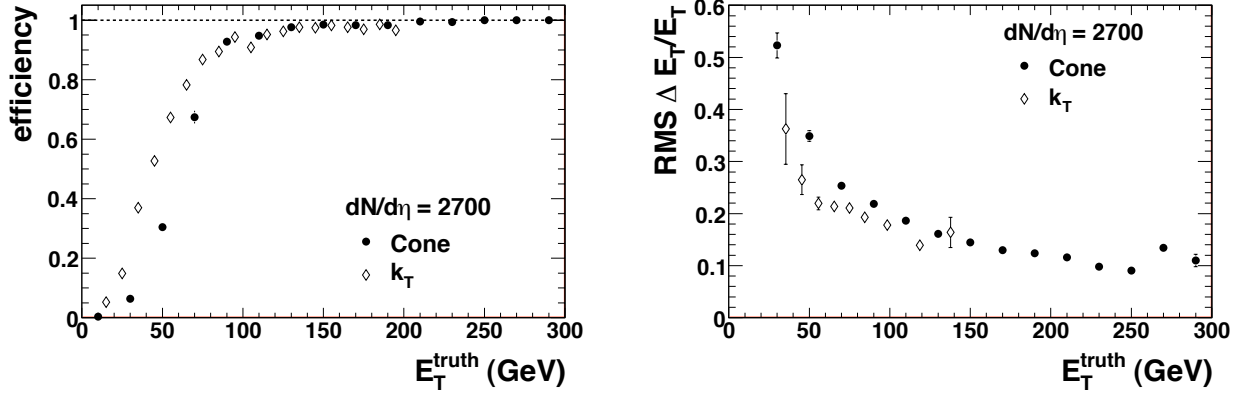


Figure 6.11: Comparison of efficiency (left) and E_T resolution (right) for the cone (closed) and k_T (open) algorithms for reconstructing jets in $dN_{ch}/d\eta = 2700$.

truth jet, the jet with the smallest R is chosen to be the matched jet. In determining efficiencies and fake rates all reconstructed and truth jets are considered and not, for instance, only the highest energy jets in the event. The performance of each jet algorithm is evaluated based on a few key quantities: energy resolution, energy scale, efficiency and fake rate. These quantities are evaluated at the truth jet E_T , η , and ϕ unless otherwise specified.

In order to evaluate the centrality dependence of performance quantities in this and other physics studies, HIJING events were generated at a set of fixed impact parameters. For these impact parameters, the mid-rapidity ($|\eta| < 0.5$) charged particle multiplicity ($dN_{ch}/d\eta$) was evaluated with the results shown in Table 6.1. When discussing the centrality dependence of jet reconstruction performance and other results in later chapters, we will quote $dN_{ch}/d\eta$ since such a quantity is, in principle, less subject to the assumptions of the HIJING model. We note, however, that the correlated semi-hard production in HIJING has a greater impact on jet performance than fluctuations in the soft background so different models for Pb+Pb events producing the same $dN_{ch}/d\eta$ will not necessarily give the same jet performance.

6.4.2 Performance results

Figure 6.11 shows the comparison of the jet performance for cone and k_T jets for the highest multiplicity environment simulated. The efficiency is shown in the left panel. While there are differences at low- E_T , primarily due to how the fake background is handled, the efficiencies converge

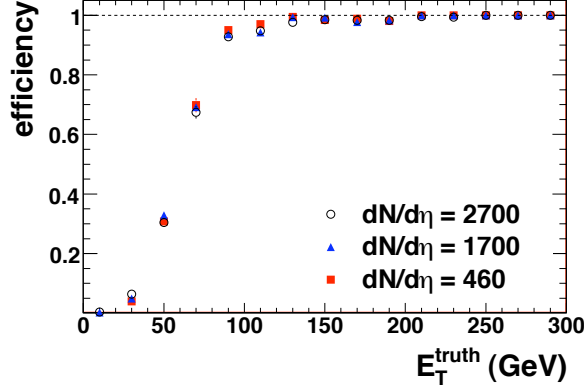


Figure 6.12: Jet reconstruction efficiency for jets reconstructed with the seeded cone and k_T algorithms as a function of input jet E_T and as a function of HIJING Pb+Pb multiplicity.

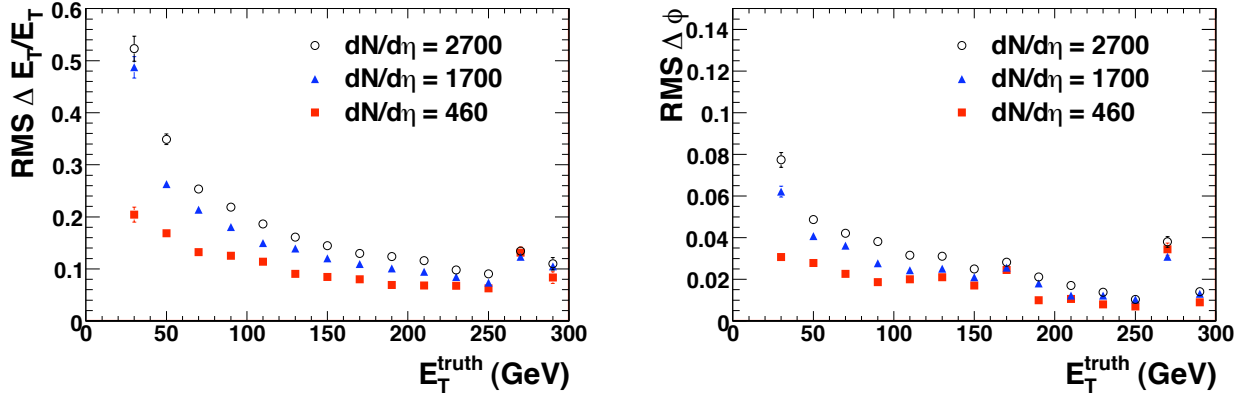


Figure 6.13: (left) Jet energy resolution as function of truth jet E_T for three multiplicity bins for seeded cone jet algorithm. (right) The azimuthal angular resolution of the seeded cone jets as function of truth jet energy.

to better than 95% at $E_T > 120$ GeV. The jet energy resolution is defined as the root-mean-square of the distribution of $\Delta E_T / E_T = (E_T^{truth} - E_T^{reco}) / E_T^{truth}$. A better resolution for the k_T algorithm is observed.

The jet performance results have been studied as a function of background multiplicity. Figure 6.12 shows the jet reconstruction efficiency for seeded cone jets as a function of E_T^{truth} and as a function of HIJING multiplicity. There is little to no dependence of the efficiency on multiplicity. This result is a combination of two effects. First, the shape of the efficiency curve is most influenced by the 5 GeV tower E_T seed cut in cone algorithm. A lower seed cut would result in higher efficiency at lower jet E_T but would generate more background jets. Second, for the results presented in Fig. 6.12 the same background rejection cuts have been applied for all centralities. For actual data analysis, the cuts would depend on centrality becoming less severe for more peripheral collisions. Thus, the results in Fig. 6.12 represent worst-case results for non-central collisions.

Figure 6.13 shows the energy and position (in ϕ) resolution as a function of truth jet E_T for cone jets for several Pb+Pb multiplicity bins. Both energy and position resolution of cone jets improve

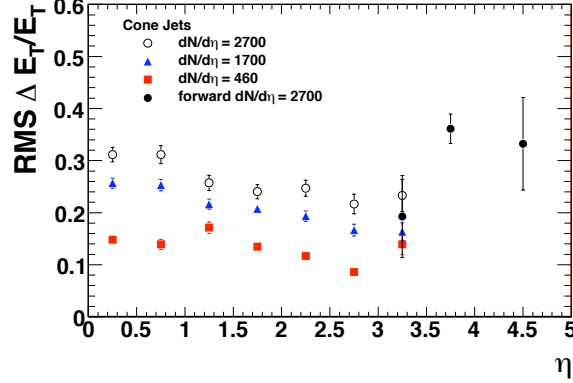


Figure 6.14: Jet energy resolution for $E_T > 50$ GeV seeded cone jets as a function of η for HIJING Pb+Pb events of different centrality, $dN_{ch}/d\eta|_{\eta=0}$.

with increasing jet energy and for lower multiplicity environments. Although not shown, the position resolution in η is comparable to that in ϕ for all multiplicities. We note that many physics models predict that $dN_{ch}/d\eta$ for the most central Pb+Pb events is closer to $dN_{ch}/d\eta = 1700$ than 2700 (see Fig. 5.1), for which case we should expect a significant improvement of the resolution in the real data.

The pseudo-rapidity dependence of the jet performance has also been evaluated. Figure 6.14 shows the jet energy resolution for seeded cone jets with $E_T^{truth} > 50$ GeV and for three different multiplicity bins. The points with $|\eta| < 3.2$ are obtained from jets reconstructed in the barrel and the end-cap calorimeters while the open points with $|\eta| > 3.2$ are from jets reconstructed in the forward calorimeters, an analysis which has only been carried out for the most central Pb+Pb sample. The improvement in energy resolution as η increases in the barrel and end-cap regions is due to the decrease in the underlying HIJING background. In the most forward rapidity region, the energy resolution deteriorates due to larger segmentation of the forward calorimeters. However, due to a lower underlying background, the resolution is comparable to that for mid-rapidity. In summary, over the entire η coverage of the calorimeter, 20-30% jet E_T resolution is obtained in the highest occupancy environment.

Figure 6.14 compares the reconstructed cone jet spectrum with the input and fake jet spectra. Even without correcting for efficiency and energy resolution, the reconstructed spectrum already matches the input spectrum above 80 GeV quite well. The fake jet spectra before and after the rejection cuts are shown by the dashed line and squares, respectively. These rates fall much faster than the input jet spectrum given by PYTHIA. The impact of these performance results on physics results can be seen in Fig. 6.15 which shows the ratio of reconstructed and input jet spectra without correction. Above 80 GeV the required corrections are of order 20%, much smaller than the factor of two jet suppression predicted by Lokhtin (see Fig. 6.6). We note, for completeness, that no adjustment of the jet energy scale after background subtraction has been applied. Distortions of the jet energy scale due to the background subtraction are included in Fig. 6.15. Based on these results, we expect the systematic errors in the measurement of the jet spectrum to be sufficiently controlled that the spectrum can provide direct sensitivity to collisional energy loss and large-angle radiative energy loss.

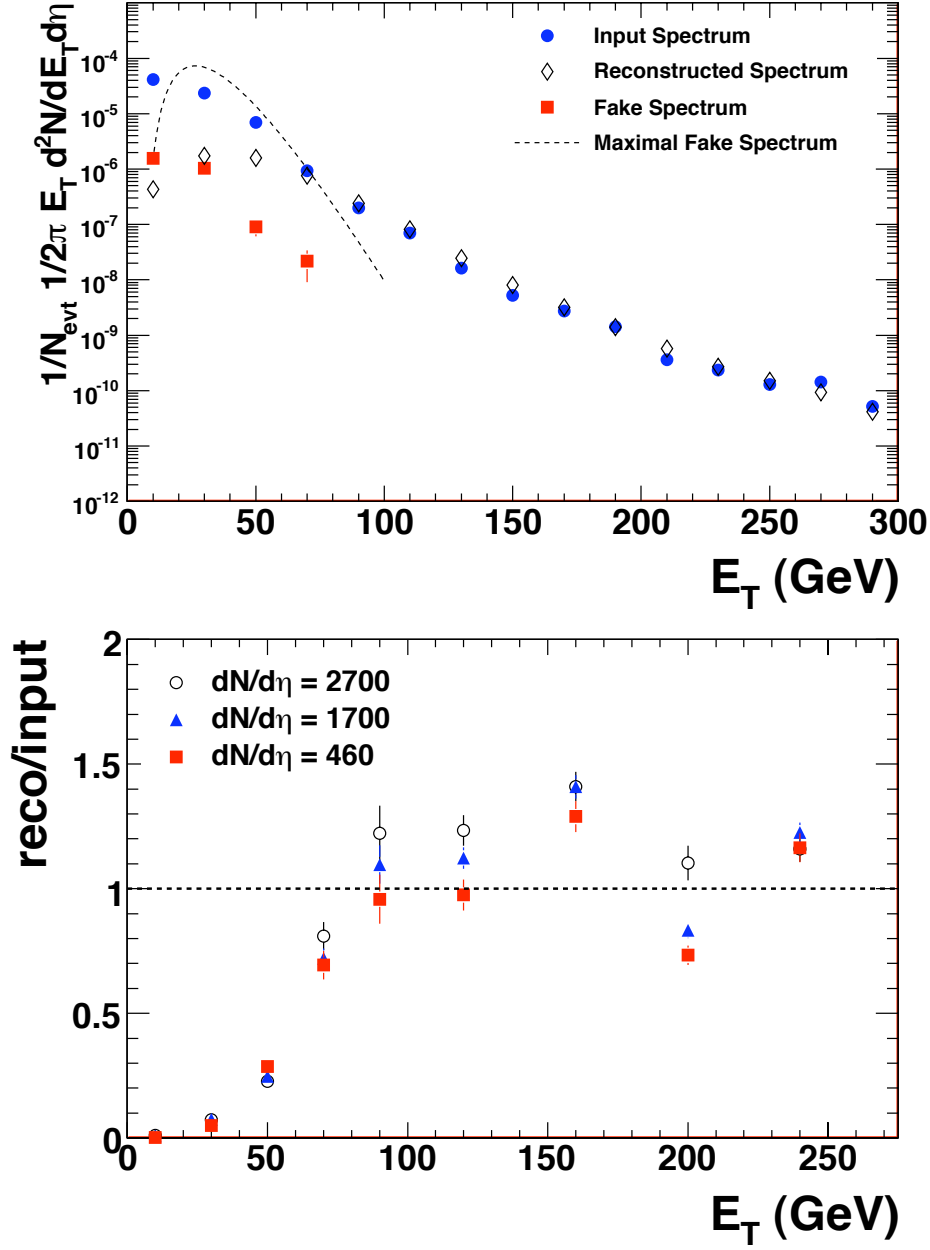


Figure 6.15: (top) Input (filled circles), raw reconstructed (diamonds), and fake (squares) spectra for cone jets in central ($dN_{ch}/d\eta = 2700$) Pb+Pb collisions. The reconstructed spectrum is not corrected for efficiency or energy resolution. The dashed line represents the absolute fake jet rate from pure HIJING events prior to background jet rejection (see text for details). (bottom) Ratio of reconstructed to input jet spectrum for three different Pb+Pb collision centralities without efficiency and resolution corrections to the reconstructed spectra.

$dN_{ch}/d\eta _{\eta=0}$	efficiency	B/(S+B)	$\sigma_{\Delta E_T}/E_T$
2700	70%	3%	25%
1700	70%	1%	21%
460	70%	$\ll 1\%$	15%

Table 6.2: Relevant jet reconstruction quantities for 70 GeV seeded cone jets reconstructed in different $dN_{ch}/d\eta$ backgrounds: efficiency, fake fraction, and jet energy resolution.

A summary of important performance variables, jet reconstruction efficiency, fake rate, and E_T resolution, are listed in Table 6.2 for 70 GeV reconstructed seeded cone jets in three multiplicity bins.

6.5 Jet Fragmentation

Full jet reconstruction provides new variables, sensitive to in-medium energy loss, that are currently not available at RHIC. The first of these is the transverse momentum of fragments with respect to the jet axis, j_T ,

$$\begin{aligned} j_T &= |\hat{p}_{jet} \times \vec{p}_{frag}| \\ &\approx p_{T,frag} \sin R \quad , \end{aligned} \quad (6.4)$$

where \hat{p}_{jet} is the jet direction, \vec{p}_{frag} is the three momentum vector of the fragment, $p_{T,frag}$ is the particle transverse momentum with respect to the beam, and $R = \sqrt{\Delta\phi^2 + \Delta\eta^2}$ is the jet cone variable. The j_T distribution has a soft core governed by non-perturbative physics and a power law tail resulting from hard radiation of the parton shower. Jet in-medium energy loss is expected to modify the distribution of hard fragments associated with the jet and can be detected as a modification of the j_T distribution [13].

Another observable of interest is the modification of the jet fragmentation function. The fragmentation variable, z , is the longitudinal fraction of the jet momentum carried by the fragment,

$$\begin{aligned} z &= \frac{\hat{p}_{jet} \cdot \vec{p}_{frag}}{|\vec{p}_{jet}|} \\ &\approx p_{T,frag}/E_{T,jet} \cos R. \end{aligned} \quad (6.5)$$

The interaction of the jet with the medium is expected to soften the fragmentation function by reducing the number of fragments at large z and increasing the number of fragments at small z (see Ref. [72] for a recent analysis).

The reconstructed fragmentation function, $D(z)$, and the j_T distribution are obtained using charged tracks with $p_T > 2$ GeV/c reconstructed from the silicon detectors (Pixel and SCT) in the ATLAS Inner Detector (see Chapter 3 for more details on tracking performance). The tracks are required to match to hits in the calorimeter taking into account the bending due to the magnetic field. The measured j_T distribution and fragmentation function are shown in Fig. 6.16 for the highest multiplicity Pb+Pb events considered. These distributions have been corrected for an approximately constant tracking reconstruction efficiency of 70% (as shown in Fig.), they are

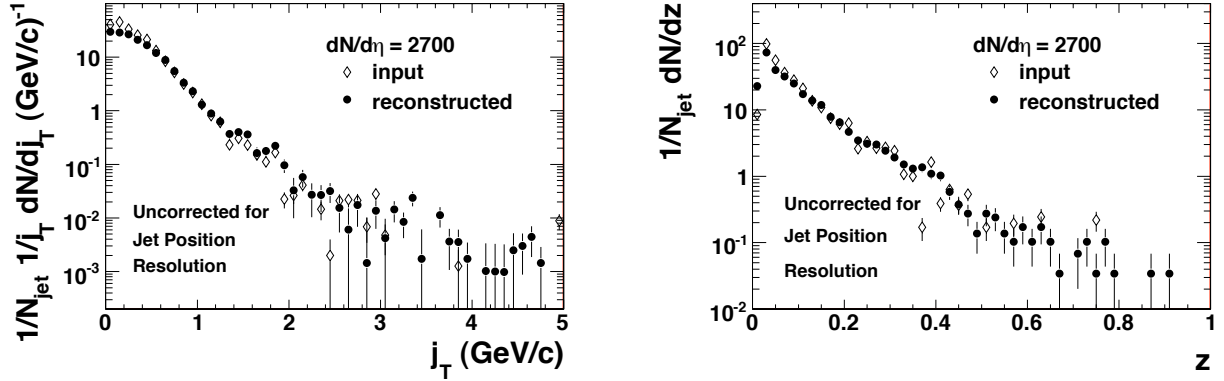


Figure 6.16: (left) Input (open) and reconstructed (closed) j_T distribution (see Eq. 6.4). (right) Input (open) and reconstructed (closed) fragmentation functions (see Eq. 6.5). The reconstructed quantities are uncorrected for position and energy resolution, which accounts for any difference with the input distributions.

not corrected for the position and energy resolution of the reconstructed jets. These distributions are also compared with the distributions for final state truth charged particles within an $R = 0.4$ cone around the truth jet axis. Since no medium modifications are simulated, the truth and reconstructed distributions should be essentially the same, as is indeed observed. Small differences between the truth and reconstructed distributions are entirely attributed to the jet position and energy resolution.

6.6 Di-jet correlations

The large η acceptance of the ATLAS calorimeter system provides nearly complete acceptance for di-jets making possible a variety of correlation measurements. Jets traversing the medium are also expected to multiple scatter as a consequence of energy loss [18]. Therefore, angular correlations between the back-to-back di-jets should be broadened in central Pb+Pb collisions relative to p+p collisions [12]. The left panel of Fig. 6.17 shows the conditional yield of detecting a second, associated jet (B) given a leading jet (A) as a function of their relative azimuth, $|\Delta\phi|$ in central Pb+Pb collisions. The seeded cone jet reconstruction algorithms are used and no efficiency and energy resolution corrections were applied. The distributions show a clear peak at $|\Delta\phi| = \pi$, indicating the back-to-back emission of di-jets, and very little background at other $|\Delta\phi|$. Integrating the distribution gives a 60% probability for detecting a jet with $E_T > 70$ GeV that is associated with a leading jet with $E_T > 100$ GeV. This high coincidence rate is due to the large detector acceptance and accurate measurements for single jets. A more sensitive probe of multiple scattering might be the p_{out} distribution which measures the momentum acoplanarity of the associated jet compared to the leading jet. The variable p_{out} is defined as

$$p_{out} = E_T^B \sin R. \quad (6.6)$$

and its distribution is shown in the right panel of Fig. 6.17.

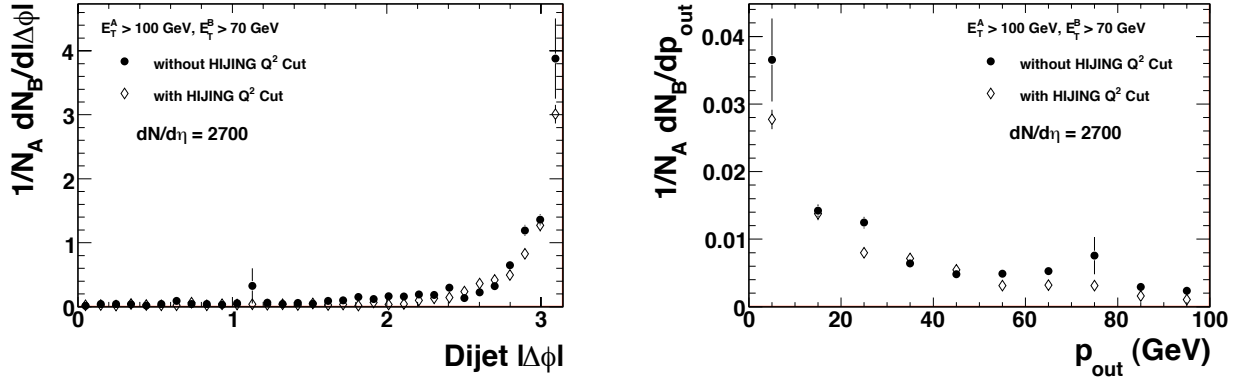


Figure 6.17: Conditional yield for finding an associated jet above 70 GeV (B) given a leading jet above 100 GeV (A), plotted as a function of (left) di-jet $|\Delta\phi|$ and (right) p_{out} (see Eqn. 6.6).

At RHIC, the studies of the medium response to jet energy loss are important tools to understand properties of the produced medium. In principle, such studies can also be explored with ATLAS. However, ATLAS's abilities for measuring medium response are difficult to quantify as there is no consensus on the mechanism of medium response, and thus no model implementations of this effect exist that could be used to generate LHC events. Still, if a ridge exists and is associated with a high- E_T jet and extends to ± 4 units in $\Delta\eta$, the ATLAS calorimeter, covering $|\eta| < 5$, will certainly encompass the entire ridge. Furthermore, a possible Mach cone and ridge associated with di-jets can be studied on an event-by-event basis as opposed to statistically averaging over many events as has been done at RHIC. These are some of the physics capabilities that will be explored in the near future.

6.7 Heavy quark jet reconstruction

To understand heavy quark energy loss, it will be important to identify bottom and charm jets. Fortunately, the excellent jet reconstruction capability of the ATLAS detector and excellent capabilities for tagging heavy quark mesons and associated semi-leptonic decay muons make the direct study of the heavy-quark energy loss feasible. Once the high energy jets are reconstructed, two tagging methods can be applied to identify the flavor of the reconstructed jets: 1) tagging charm and bottom mesons directly via their displaced decay vertices and associating these heavy mesons to reconstructed jets; 2) associating semi-leptonic decay muons directly to reconstructed jets. A first attempt of the latter approach is described in this section.

To leading order in QCD, most of the muon-tagged jets come from hard-scattering processes that lead to di-jet events. The reconstructed jet and muon could either belong to the same truth jet, or they belong to different jets of the di-jet. Due to the weak decay of light hadrons in flight, a portion of the muons may not be associated with heavy quark jets. In addition, only a fraction of the heavy quark jets contribute to high p_T muons via the semi-leptonic decay of heavy quark mesons. Based on these considerations, the performance of muon tagging for heavy quark jets has been quantified by the two most important parameters. The first parameter is the purity of heavy quark jets in the tagged jet sample, and the second parameter is the tagging efficiency for jets

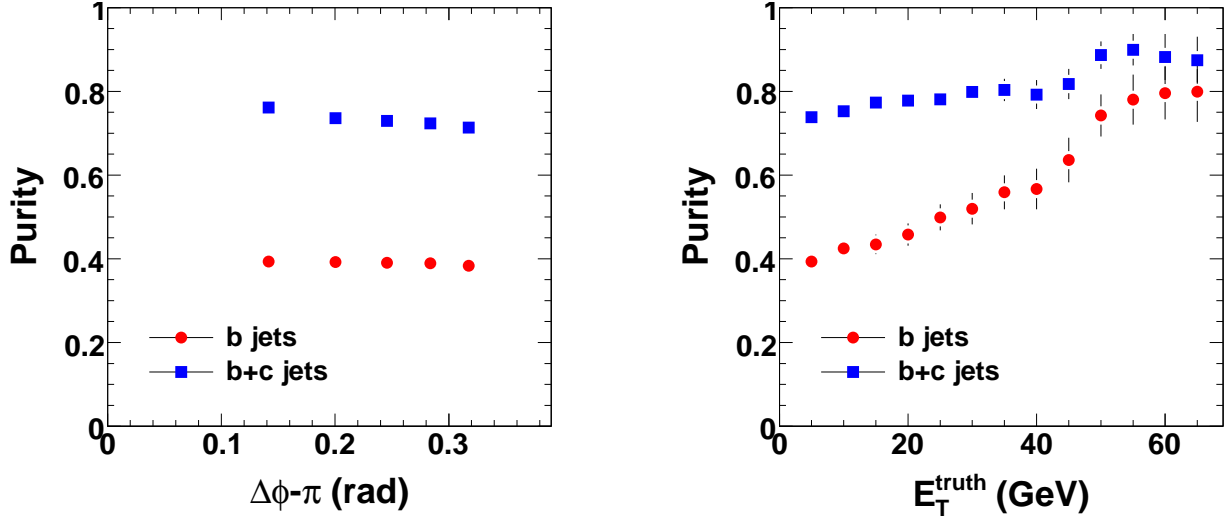


Figure 6.18: Bottom jet (red circles) and heavy flavor (blue squares) tagging purity as a function of azimuthal angle difference between the tagged jet and muon at the away-side ($\Delta\phi \sim \pi$) requiring a muon with $p_T > 5$ GeV (left) and as a function of truth muon E_T (right).

that are known to come from heavy quarks.

To estimate the purity of heavy quark jets in the tagged jet sample, PYTHIA minimum bias events were generated with the requirement that each event contain at least one muon with $p_T > 5$ GeV/c and one jet with $E_T > 35$ GeV. The resulting events were then embedded into central HIJING Pb+Pb events ($dN_{ch}/d\eta = 2700$ at mid-rapidity) generated as described in Section 6.4.1. The jets were reconstructed with the seeded cone jet algorithm as described in the Section 6.3.1. Single muon candidates were reconstructed using the standard tracking and muon identification software in ATLAS [81]. Details of the muon reconstruction are given in Chapter 8.

The purity of heavy quark jets in the tagged jet sample is defined as the ratio between the number of jets of interest, *i.e.* those from heavy quarks, and the total number of jets. To identify the heavy quark jets, the jets reconstructed from the merged event are first matched to the truth jets, which are obtained by applying the seeded cone algorithm to the final state particles in the input PYTHIA event. The matching criteria requires the three-dimensional opening angle between the reconstructed jet and truth jet, θ , to satisfy $\theta < 0.2$ rad. Input (truth) jets are tagged as bottom jets by tracing the PYTHIA ancestry information back to the original string. If it is a bottom string and the truth jet in question has more than 50% of the bottom quark energy, the truth jet is considered to be a bottom jet. Otherwise, the truth jet, and hence the matched reconstructed jet, is either a charm jet or light quark jet.

The purities of the muon-tagged jets are shown in the left panel of Fig. 6.18 as a function of the azimuthal angle difference between the muon and tagged jet. The red circles show the bottom-tagged purity; about 40% of the tagged jets come from bottom quarks. The blue squares show the heavy flavor-tagged purity is about 70%. This suggests 30% of the tagged jets come from charm quarks and remaining 30% of the tagged jets come from light quarks and gluons. To summarize, the jets tagged by muon $p_T > 5$ GeV contains approximately equal number of bottom, charm and light quark/gluon jets.

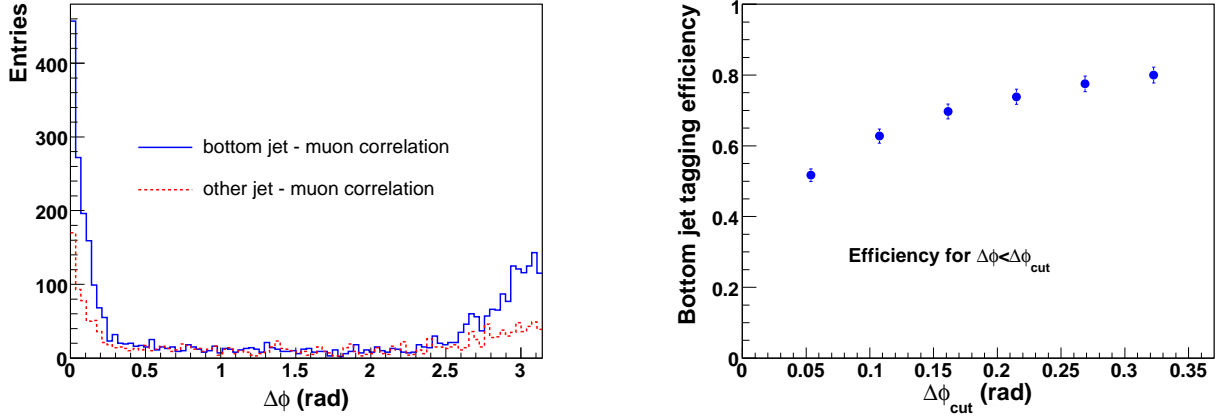


Figure 6.19: (left) Azimuthal correlation between the reconstructed jets and the muons. The solid line and dashed line are for tagged bottom jets and other jets, respectively (right) Jet tagging efficiency as a function of angular cuts ($\Delta\phi < \Delta\phi_{\text{cut}}$).

The purity of heavy quark jets in the tagged jet sample also depends strongly on the trigger muon p_T . This is shown on the right panel of Fig. 6.18. The red circles are bottom-tagged purity and the blue squares show the heavy flavor-tagged purity. For muons at $p_T \gtrsim 60$ GeV/c, approximately 80% of all tagged jets are bottom-jets.

Further improvement is possible if we consider the correlation between muon p_T and jet E_T . Since heavy quark jets have much harder fragmentation functions, *i.e.* the leading heavy meson contributing to the muon carries most of the energy of the jets, the muon p_T and jet p_T should be much closer to each other than for muons from light hadron decays. Thus a high E_T jet correlated with a low p_T muon mostly likely indicates a gluon jet or light quark jet.

The minimum bias PYTHIA events used for the purity study contain a limited number of bottom jets. For an accurate estimation of the tagging efficiency for bottom jets at ATLAS, a separate set of PYTHIA events containing bottom jets was generated, requiring at least one muon with $p_T > 5$ GeV/c, and at least one jet with $E_T > 35$ GeV. These events were embedded into central ($dN_{\text{ch}}/d\eta = 2700$) HIJING Pb+Pb events, and analyzed using the same procedure applied to minimum-bias PYTHIA events. The same procedures for matching the reconstructed jets with truth bottom jets are carried out. Figure 6.19 shows the azimuthal correlation between reconstructed jets ($E_T > 35$ GeV) and muons ($p_T > 5$ GeV/c) for the bottom (blue) and non-bottom (red) jet samples. The muons either come directly from the tagged bottom jet themselves (peak around $\Delta\phi \sim 0$, or they corresponds to muons from a bottom jet recoiling from another bottom jet (peak around $\Delta\phi \sim \pi$). For the non-bottom jet sample, fewer jets are measured, however a correlation with muons is still observed.

The narrow azimuthal correlation between the tagged jets and the muon can be used to improve the purity of the bottom jets by making a matching cut in $\Delta\phi$. The tagging efficiency is defined as the probability for a bottom jet to be within the matching cut. The efficiency for tagging the bottom jet back-to-back to the muon is shown in Fig. 6.19. A cut of 0.16 rad gives a 70% tagging efficiency while relaxing the cut to 0.32 rad gives an efficiency of 80%.

Using high- p_T muons to tag heavy flavor jets will be an important tool in studying the heavy flavor energy loss. A clear correlation in muon-jet $\Delta\phi$ is observed from heavy flavor jets. By

cutting on this muon-jet $\Delta\phi$ and the muon p_T it is possible to tune the purity of the heavy flavor sample and the tagging efficiency.

6.8 Summary

- Utilizing the large acceptance, finely-segmented ATLAS calorimeter, jets in a heavy ion environment can be measured with high efficiency and excellent position/energy resolution over a broad range in energy ($E_T > 40$ GeV), pseudo-rapidity (± 5) and multiplicities (at least up to $dN_{ch}/d\eta = 2700$). These unprecedented reconstruction capabilities for full jets will significantly reduce the energy-loss biases intrinsic in leading hadron and di-hadron correlation analyses at RHIC.
- The full jet and di-jet measurements possible with the ATLAS detector will provide direct constraints on the mechanisms for energy loss and jet-medium interactions. In particular, the jet fragmentation (via $D(z)$) and the jet shape (via the j_T distribution and di-jet $\Delta\phi$ and p_{out}) can be reliably quantified. These measurements are sensitive to jet energy loss and medium response.
- Combining the jet reconstruction with the muon identification capability of the ATLAS detector allows the study of heavy quark energy loss, which will be of particular use to quantify the role of radiative and collisional energy loss.
- Full jet reconstruction combined with the direct photon capability of the ATLAS calorimeter (described in detail in the next chapter) provides a means to probe the properties of the medium using γ -jet correlations.
- All of the measurables described here will be studied as a function of global variables, such as centrality and the angle with respect to the reaction plane.
- In tandem, these techniques will allow ATLAS to undertake a comprehensive program of tomographic studies of the energy loss and the properties of the medium.

Chapter 7

Jet Quenching

This chapter reviews some details of the jet quenching, suitable variables etc. Illustrative analysis of simulated nonquenched/quenched jets is also exhibited.

This chapter may exist separately or be embedded into the jet chapter...

7.1 Recent predictions of jet quenching

Let us review some recent papers on jet quenching [?, ?, ?]... There are rather old predictions of a large energy loss of the fast partons in dense medium, so called jet quenching. Experimental evidence at RHIC showed clearly this kind of suppression (of fast hadrons on the "away side" from the most energetic hadron acting as a trigger) and also raised a serious question what happens to the absorbed energy by seeing the "Mach cone" structure.

Corresponding objects to study at LHC heavy-ion collisions will be jets and their detailed structure. It means that we will be interested not only at the fate of the leading parton, but also at the evolution of the whole partonic shower finally fragmenting to a jet. There are two basic processes which tear off the parton energy in the medium – collisions with partons of the medium and the medium induced gluon radiation. Different models estimate and treat differently these processes; for practical purposes the most valuable tool is a Monte Carlo programme which can be embedded into an experiment simulation framework and be used to tune the methods of analysis.

This aim is currently fulfilled by the PYQUEN add-on to Pythia, [?]. This model includes both collisional and radiative energy losses (in BDMS manner), angular distribution of the gluon radiation is parametrized by a simple gaussian. This add-on can be used to modify Pythia jets within any simulation framework. We will present later some results of full simulation of the PYQUEN-modified jets in the ATLAS detector.

A recent results on jet shapes and cross sections at LHC p+p and Pb+Pb collisions with medium induced gluon radiation (in GLV formalism) are presented in [?]. The calculated jet shapes describe fairly well the jet data from the Tevatron; although authors don't provide yet the tool to be embedded in our simulation, they provide some quite interesting hints:

Not surprisingly they predict a significant suppression of jets, clear hint is that the most interesting region sits at ET below 100 GeV, although the suppression takes place also above 100 GeV (Fig. 7 from [?]). More surprising is the prediction that the quenched jets will be not too much

broader than vacuum ones (Table 2. and Fig. 11 from [?]).

The last mentioned expectation concides with conclusions of [?, ?]) who built a Monte Carlo model for a parton shower evolution both in vacuum and in the medium – JEWEL. Vacuum jets have been tested on LEP (ALEPH) data. Medium effects are collisional with some mimicking of radiative losses. Authors study the role of recoil partons looking also at their effect on medium. However without the possibility to embedd the JEWEL to our simulations it is hard to analyze in detail the visibility of JEWEL quenching in different variables.

...

7.2 Jet description

RAA, shapes, JT, fragmentation function, $dN/d\zeta$...

7.3 Illustrative quenching

Chapter 8

Quarkonia

Chapter 9

Z

This chapter describes the physics need for Z^0 measurements in $Pb + Pb$ collisions with ATLAS, and ATLAS capabilities for this measurement.

9.1 Physics motivation

Z^0 is a useful probe for understanding properties of hot and dense nuclear matter created in high energy heavy ion collisions.

Z^0 are transparent to strong interaction and rather straightforward to observe in $Pb + Pb$ collisions via di-muon decay mode.

dN/dy of Z^0 is considered a precision test of the PDFs.

In addition, Z^0 -jet correlations can be a useful complimentary measurement for jet-jet and photon-jet studies.

9.2 Introduction

In order to study the effects of high multiplicity environment typical of high energy heavy ion collisions on Z^0 measurement, we generated single Z^0 's with flat distribution in pseudorapidity (from -5 to 10) and transverse momentum (from 0 to 25 GeV). These Z^0 were merged to central (impact parameter $b = 2fm$) Hijing $Pb + Pb$ events. and reconstructed. Same Z^0 's were merged to minimum bias $p + p$ PYTHIA events and also reconstructed. The results of these two simulations were then compared in order to determine how ATLAS detector performance is affected by high multiplicity of $Pb + Pb$ collisions.

All simulations were done with Athena version 12.0.6.

9.3 Z^0 mass resolution.

Di-muon invariant mass distributions in $p + p$ and $Pb + Pb$ events with embedded Z^0 's are shown in Fig.9.1.

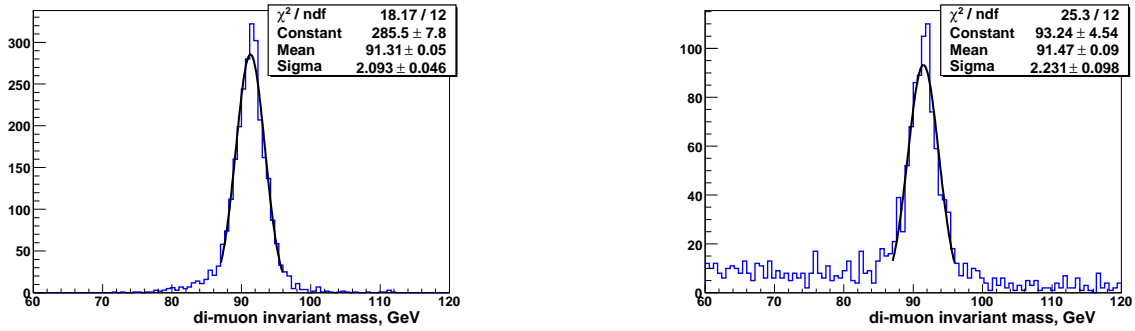


Figure 9.1: (left) Z^0 mass resolution in $p + p$ collisions. (right) Z^0 mass resolution in central $Pb + Pb$ collisions.

9.4 Acceptance times efficiency.

Z^0 acceptance times reconstruction efficiency is shown in Fig.9.2.

Reconstruction efficiency in central $Pb + Pb$ collisions relative to reconstruction efficiency in $p + p$ collisions is $\sim 90\%$ and is shown in Fig.9.3.

9.5 Expected rates and yields

Z^0 production cross section at 5.5TeV is 0.65nb [hep-ph/9907231]. Assuming luminosity 0.5nb^{-1} , ratio of $Pb + Pb$ to $p + p$ cross-sections ~ 100 , Number of binary collisions in minimum bias $Pb + Pb$ events ~ 400 , we get ~ 13000 Z^0 produced in one year of running.

Integrated acceptance times efficiency calculated using pseudorapidity weight shown in Fig.9.4 is 31%. This distribution is, however, different from one predicted in [Anastasiou et al, hep-ph/0312266], see Fig.9.4, left plot. If the later distribution is used, integrated acceptance times efficiency could be almost a factor of 2 larger.

9.6 Summary

This chapter has presented the ATLAS performance for Z^0 measurement in $Pb + Pb$ collisions.

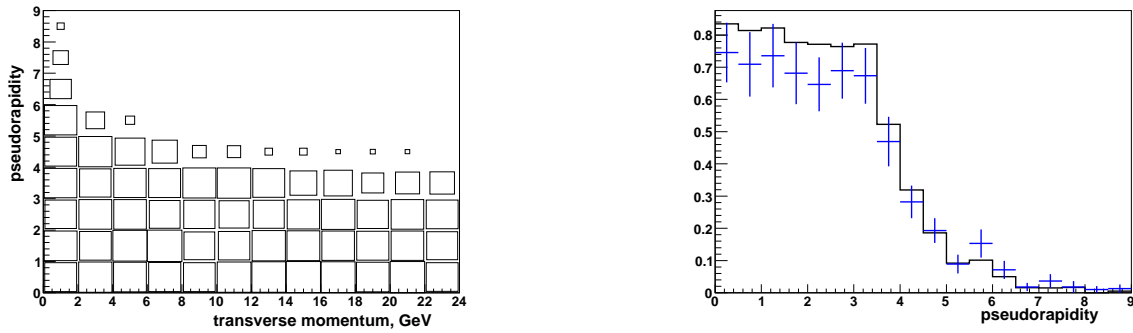


Figure 9.2: (left) Z^0 acceptance times reconstruction efficiency as a function of pseudorapidity and transverse momentum. (right) Z^0 acceptance times reconstruction efficiency in $p + p$ collisions (black histogram) and in central $Pb + Pb$ collisions (blue data points) as a function of pseudorapidity.

- Relative Z^0 reconstruction efficiency is 90% in $Pb + Pb$ collisions compared to $p + p$ collisions.
- Z^0 mass resolution is only weakly affected by high multiplicity environment in $Pb + Pb$ collisions compared to $p + p$ collisions.
- Integrated acceptance times efficiency in $Pb + Pb$ collisions is 31% (???)

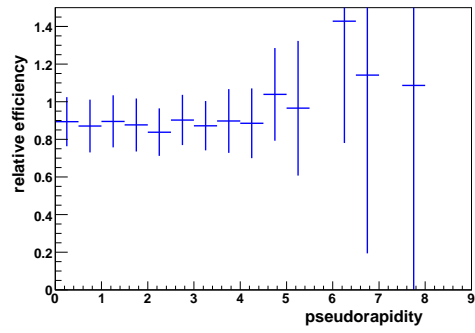


Figure 9.3: (left) Ratio of Z^0 reconstruction efficiency in central $Pb + Pb$ collisions to reconstruction efficiency in $p + p$ collisions as a function of pseudorapidity.

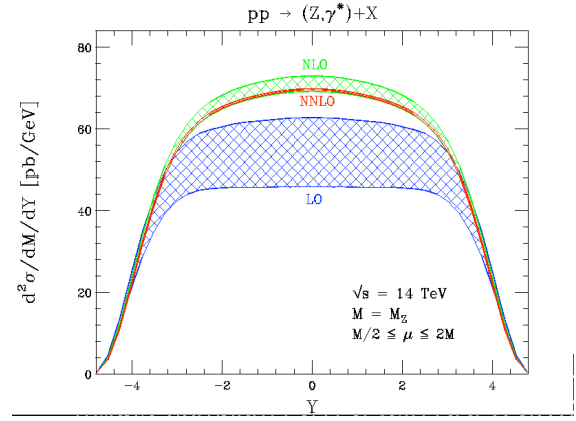
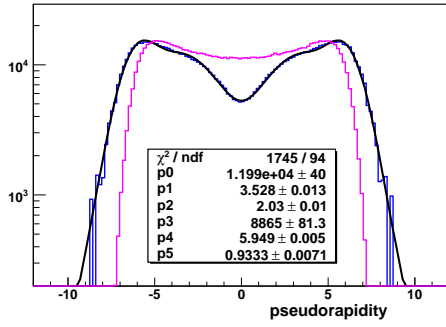


Figure 9.4: (left) Pseudorapidity (black curve) and rapidity (magenta histogram) distributions of Z^0 predicted by pythia for $p + p$ collisions at 5.5 TeV. (right) Rapidity distribution of Z^0 predicted by hep-ph/0312266.

Chapter 10

Direct Photons & Photon-Jet Correlations

This chapter describes the physics need for direct photon and γ -jet measurements with ATLAS, the techniques available in ATLAS for photon detection, and its capabilities for photon physics and γ -jet correlations, both with and without isolation. The ability to efficiently separate photons and neutral hadrons without an isolation cut over a broad acceptance is a unique strength of ATLAS. In addition to providing an optimal window on jet energy loss, this particular aspect of the analysis provides the unique capability to measure non-isolated photons from fragmentation or from the medium.

10.1 Physics motivation

Direct photons are a useful tool, complementary to jet and di-jets, for “tomographic” studies of the microscopic properties of the sQGP. They can be studied either inclusively, or in coincidence with jets (known as “ γ -jet” events). γ -jet events are a particularly useful probe because the medium is transparent to photons. Therefore the γ ’s can be used to measure the original energy and direction of the away-side jets, which should be strongly modified by the medium. They not only provide a model independent way for calibrating the jet reconstruction algorithms (e.g. jet energy scale and resolution), but also help to extend the jet reconstruction to lower E_T where the jet reconstruction efficiency degrades (as shown in Fig. 6.12). This measurement should be able to eliminate the trigger bias intrinsic to the jet-jet coincidence measurements where there is no absolute calibration of jet energy (since both jets being modified by the medium). Thus, the study of γ -jet events provides direct access to the average behavior as well as fluctuations of the energy loss process.

“Direct” photons refer to those photons that are produced during the initial creation and space-time evolution of the fireball, which should be distinguished from “decay” photons from the electromagnetic decays of hadrons. To leading order in pQCD, most direct photons come from γ -jet events generated by the initial hard-scattering processes such as QCD Compton scattering ($qg \rightarrow \gamma q$) and annihilation ($q\bar{q} \rightarrow \gamma g$) processes, and these photons are called “prompt” photons. The main difficulty facing the γ -jet analysis is the relatively small production rate. The cross-section of γ -jet events, compared to jet-jet events, is typically down by a factor of 100–1000 for E_T below 200 GeV at LHC energies. The photons from various decay modes, such as $\pi^0, \eta \rightarrow \gamma\gamma$, create a large background to the direct photon sample. Figure 10.1 shows the direct γ to $(\pi^0 + \eta)$ ratio as function of transverse energy estimated from a next-to-leading order (NLO) calculation

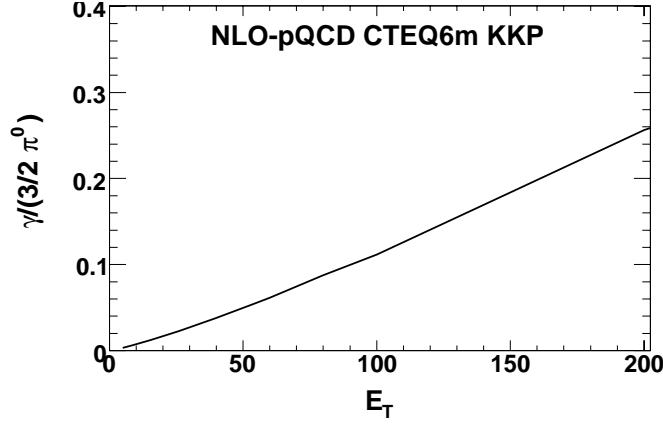


Figure 10.1: Next to leading order pQCD calculation of the direct γ to neutral hadron ratio as function of transverse energy (using CTEQ6m parton distribution function and KKP fragmentation function). The η yield is estimated to be 50% of that for π^0 .

[82], which is around 0.1 for E_T of 100 GeV.

The main challenge for the γ -jet analysis is to derive an algorithm which can effectively reject the decay photons while maintaining a reasonable fraction of direct photons. In this section, the performance of ATLAS detectors for single γ and for γ -jet measurements is evaluated. Two methods are described to reject decay photons. In the first, a shower shape cut based on the highly segmented first layer of the calorimeters provides a factor of 3–5 rejection. An additional factor of 10 rejection can then be achieved by a set of isolation criteria. The largest rejection power is then obtained by combining the shower shape and isolation cuts, which are largely orthogonal to each other. Future prospects and comparisons to ALICE and CMS are discussed in the end.

10.2 Photon identification

The design of the ATLAS electromagnetic calorimeter is optimal for direct photon identification. The first layer of the electromagnetic calorimeter, which covers the full azimuth and $|\eta| < 2.4$, has very fine segmentation along the η direction (ranging from 0.003–0.006 units). This layer provides detailed information on the shower shape, which allows a direct separation of photons, π^0 , and η on a particle-by-particle level. Deposited energy distributions for a typical single γ , single π^0 , and single η meson are shown in the upper panels of Fig. 10.2. Characteristically different shower profiles are seen. The energy of a single photon is concentrated across a few (typically 3) strips, with a single maximum in the center, while the showers for $\pi^0 \rightarrow \gamma\gamma$ and $\eta \rightarrow \gamma\gamma$ are distributed across more strips, often with two or more peaks. The broad shower profile for π^0 and η reflects the overlap of showers for two or more decay photons, which are typically separated only by a few strips. The strip size of 0.003 units roughly corresponds to the minimum opening angle between two decay photons for a 90 GeV π^0 . The opening angle for an η meson with the same energy is about four times bigger. Even when the two peaks are not resolved, the multi-photon showers are measurably broader on a statistical basis. Thus the strip layer allows the rejection of π^0 and η decay photons over a very wide energy range.

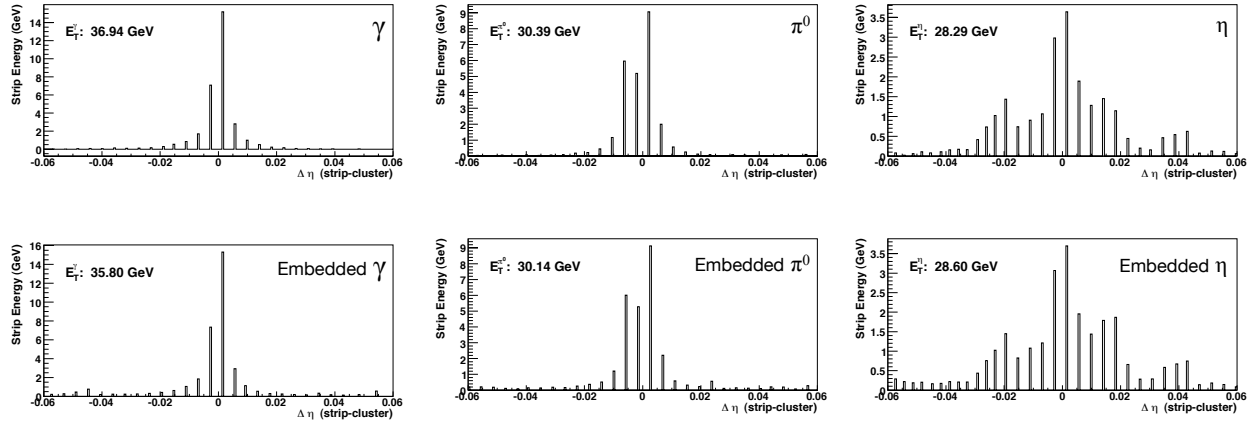


Figure 10.2: The energy deposition in the strip layers around the direction of (upper left) a single photon, (upper middle) a single π^0 and (upper right) a single η as well as for (lower panels) the identical particles embedded in one central ($b = 2$ fm) Pb+Pb event. The energy values are the reconstructed energies.

In Pb+Pb collisions, the shower profiles at the strip layer can be distorted by the high occupancy environment. To study such occupancy effects, single photons, π^0 's and η 's have been embedded in Pb+Pb events generated with HIJING. The official ATLAS detector simulation, digitization and data analysis procedures have been used to simulate and analyze the merged events and to reconstruct the embedded photons and mesons. The lower panels of Fig. 10.2 show the strip layer energy distributions surrounding the direction of single particles embedded in central Pb+Pb events. The γ , π^0 and η in these panels are the same ones used in the upper panels. Despite the huge number of low-energy particles produced in Pb+Pb events, the underlying event only introduces, typically, around a hundred MeV background for each strip. In comparison, a single photon typically deposits 40-50% of its total energy in the strip layer. Since the energy deposited in each strip by a high energy single γ , π^0 and η is typically several GeV, the shower shape for the embedded particle is almost unchanged by the background. One expects the rejection to work down to very low energy (about 10 GeV), and the performance for the background rejection and identification efficiency should not depend strongly on the event centrality.

To distinguish direct photons from neutral hadrons, a set of cuts has been developed based on the shower shape in the strip layer. These cuts reject those showers that are anomalously wide or exhibit a double peak around the maximum. In total, six variables are used to define the cuts, the most important being:

- F1: the fraction of energy outside the shower core of six stripes, i.e. $(E(\pm 7) - E(\pm 3))/E(\pm 7)$, where $E(\pm n)$ is the energy deposited in $\pm n$ strips around the strip with the highest energy;
- E2: The difference between the energy associated with second peak and the minimum energy found in between the two peaks.

The cuts on these variables have been tuned as function of photon energy and pseudo-rapidity. In general, better rejection can be achieved using a tighter cut, but at the expense of reduced efficiencies. The performance has been quantified via photon efficiency (ϵ_γ) and relative rejection

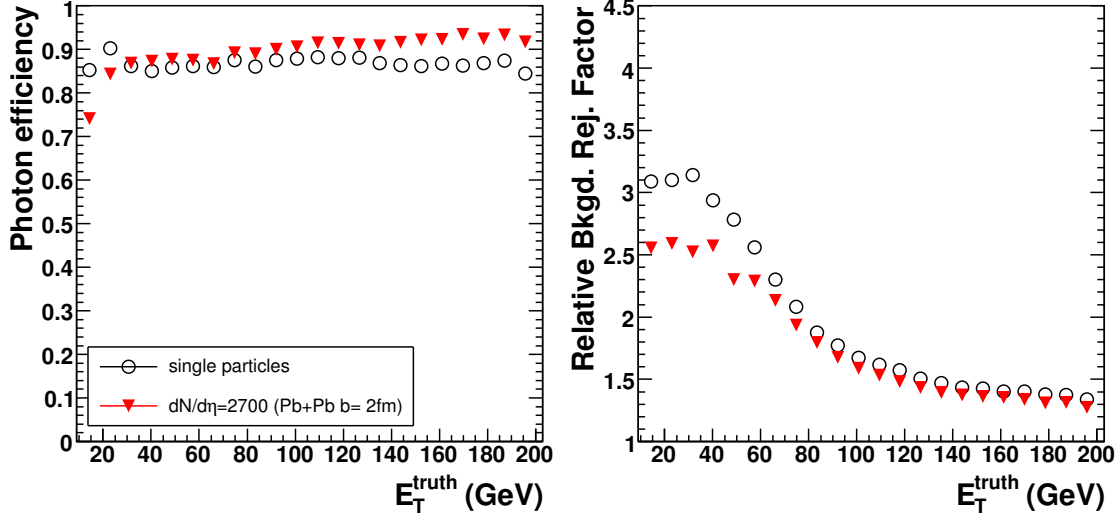


Figure 10.3: (left) Photon identification efficiency and (right) relative rejection factor for neutral hadrons for the loose cut set for p+p (open circles) and central ($b = 2$ fm, $dN/d\eta = 2700$) Pb+Pb collisions (filled triangles). These are averaged over the entire range $|\eta| < 2.4$

(R_{rel}). The former is defined as the fraction of photons passing the cuts. The latter is defined simply as the ratio of the efficiencies for γ and neutral hadrons,

$$R_{\text{rel}} = \frac{\epsilon_{\gamma}}{\epsilon_{\pi^0+\eta}} \quad . \quad (10.1)$$

The relative rejection basically reflects the gain on the signal (direct photon yield) relative to background (neutral hadron yield). The absolute rejection can also be used, which is defined as

$$R_{\text{abs}} = \frac{1}{\epsilon_{\pi^0+\eta}} \quad , \quad (10.2)$$

thus $R_{\text{abs}} \approx R_{\text{rel}}$ if the efficiency for direct photons is close to one.

In this analysis, two sets of cuts have been developed, a “loose” cut set and a “tight” cut set. The performance for these two sets is summarized in Fig. 10.3 for the loose cuts and in Fig. 10.4 for the tight cuts. The variations from point to point are not due to statistical fluctuations, which typically are smaller than the symbol size, but are caused by the fact that the cuts are currently tuned by hand bin-by-bin in E_T . The loose cuts give a factor of 1.5–3 relative rejection with a photon efficiency of about 90%; the tight cuts give a factor of 3–5 relative rejection with an efficiency of about 50%. The efficiency is tuned to be roughly independent of E_T , η , and centrality. The corresponding rejection factors were found to vary weakly with the E_T , η , and centrality. The η dependence (not shown) is roughly $\pm 25\%$ relative to the η -averaged value with the best performance near midrapidity. These results suggest that the best performance can be achieved for 30–50 GeV photons.

The identified photons are well reconstructed, even in heavy ion collisions. Figure 10.5 shows the position resolution in ϕ and η averaged over the entire acceptance as a function of E_T . The resolution is shown for single photons (labeled as $dN/d\eta = 0$) and for photons embedded in Pb+Pb

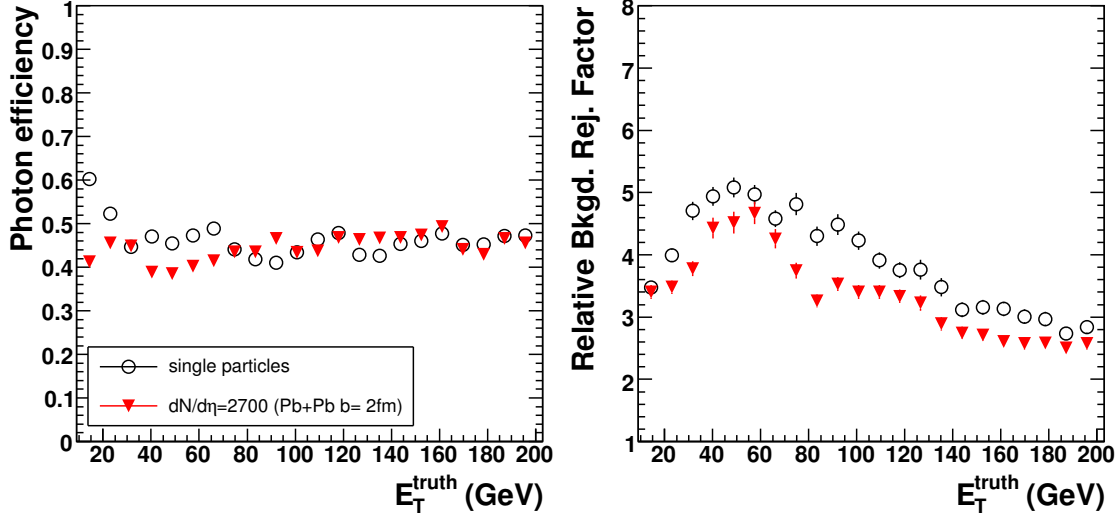


Figure 10.4: (left) Photon identification efficiency and (right) relative rejection factor for neutral hadrons for the tight cut set for p+p (open circles) and central ($b = 2$ fm, $dN/d\eta = 2700$) Pb+Pb collisions (filled triangles). These are averaged over the entire range $|\eta| < 2.4$.

collisions for three different centralities, indicated by their midrapidity particle densities. For E_T around 100 GeV, the η resolution is about 0.0003, while the ϕ resolution is about 0.0006 (0.6 mr). Figure 10.6 shows the relative resolution for E_T , again averaged over the acceptance, which is about 2% at an E_T of 100 GeV.

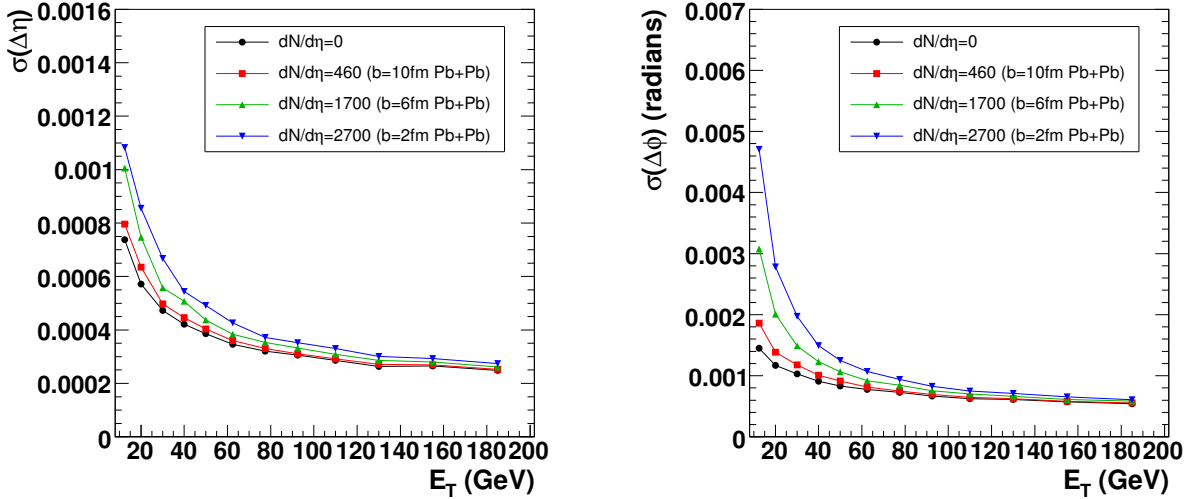


Figure 10.5: Angular resolution, (left) pseudo-rapidity and (right) azimuthal angle, vs. E_T for single photons and single photons embedded in Pb+Pb HIJING events.

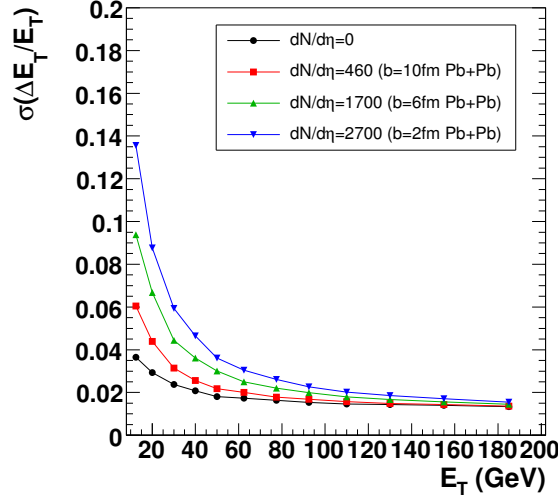


Figure 10.6: Relative energy resolution vs. E_T for reconstructed single photons and those embedded in Pb+Pb HIJING events.

10.3 Isolation cuts

One difference between direct photons and decay photons is that the direct photons are usually isolated but decay photons come from hadrons that are the fragments of jets: e.g. $\text{jet} \rightarrow \pi^0 \rightarrow \gamma + \gamma$. The decay photons typically merge into one cluster, but they have other hadrons in the neighboring angular space coming from the same original jet. Thus the direct photons can be distinguished from decay photons based on a set of isolation criteria. The isolation cuts are defined by using the charged tracks and total tower E_T in a cone around the jets. These cuts are tuned to maximize the rejection while keeping reasonable efficiency. This is achieved by varying the p_T threshold for charged tracks and the isolation cone size, or by varying the energy sum threshold and corresponding cone size. In general, the isolation efficiency drops with increasing cone size and decreasing p_T threshold or total E_T sum. The rejection, on the other hand, follows the opposite trend. We determine the best cuts separately for three Pb+Pb centralities and p+p and summarize them in Table 10.1. For example the cuts for most central Pb+Pb events require that all charged tracks in a cone of $0.02 < R < 0.2$ radians should be below 2.5 GeV in p_T , and the total energy in a cone of $R < 0.2$ radians surrounding the cluster should be less than $31 + 0.025E_\gamma$ GeV. The requirement of $0.02 < R$ is necessary to avoid false rejection of genuine isolated photons due to conversions.

The performance of the isolation cuts for p+p and central Pb+Pb events is summarized in Fig 10.7. In the most central collisions (corresponding to 0.5% of the cross-section in HIJING), the efficiency is about 65% and the absolute rejection is about 8 for $E_T > 50$ GeV. In p+p collisions, the efficiency is about 90% with an absolute rejection factor of about 16 above 50 GeV. Fig. 10.8 shows the corresponding performance for mid-central and peripheral Pb+Pb events. The increase of rejection with E_T is mainly due to the increase of jet multiplicity and jet energy which makes the isolation cut more effective.

	$dN/d\eta = 2700$	$dN/d\eta = 1700$
Track-based cut	$0.02 < R < 0.2$ $p_T < 2.5$ [GeV]	$0.02 < R < 0.25$ $p_T < 2.5$ [GeV]
Energy-based cut	$R < 0.2$ $\sum E_T < 31 + 0.025E_\gamma$ [GeV]	$R < 0.2$ $\sum E_T < 17.2 + 0.025E_\gamma$ [GeV]
Efficiency	0.60	0.70
Absolute rejection at 50 GeV	8	10
	$dN/d\eta = 460$	p+p
Track-based cut	$0.02 < R < 0.35$ $p_T < 2.0$ [GeV]	$0.02 < R < 0.5$ $p_T < 1$ [GeV]
Energy-based cut	$R < 0.2$ $\sum E_T < 5.6 + 0.025E_\gamma$ [GeV]	$R < 0.2$ $\sum E_T < 0.9 + 0.025E_\gamma$ [GeV]
Efficiency	0.70	0.91
Absolute rejection at 50 GeV	14	16

Table 10.1: The isolation cuts used in this analysis for three Pb+Pb centrality bins and p+p collisions. The track-based cut requires all charged tracks in the specified cone should have energy below the p_T threshold. The magnetic field also imposed a cut off of about 0.5 GeV. Similarly, the energy-based cut requires the total energy in the cone surrounding the cluster should be less than the threshold.

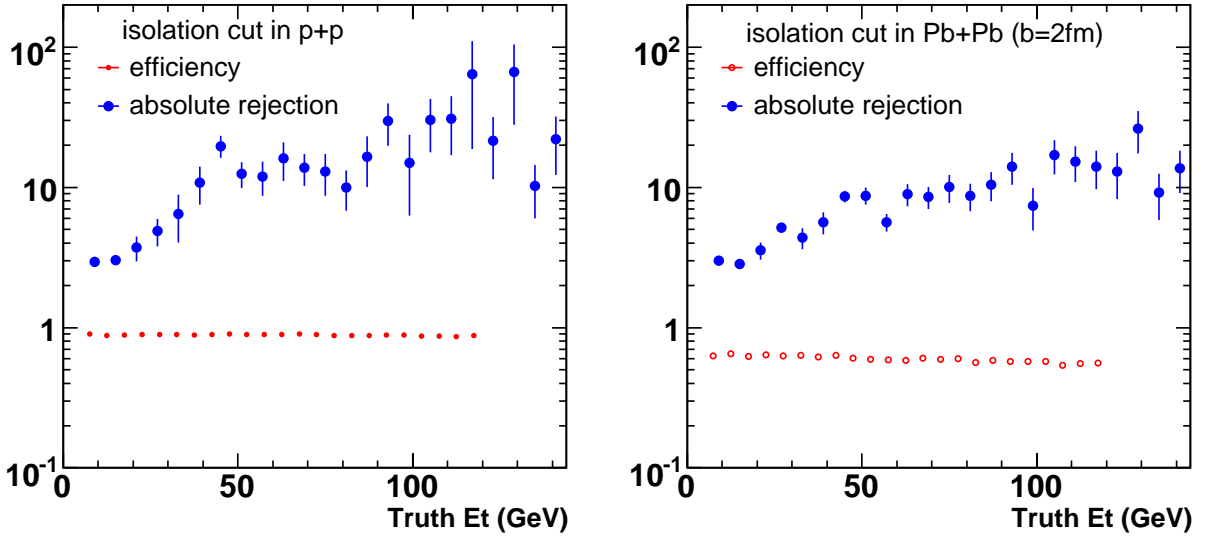


Figure 10.7: The photon efficiency and absolute rejection for background neutral hadrons for the isolation cuts (see Table. 10.1) as a function of energy in (left) p+p and (right) central Pb+Pb events.

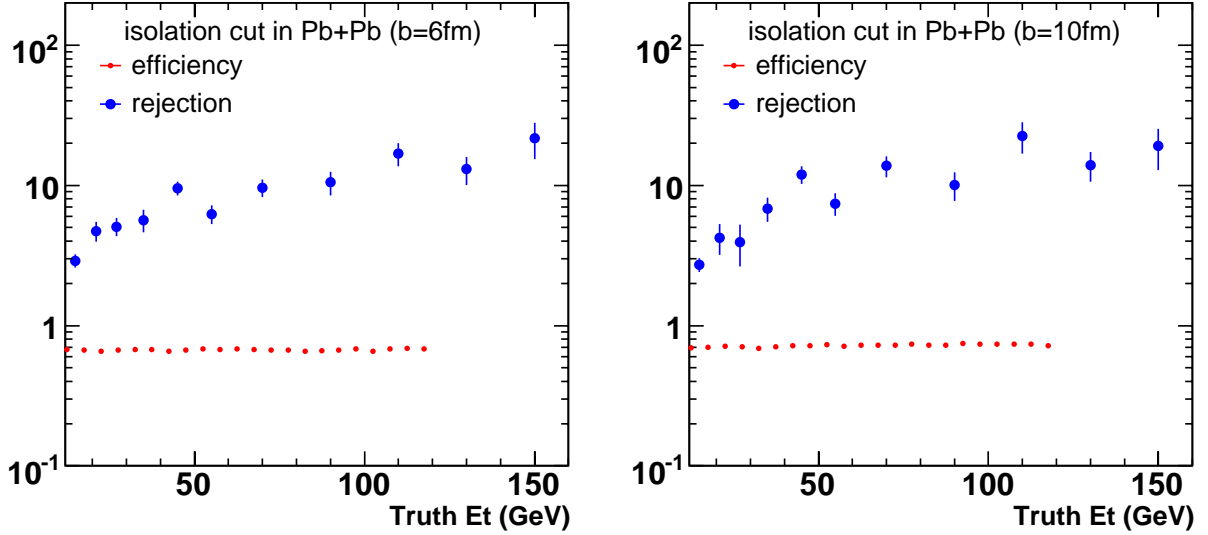


Figure 10.8: The photon efficiency and absolute rejection for background neutral hadrons for the isolation cuts (see Table. 10.1) as a function of energy in (left) $b=6$ fm and (right) $b=10$ fm Pb+Pb events.

10.4 Combined photon identification and isolation cuts

The combined performance for direct γ identification using both the shower shape and isolation cuts is summarized in Fig 10.9. In this study, about 140k PYTHIA di-jets are generated and embedded into the Pb+Pb HIJING events, similar to what was done for jet reconstruction in Chapter 6. To speed up the simulation, these di-jet events were generated with seven $\sqrt{Q^2}$ cuts in the 10–100 GeV range each with comparable statistics, which were then combined into a single jet spectrum by weighting them with the corresponding di-jet cross-section. PYTHIA also provides the spectra of π^0 and η mesons from jet fragmentation. After applying the γ -identification and isolation cuts, we obtain the spectrum of remaining neutral mesons that survive the cuts, which are the background for the direct photons.

To compare with the direct photon yield passing the same set of cuts, the NLO pQCD calculation of Fig. 10.1 is used to generate a realistic hadronic background. The expected direct photon yield is obtained by multiplying the expected spectra of π^0 and η mesons with the ratio $\gamma/(\pi^0 + \eta)$, which is then multiplied by the measured photon identification efficiency to obtain an estimated reconstructed photon spectrum. Figure 10.9 shows the spectra of jets (open circles), $\pi^0 + \eta$ (solid squares), $\pi^0 + \eta$ passing the cuts (solid circles), expected γ (solid line), and expected γ passing the cuts (dashed line). As the figure shows, above 60 GeV, the cuts suppress the yield of background neutral hadrons below the direct photon yield.

Figure 10.10 shows the ratio of direct photons to remaining neutral hadrons passing the cuts as function of photon energy in central Pb+Pb events. Assuming no suppression for neutral hadrons, $S/B = 1$ is reached for 100 GeV photons (left panel). By assuming a factor of 5 suppression of high p_T yields for π^0 and η [58], the S/B is improved by a factor of 5, which leads to a $S/B \sim 1$ for 30 GeV photons. This should be compared with the original S/B , which is less than 0.1 below

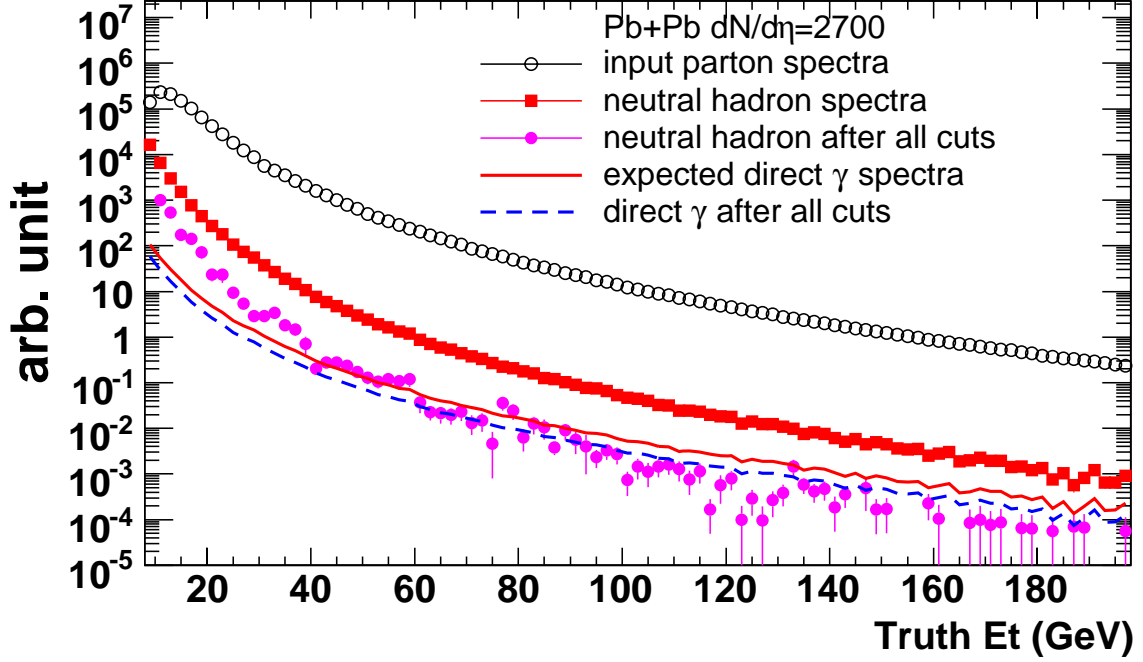


Figure 10.9: The performance of the shower shape cuts and isolation cuts on PYTHIA di-jets embedded into $b = 2$ fm Pb+Pb events. The spectra shown are for input jets (open circles), input $\pi^0 + \eta$ (solid square), remaining $\pi^0 + \eta$ (solid circles), expected direct γ (solid line) and direct γ surviving all cuts (dashed line).

100 GeV according to the NLO pQCD calculations shown in Fig. 10.1. Note that the improvement of S/B towards high E_T is partly due to the increase of $\gamma/(\pi^0 + \eta)$ ratio.

The centrality dependence of the direct photon performance is summarized in Fig. 10.11. The S/B ratio is the best in p+p collisions, which is about factor of 4–5 larger than that for most central Pb+Pb events. However, by taking into account the benefit one gains from the likely hadron suppression, we expect to achieve a similar level of performance that is approximately independent of the event centrality.

10.5 Rate estimate

The number of expected direct photons observed per year is based on the following assumptions:

- 3 weeks/year running at 60% up time, which gives 0.5nb^{-1} integrated luminosity for minimum bias Pb+Pb collisions;
- Estimation of the direct photon yield based on the next to leading order pQCD calculation shown in Fig. 10.1;
- Photon reconstruction efficiency of 50% passing the shower shape and isolation cuts;
- π^0 's and η 's are suppressed by a factor of 5 in central Pb+Pb collisions.

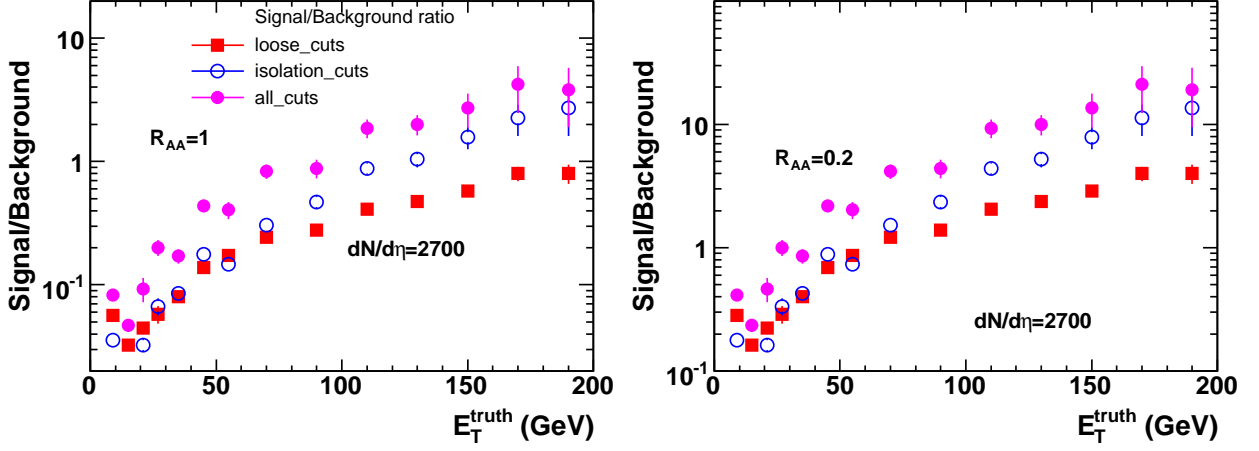


Figure 10.10: The ratio of direct photons over background neutral hadrons passing the loose shower shape cuts only (solid squares), isolation cuts only (open circles) and combined cuts (solid circles) in central Pb+Pb events, assuming (left) no suppression for hadrons, and (right) a factor of 5 suppression for hadrons.

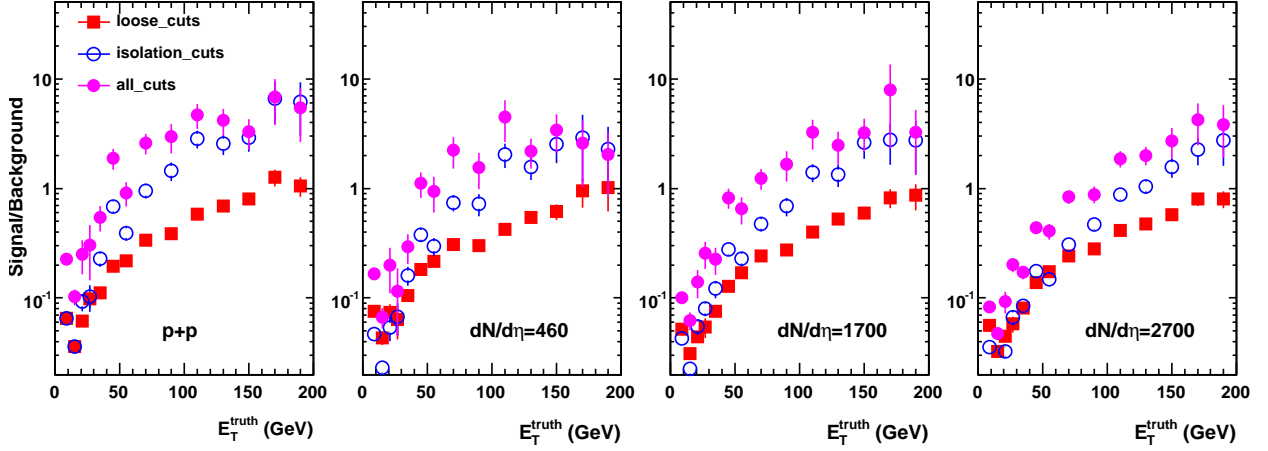


Figure 10.11: The ratio of direct photons over background neutral hadrons passing the loose shower shape cuts only (solid squares), isolation cuts only (open circles) and combined cuts (solid circles) for different occupancies under the assumption that the nuclear modification factor $R_{AA} = 1$, for all centralities.

Based on these assumptions, 200k (10k) γ will be measured above 30 GeV (70 GeV) per LHC year with $S/B > 1$ ($S/B > 4$).

10.6 γ -jet correlations

Once the direct photons are cleanly identified, the away-side jet can be reconstructed and it is feasible to study the correlation between the γ and jet. A first attempt at measuring such a coinci-

dence has been made. A set of PYTHIA γ -jet events was generated and embedded into the same set of HIJING events without quenching used for the jet performance study. Jet reconstruction was performed using the seeded cone algorithm with $R = 0.4$ and 5 GeV seed towers as described in Chapter 6. The photons were measured using the photon identification and isolation cuts outlined earlier.

Two different energy ranges for γ -jet correlations are shown in Figure 10.12. The left panel shows the $\Delta\phi$ correlation between isolated photons from 40–60 GeV with jets from the same energy interval. A clear away-side jet signal around $\Delta\phi = \pi$ is visible above the low, flat background. The right panel shows a similar correlation for isolated photons and jets in 60–80 GeV range. The jet signal peak is more significant comparing to the low background. In the 40–60 GeV energy range, fake jets were removed by applying the same rejection cut on $\sigma_{j_T}^{\text{sum}}$, which was used in the jet performance study (see discussion in Chapter 6 and Figure 6.9). For the correlation in 60–80 GeV bin, the fake jets haven't been removed to shows the upper limit of the expected background. The γ -jet S/B as a function of the fake jet rejection cut is shown in Fig. 10.13. The cut used to remove fake jets was $\sigma_{j_T}^{\text{sum}} < -2.5$. These γ -jet correlations can be used to improve jet energy scale calibration, to reject background jets and to improve the reconstruction efficiency by testing for a coincidence with isolated photons.

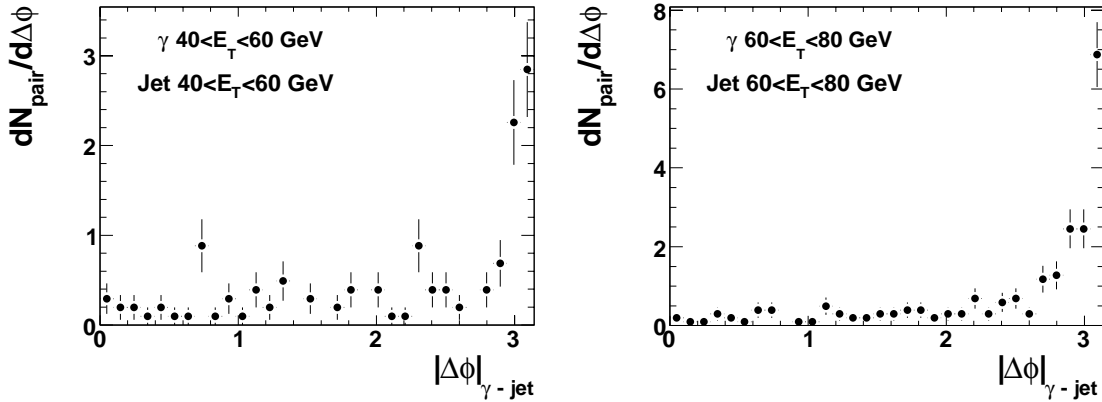


Figure 10.12: Correlations in $\Delta\phi$ for γ -jet pairs where both the photon and the jet have 40-60 GeV (left) and 60-80 GeV (right) in E_T .

10.7 Unique ATLAS capabilities

ATLAS's large acceptance allows full jet reconstruction in 2π and up to 10 units in pseudo-rapidity ($|\eta| < 5$) with $> 50\%$ efficiency for jets above 50 GeV in central Pb+Pb collisions (see Fig.6.12). The results shown in this chapter show that ATLAS can reconstruct a highly-pure sample of direct photons above $E_T = 20$ GeV over nearly 5 units in pseudo-rapidity ($|\eta| < 2.4$) with a constant 50 – 60% efficiency even for central Pb+Pb collisions with $dN/d\eta = 2700$. Combined with the measurement of global properties of the collision (as discussed in Chapter 5), this should allow a detailed study of γ -jet tomography as a function of centrality and angle relative to the reaction

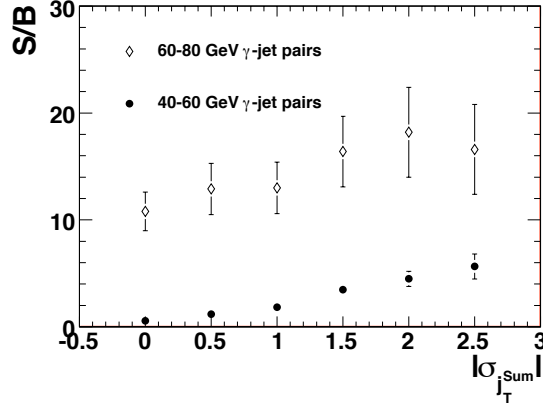


Figure 10.13: The resulting γ -jet signal-to-background in the peak region for both sets of E_T bins.

plane in a broad E_T and η range.

ATLAS's sophisticated calorimeter system provides γ and γ -jet capabilities which are competitive, and often superior, compared to ALICE and CMS. Compared to ALICE, the advantage of the ATLAS detector lies in its large detector acceptance (see Figure ??) coupled with its high rate triggering capability. Compared to CMS, which also has a large acceptance calorimeter and a similar trigger system, the advantage of the ATLAS design is its longitudinally segmented calorimeter, and especially the finely-segmented strips in the first layer. This will allow the discrimination between γ 's and neutral hadrons independent of the isolation cuts. In the case of γ -jet, this should allow ATLAS to extend the measurements down to $E_T = 20$ GeV.

One area where the ATLAS calorimeter provides capabilities completely unmatched by the other LHC experiments is the measurement of medium induced photons over the full experimental acceptance. Recent theoretical calculation constrained by existing photon data have suggested that direct photons coming from final-state sources — such as fragmentation, in-medium gluon conversion and medium-induced bremsstrahlung — can dominate the direct photon yield up to $p_T = 50$ GeV [83]. These are compelling phenomena to address since their production rate directly reflects the interaction of quarks and gluons as they propagate through the medium.

Fragmentation and medium-related photons are not straightforward to measure in general, as they are produced close to the primary jet, and thus can not be extracted using isolation cuts. Fortunately, the first layer of the ATLAS electromagnetic calorimeter, as discussed in section 10.2, has sufficiently fine segmentation in η that it can resolve fragmentation photons even within jets. Fig.10.4 suggests that even without isolation, a tight γ identification cut can provide a unbiased, centrality-independent relative rejection factor of 3 to 5 against the hadronic decay background with about 50% efficiency for the photons. Assuming the yield of medium-induced photons is roughly equal to that of prompt photons, as suggested by recent NLO calculations, a S/B of about 0.3 will be achieved at around $E_T = 50$ GeV in central Pb+Pb collisions. This will allow a statistical subtraction of the hadronic background and facilitate the first measurement of medium-induced photons in heavy ion collisions over a large acceptance, and thus down to very low x .

10.8 Summary

This chapter has presented the ATLAS performance for direct photon identification and γ -jet correlation measurements.

- The first layer of the ATLAS EM calorimeter provides an unbiased relative rejection factor against background neutral hadrons of either 1.5–3 (loose shower shape cuts) or 3–6 (tight shower shape cuts) for neutral hadrons.
- The loose γ identification cuts can be combined with isolation cuts which can provide an additional factor of about 10 relative rejection. This results in a total relative rejection of about 20 even in central Pb+Pb collisions.
- The photon efficiency is constant at 60% down to $E_T = 20$ GeV for central Pb+Pb allowing the study of medium modification for low- E_T jets.
- Identified direct photons can improve the reconstruction efficiency and S/B significantly for jets below 80 GeV, relative to the performance for jet reconstruction without tagging.
- The tight shower shape cuts alone provide sufficient rejection against hadron decays within jets to allow the study of fragmentation photons, in-medium gluon conversion and medium-induced bremsstrahlung. This is a unique capability of ATLAS.
- The expected luminosity per LHC Pb+Pb year will provide 200k photons above 30 GeV with $S/B > 1$, and 10k above 70 GeV per LHC year with $S/B > 4$.

Chapter 11

Trigger & DAQ

The ATLAS data acquisition system is well suited to carrying out the measurements described in this proposal both in terms of readout capability and triggering. This chapter briefly summarizes the design of the ATLAS data acquisition system (DAQ), discusses the conditions under which the DAQ system will operate during Pb+Pb running, and describes the strategy for minimum-bias and rare process triggering during heavy ion data-taking.

11.1 ATLAS data acquisition system

ATLAS has implemented a traditional collider data acquisition system [84] (see diagram in Fig. 11.1) utilizing a three-level trigger system that can, in principle, sample every bunch crossing at 40 MHz while reducing the rate of recorded events to a few hundred Hz, limited by an aggregate data rate of 300 MByte/sec (a number that will be relevant for heavy ion estimates in Chapter ??). Data from all detector channels are sampled and stored in either analog or digital form at the bunch crossing frequency.

The ATLAS Level-1 trigger [85] uses data from the electromagnetic and hadronic calorimeters, the Muon trigger chambers, trigger scintillators, and (for Pb+Pb operation) the ZDC to make a decision to keep or reject data from a bunch crossing within $2.5 \mu\text{s}$ of crossing. Data from events selected by the Level-1 trigger – up to a maximum rate of 75 kHz – are partially read out and processed by the Level-2 trigger processor farm. Events selected by the Level-2 trigger up to a maximum rate of 1 kHz are completely read out and then subjected to offline style analysis in the ATLAS “Event Filter” farm. Events selected by Event Filter algorithms are transmitted to the ATLAS Tier 0 system for recording and immediate analysis.

During high luminosity ($10^{34} \text{ cm}^{-2}\text{s}^{-1}$) p+p operation of the LHC there will be ~ 20 minimum-bias p+p collisions per bunch crossing. Under these conditions the total data volume read out from a single crossing is expected to be ~ 1 MByte. The ATLAS DAQ system is designed to have sufficient throughput to read high-luminosity events out to the Event Filter farm at the maximum 1 kHz rate. These performance specifications will be used below to evaluate the DAQ performance under Pb+Pb conditions. The data from the ATLAS calorimeters provides the bulk of the estimated p+p events size as no zero suppression is applied in the calorimeter readout.

The ATLAS Level-2 and Event Filter systems – together referred to as the “High Level Trigger” (HLT) – were designed to find jets, photons, muons, and other desired signatures of interesting

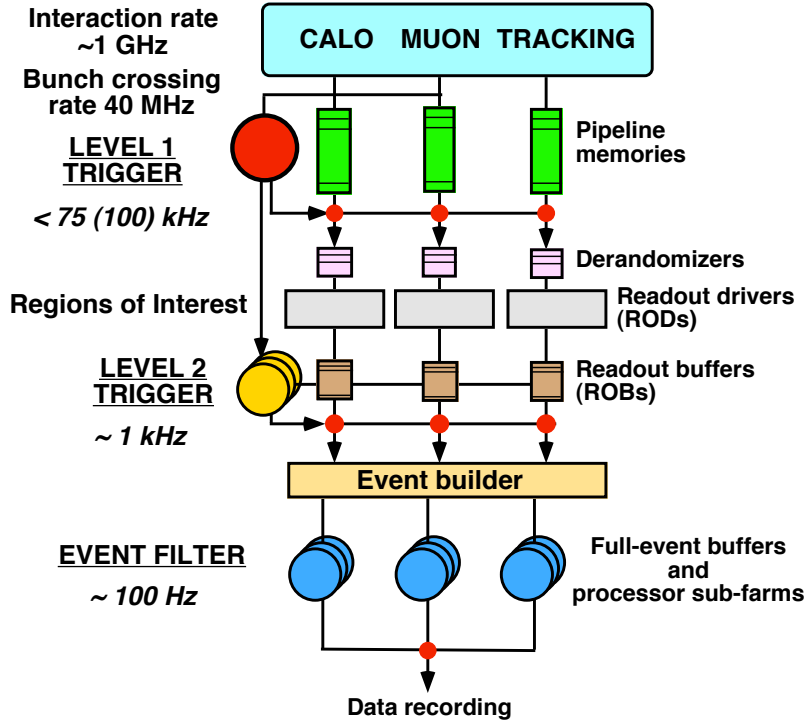


Figure 11.1: Schematic of the ATLAS data acquisition system.

physics in “Regions of Interest” (ROIs) identified by the Level-1 trigger. Each jet, photon, and/or muon candidate satisfying a Level-1 trigger criterion has a corresponding geometrical region that guides subsequent Level-2 and Event Filter analysis that refines the Level-1 trigger decision and ultimately determines whether data from a given crossing are transmitted to the Tier 0 system for archiving. The combination of Level-1 trigger/ROI, Level-2 trigger algorithm, and Event Filter algorithm that select a specific physics pattern are collectively referred to as a “trigger slice.”

11.2 Pb+Pb conditions

Based on the maximum anticipated Pb+Pb luminosity of $1 \times 10^{27} \text{ cm}^{-2}\text{s}^{-1}$ [86] and assuming a Pb+Pb total cross-section of 7.7 b [87], we expect a maximum Pb+Pb hadronic collision rate of 7.7 kHz. This rate is a factor of 10 below the maximum Level-1 trigger rate so the full minimum-bias Pb+Pb rate can be sampled by the Level-2 trigger. Nonetheless, the Level-1 trigger will be used as described below to find jets, photons, and muons at Level-1 to provide regions of interest for Level-2 and Event Filter processing.

We have estimated an average minimum-bias event size of 5 MByte for Pb+Pb collisions using HIJING followed by complete GEANT4 simulations of the detector response (see Chapter ?? for more thorough discussion of event size). The modest increase in event size from p+p to Pb+Pb collisions is largely due to the fact that the calorimeter readout has no zero suppression. The increased event size will reduce the maximum rate at which events can be transferred to the Event

DAQ Stage	Input Rate (Hz)	Max. Output Rate (Hz)	Max. Rejection
Level-1	$< 8 \times 10^3$	75×10^3	none
Level-2	$< 8 \times 10^3$	900	9
Event Filter	900	50	16

Table 11.1:]

Estimated maximum minimum-bias Pb+Pb event rates through different components of the ATLAS DAQ system and resulting upper limits of rejection required in each stage of trigger system

Filter farm. The specification for the ATLAS Event Builder which performs the complete readout of all events selected by the Level-2 trigger is that it should be able to read a aggregate data rate of 4.5 GBytes/s. Based on the above heavy ion event size we estimate a maximum sustained rate of Level-2 accepts of 0.9 kHz during Pb+Pb operation. The specification for the maximum archiving bandwidth from ATLAS is 300 MByte/s. Based on the estimated event size, this gives an archiving rate of approximately 60 events/s. These numbers are summarized in Table 11.1.

11.3 Pb+Pb minimum bias triggers

A well-understood minimum bias trigger is essential to the success of the heavy ion program. The uncertainty in the fraction of total inelastic cross section sampled by this trigger translates directly into an uncertainty on centrality variables (e.g. N_{part} , N_{coll} , or b) which gets significantly worse in more peripheral events. The RHIC program showed clearly that a variety of triggering schemes should be used, with careful offline cuts and various extrapolation techniques, to reduce this uncertainty. Doing this, all of the RHIC experiments kept uncertainties down to a few percent, even with triggers having less than 90% efficiency.

Multiple triggers are available for use as Pb+Pb minimum-bias triggers. The ZDC, described in the previous chapter, will provide a trigger whose efficiency is expected to be better than 90%. The ATLAS Minimum Bias Trigger Scintillators (MBTS) were designed to increase the efficiency for triggering on minimum-bias collisions in p+p collisions. Located at $2.4 < |\eta| < 3.8$, the MBTS has similar coverage as multiplicity/trigger detectors used in RHIC experiments and will provide a Pb+Pb minimum-bias trigger with $\approx 100\%$ efficiency in Pb+Pb collisions. However, the MBTS is not expected to survive beyond early low luminosity runs due to radiation damage. The ATLAS Level-1 trigger has implemented a sum of the total transverse energy, ΣE_T , in the electromagnetic, hadronic, and forward calorimeters. A detailed study of the performance of the ΣE_T trigger including calorimeter suggests that the ΣE_T trigger would have an efficiency of 85% for a noise trigger rate $< 10\%$ of the true Pb+Pb minimum-bias trigger rate.

Beam-gas and halo events and other backgrounds will be removed in the HLT, which has more than sufficient capacity given that it is designed for 75 kHz input rate and the maximum heavy ion rate will be only about 10% of that. Various algorithms involving silicon spacepoints and tracks are being optimized for early p+p running, and we expect to be able to adapt these for heavy ion running. While the large occupancy will challenge these algorithms for more central events, these events are highly unlikely to ever arise from backgrounds, and so a simple threshold on the MBTS total energy should be sufficient to tag them as good events. Conversely, the lower

multiplicities will have a larger background contamination but in these the p+p algorithms should work properly.

11.4 Rare signal triggers

As noted in Section 11.2, no Level-1 trigger rejection is required during Pb+Pb running. However, the Level-2 and Event Filter trigger processing is designed to take advantage of ROIs generated by the Level-1 trigger, so we will use the Level-1 trigger to find jet, photon, and muon ROIs that will provide the starting point for later trigger processing. Because we do not need rejection at Level-1, we can set the relevant thresholds such that there are up to a few ROIs per event compatible with the typical ROI rate for Level-1 selected p+p events. The rare triggers of interest in Pb+Pb collisions include: jets, high- p_T photons/electrons, single/di-muons and Z 's. Each of these triggers depends either on a calorimeter based trigger (jets, photons, electrons) and/or a muon trigger. We describe the Level-1 trigger strategy for each of these separately. Our studies of the performance of Level-2 and Event Filter algorithms on Pb+Pb events are not yet complete, but we expect the efficiency and resolution of the combined Level-2/Event Filter algorithms to be similar to the results presented in Chapters ??-?? as the algorithms are similar to the offline algorithms used in the presented physics studies.

11.5 Pb+Pb jet and photon triggers

11.5.1 Level-1

The ATLAS Level-1 trigger is designed to trigger on jets using an overlapping tiling of trigger towers of size $\Delta\eta \times \Delta\phi = 0.2 \times 0.2$ whose energies are calculated in the calorimeter readout electronics using a combination of analog and digital sums. The Level-1 jet sums are generated for tiles that cover $\Delta\eta \times \Delta\phi$ regions of 0.4×0.4 , 0.6×0.6 and 0.8×0.8 . The ATLAS jet trigger allows for 8 possible thresholds on each of the different tile sizes. Tiles that provide a local maximum E_T and pass at least one of the jet trigger E_T thresholds are candidate Jet ROIs. The ROIs are tagged according to which threshold they satisfy and the list of generated ROIs is available for readout by the Level-2 trigger.

Because of the large backgrounds in heavy ion events, only the 0.4×0.4 tiles will be useful. As noted above, the primary role of the jet Level-1 trigger for heavy ion operation is to provide the ROIs for use in the HLT. The specification for the Level-2 readout of Level-1 jet trigger ROIs allows a maximum sustained rate of 24 jet ROIs to be read out per event. The lower Pb+Pb Level-1 trigger rate would allow, in principle, a larger number of ROIs per event, but our goal will be to keep the number of ROIs much lower – comparable to the number of expected ROIs per event in p+p collisions – while preserving maximum efficiency for finding ROIs for lower energy jets. We initially set a target of 5 ROIs per event accounting for contributions only from the underlying event; but as will be shown below, this criterion yields thresholds that are unnecessarily low.

The left panel of Figure 11.2 shows the distribution of transverse energy in the 0.4×0.4 ROIs, $E_T^{4 \times 4}$, due to the “underlying event” in Pb+Pb collisions for four different centrality bins. Because of the baseline shift in the $E_T^{4 \times 4}$ energies resulting from the Pb+Pb underlying event, the distribution shifts to larger energies for more central collisions. The right panel of Figure 11.2

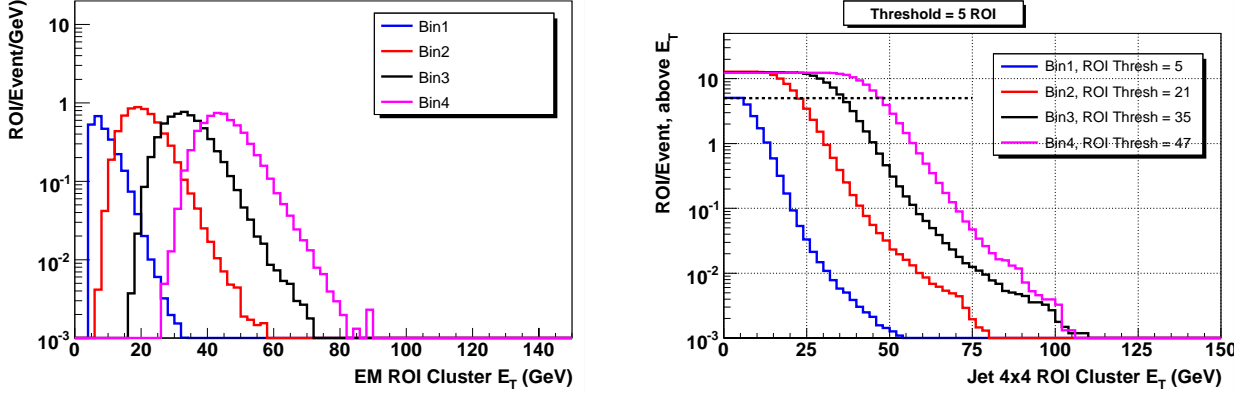


Figure 11.2: Level-1 jet 0.4×0.4 ROI E_T distributions in HIJING simulated Pb+Pb events for four centrality bins, 75-100%, 50-75%, 25-50%, 0-25% indicated as bins 1-4, respectively. *left* - differential ROI E_T distribution, *right* - Integral distribution giving # of ROIs per above a given E_T . The thresholds corresponding to a requirement of no more than 5 ROIs per event are indicated in the legend.

shows the integral distribution corresponding to Fig. 11.2 expressed in terms of the number of ROIs per events satisfying a given $E_T^{4 \times 4}$ threshold. A single threshold of 50 GeV would yield no more than a few ROIs per event for all collision centralities. However, such a single threshold would not be ideal because it would produce an inefficiency for jets with $E_T < 50$ GeV in non-central collisions. We indicate in the right panel of Fig. 11.2 $E_T^{4 \times 4}$ values which give 5 ROIs per event for the four chosen centrality bins. Since the distributions in Figure 11.2 represent only the contribution from the underlying event, real jets will add to the energy in the ROIs. Thus, for events in the 50-75% centrality bin (e.g.) a threshold of 21 GeV will satisfy to requirement of 5 ROIs per event, but that places the threshold only marginally above the most probable value of 20 GeV and only ~ 10 GeV above the low edge of the $E_T^{4 \times 4}$ distribution in that centrality bin. Thus, such a threshold would nominally correspond to a jet threshold of 10 GeV for ROIs with underlying event E_T on the low side of the $E_T^{4 \times 4}$ distribution, and essentially zero threshold for ROIs on the high side of the $E_T^{4 \times 4}$ distribution. Clearly, these numbers are too low to be practical, so in reality we would likely choose thresholds larger by at least 10 GeV which would reduce the number of ROIs per event produced purely by the underlying event) by a factor of 10. This analysis demonstrates that we can choose a set of thresholds that produce an acceptably small number of ROIs per event while also providing the ability to set the effective jet E_T thresholds as low as 10-20 GeV. In practice, we would likely implement eight (8) evenly spaced thresholds varying from 20 GeV to 50 GeV (e.g.) that would allow finer gradations in the association of jet thresholds with centrality.

In addition to the jet regions of interest described above, the ATLAS Level-1 trigger also provides the ability to trigger on photons and τ 's using information from the calorimeter. The diagram in Figure 11.3 illustrates the function of the photon trigger. The photon trigger starts with electromagnetic towers of size $\Delta\eta \times \Delta\phi = 0.1 \times 0.1$. The largest energy tower pair within a 0.2×0.2 region with E_T greater than one of eight thresholds, satisfying a cut on the electromagnetic energy in a surrounding "isolation" ring and cut on the total hadronic energy in a 4×4 region including

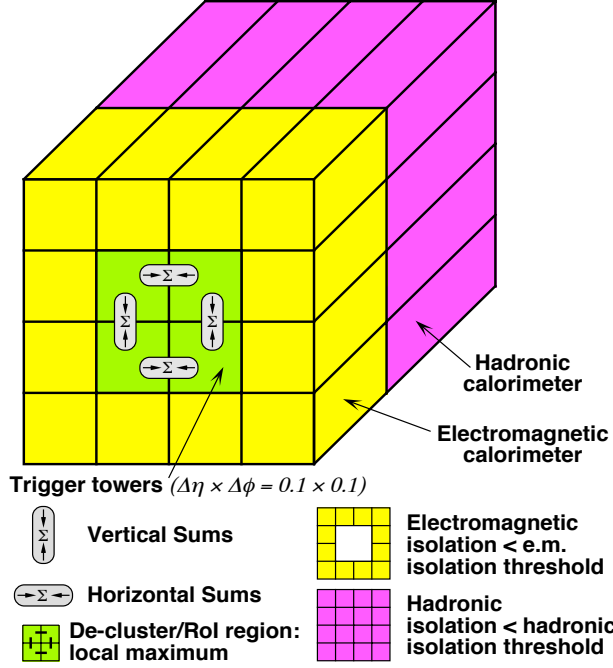


Figure 11.3: Diagram illustrating the Level-1 electromagnetic ROI algorithm

the 2×2 region and the surrounding isolation ring becomes an electromagnetic ROI (EM ROI). The distribution of EM ROI E_T , E_T^{EM} , values is shown in Fig. 11.4 together with the corresponding integral distribution. Because the EMROIs cover a much smaller $\Delta\eta \times \Delta\phi$ region, the baseline shift is much smaller in the E_T^{EM} distributions compared to the $E_T^{4 \times 4}$ distributions. A single E_T^{EM} threshold at 20 GeV would be sufficient to trigger on 20 GeV photons (e.g.) over the entire centrality range and would generate < 0.01 EMROI per event.

In fact, we obtain sufficient rejection simply with a cut on E_T^{EM} that we would not need to use the isolation cut at Level-1. By avoiding the isolation cut at Level-1 we avoid having to accommodate the effect of the underlying event in the isolation ring, *and* we can use the Level-1 EM trigger to reduce an inefficiency in the Level-1 jet trigger. Extreme downward fluctuations in the underlying event for a given ROI in a given centrality bin may cause a jet to not satisfy the ROI threshold expected for the given centrality. However, a significant fraction of such jets will have a neutral hadron with sufficient energy that it could be selected by the EM trigger – which is much less sensitive to the fluctuations in the underlying event. The Level-1 calorimeter trigger also implements a “tau” region of interest similar to the EMROI but including the hadronic layers. The ROIs also can be used to improve Level-1 trigger efficiency for jets at low E_T . A first evaluation of the combined performance of the jet 0.4×0.4 , EM and Tau ROIs for finding jets in 0-25% Pb+Pb collisions gives an efficiency $> 90\%$ for jet $E_T > 30$ GeV.

Alternatively, if we apply a similar analysis as used for the jet ROIs above with a more restrictive requirement of no more than 3 ROIs per event, we obtain a set of centrality dependent thresholds that are all < 10 GeV and vary by 2 GeV between centrality bins except for the most peripheral bin. For the most central bin where the baseline shift is the largest, the E_T^{EM} value giv-

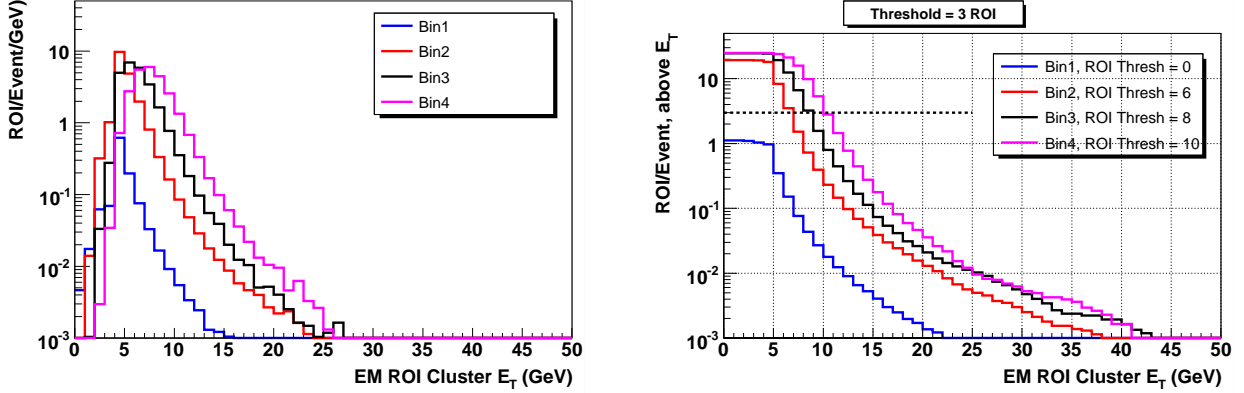


Figure 11.4: Level-1 Electromagnetic ROI E_T distributions in HIJING simulated Pb+Pb events for four centrality bins, 75-100%, 50-75%, 25-50%, 0-25% indicated as bins 1-4, respectively. *left* - differential ROI E_T distribution, *right* - Integral distribution giving # of ROIs per above a given E_T . The thresholds corresponding to a requirement of no more than 3 ROIs per event are indicated in the legend.

ing 3 ROIs per event is only 3 GeV larger than the most probable E_T^{EM} and is 5 GeV above the low edge of the E_T^{EM} distribution. Thus, even for the central events with the most background fluctuations, we could set an effective photon threshold as low as 5 GeV. While we would likely never try to trigger at such a low energy, the ability to push the Level-1 threshold so low means that the Level-1 ROI finding has minimal impact on the final trigger efficiency.

11.5.2 Level-2 and event filter

The Level-2 trigger will provide the first real rejection during Pb+Pb data-taking. The Level-2 trigger has access to all of the data generated by the Level-1 trigger including jet and photon ROIs and the ΣE_T from the calorimeters (see Section 11.3, which allows characterization of Pb+Pb collision centrality). This ΣE_T value will be used to select the jet and photon ROI by evaluating (e.g. with a look-up table) the appropriate thresholds corresponding to the event centrality measured by ΣE_T . Data from the calorimeter corresponding to these regions of interest will be fetched by the Level-2 trigger and used to perform jet and photon reconstruction.

For Pb+Pb collisions, the cone jet reconstruction algorithm will perform a background subtraction based on the ΣE_T value while the k_T algorithm will be used as implemented in the offline analysis (see Section 6.3.2). Since the p+p implementation of the Level-2 trigger uses the full set of calorimeter cells for performing the jet finding, the only additional time spent in the Level-2 jet algorithm for Pb+Pb collisions will be the step of subtracting the estimated background value from the calorimeter cells (for the cone algorithm) and evaluating discriminant quantities to remove false jets. Events selected as satisfying a jet Level-2 trigger will be re-analyzed in the Event Filter using more complete calibrations and corrections and using the same background subtraction procedure as used in the offline analysis. We, therefore, expect the performance of the Event Filter algorithm to be identical to the results shown in Section 6.4.2.

The thresholds that will be applied at Level-2 and in the Event Filter will depend on the actual

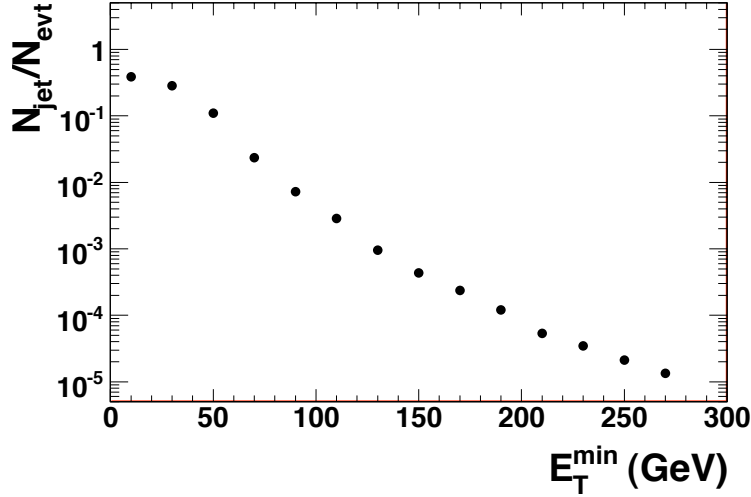


Figure 11.5: Estimated number of jets per event in the ATLAS acceptance above a given E_T in minimum-bias Pb+Pb collisions.(see text for details).

jet production rates including the effects of shadowing and quenching, and properties of the Pb+Pb underlying event and also will depend on the fraction of the 50 event/s recording rate allocated to jet triggers. Figure 11.5 shows a plot of the estimated number of jets per event produced in the ATLAS acceptance above a given E_T as a function of E_T assuming no quenching and neglecting shadowing. This result was obtained from the Pythia cross-sections used in Section 6.4.1 scaled by T_{AB} , and integrated over $|\eta| < 5$ and presented as the number of jets per minimum-bias Pb+Pb collision above a given E_T . These numbers are uncertain to at least a factor of two due because of NLO contributions not accounted for by the k -factor in PYTHIA, shadowing of nuclear PDFs not included in Pythia, unknown effects of jet quenching (see Fig. 6.6), and other effects. However, Fig. 11.5 shows clearly that the jet rates in Pb+Pb collisions at the LHC will be high, with more than one $E_T > 100$ GeV jet in a thousand Pb+Pb events. If we suppose that 20% of the recording bandwidth is dedicated to jet triggers, at full luminosity a jet E_T threshold of > 100 GeV would be required to reduce the 7.7 kHz minimum-bias rate to 10 Hz. However, at lower luminosities – either during a first LHC Pb+Pb run or later in stores – a trigger as low as 50 GeV could be utilized. In fact, a mixture of jet thresholds will be used with scale downs to collect statistics over the entire E_T range. Nonetheless, all the practically useful triggers will be well above the low jet ROI thresholds discussed above.

11.5.3 Pb+Pb muon triggers

Muon triggering is provided by Resistive Plate Chambers (RPC) in the barrel region and Thin Gap Chambers (TGC) in the end-caps. The ATLAS Level-1 Muon trigger system is designed to select events with single muons passing one or more p_T threshold or events containing two muons passing one or more of the thresholds. In the current off-line implementation of muon trigger emulation, di-muon triggers do not have invariant mass cut; the only requirement is that an event has two muons with p_T above the applied threshold.

The Level-1 muon trigger efficiency was studied using PYTHIA simulated p+p events con-

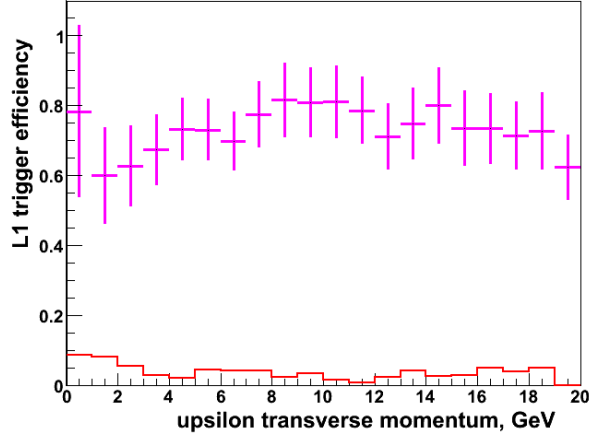


Figure 11.6: Level-1 Y trigger efficiency as a function of Y p_T obtained using PYTHIA p+p events with forced Y production merged into minimum bias Pb+Pb HIJING and using default p+p muon trigger thresholds. Magenta points show single muon trigger efficiency (any Level-1 single muon trigger fired), while red histogram shows di-muon trigger efficiency (two muons passing trigger thresholds). Error bars show statistical errors only.

taining Y 's that were merged with minimum bias Pb+Pb HIJING events. The default p+p trigger thresholds were used with the lowest threshold corresponding to $p_T \approx 6$ GeV/c. The trigger efficiency was defined as the number of events in which an Y was reconstructed and trigger fired, divided by the number of events in which an Y was reconstructed. The results for the Level-1 efficiency are shown in Fig. 11.6 as a function of Y p_T . As shown in the figure, the trigger efficiency is rather low, especially if the Y s are required to pass a Level-1 di-muon trigger. However, this low efficiency results primarily from the default muon p_T threshold of 6 GeV/c. Due to the Y decay kinematics the probability to have both muons with $p_T > 6$ GeV/c is very low.

Since rejection is not needed at Level-1, we will use multiple strategies to achieve higher Y trigger efficiency. First we can lower the p_T cut on the muons down to a minimum of 3.5 GeV/c. By reducing the cut we will improve the likelihood that both muons are found by the Level-1 trigger allowing a real invariant mass cut on be applied at Level-2. Second, we will accept some rate (yet to be determined) of single muon triggers through to the Event Filter where the full offline muon reconstruction can be performed. Assuming that the rejection provided by the single muon trigger at 6 GeV/c is sufficient to allow all selected events through to the Event Filter, the resulting Y efficiency would be approximately that of the single muon curve shown in Fig. 11.6. Ultimately, a combination of single and di-muon triggers with a variety of p_T thresholds will be used at Level-1 to seed Level-2 and Event Filter algorithms – similar to the jet and photon trigger schemes described above. The combined performance of the resulting muon trigger slices is underway. We note that the single muons found at Level-1 can also be correlated with jets at Level-2 and in the Event Filter to select heavy flavor jets for archiving.

11.6 Summary

The ATLAS data acquisition and trigger system is well suited to carry out the Pb+Pb measurements described in this proposal. During Pb+Pb operation ATLAS will record roughly 50 Pb+Pb events per second. Multiple triggers can, and will, be used as Pb+Pb minimum-bias triggers, including a ZDC coincidence trigger, a scintillator-based coincidence trigger (MBTS), and a calorimeter ΣE_T threshold trigger. The combination of these triggers is expected to provide a minimum-bias Pb+Pb efficiency $> 95\%$. For rare signals no rejection is needed at Level-1 for all expected Pb+Pb luminosities, but the Level-1 trigger will be used to find “Regions of Interest” that will be used in Level-2 trigger and the Event Filter to select jets, photons, and muons and a fraction of minimum-bias Pb+Pb events for recording. The threshold for the jet and electromagnetic regions of interest can be set low enough to have little or no impact on the trigger efficiency for jets and photons. The Level-2 trigger will use fast versions of offline algorithms to reconstruct jets with background subtraction and find electromagnetic clusters. The Event Filter will run full offline analysis on the regions of interest found by Level-1 and surviving Level-2 cuts. The resulting performance for jet and photon finding in the combined Level-2 and Event Filter systems will be similar to the results presented in Chapters ?? and ?. For Y measurements, the default p+p Level-1 di-muon trigger is found to be inefficient in selecting Y s at Level-1. However, since rejection is not needed at Level-1, a combination of single muon and di-muon triggers with lowered p_T thresholds at Level-1 will seed Level-2 and Event Filter algorithms that can select Y s based on invariant mass cuts and with better efficiency. The Level-1 single muon triggers will also provide the ability to select heavy flavor jets at Level-2 and in the Event Filter.

Chapter 12

Summary

Bibliography

- [1] *Quantum Chromodynamics and the Theory of Superdense Matter*, E. V. Shuryak, Phys. Rept. **61**, 71 (1980).
- [2] *Universal features of QCD dynamics in hadrons and nuclei at high energies*, R. Venugopalan (2007), 0707.1867.
- [3] *Manifestations of high density QCD in the first RHIC data*, D. Kharzeev and E. Levin, Phys. Lett. **B523**, 79 (2001), nucl-th/0108006.
- [4] *Viscosity in strongly interacting quantum field theories from black hole physics*, P. Kovtun, D. T. Son, and A. O. Starinets, Phys. Rev. Lett. **94**, 111601 (2005), hep-th/0405231.
- [5] *Energy loss and flow of heavy quarks in Au + Au collisions at $\sqrt{s_{NN}} = 200$ GeV*, A. Adare et al. (PHENIX), Phys. Rev. Lett. **98**, 172301 (2007a), nucl-ex/0611018.
- [6] *Disappearance of back-to-back high p_T hadron correlations in central Au + Au collisions at $s_{NN} = 200$ GeV*, C. Adler et al. (STAR), Phys. Rev. Lett. **90**, 082302 (2003), nucl-ex/0210033.
- [7] *Indications of Conical Emission of Charged Hadrons at RHIC*, B. I. Abelev et al. (STAR) (2008), 0805.0622.
- [8] *Quantitative Constraints on the Opacity of Hot Partonic Matter from Semi-Inclusive Single High Transverse Momentum Pion Suppression in Au+Au collisions at $\sqrt{s_{NN}} = 200$ GeV*, A. Adare et al. (PHENIX), Phys. Rev. **C77**, 064907 (2008), 0801.1665.
- [9] *Direct observation of dijets in central Au + Au collisions at $s(NN)^{1/2} = 200$ -GeV*, J. Adams et al. (STAR), Phys. Rev. Lett. **97**, 162301 (2006), nucl-ex/0604018.
- [10] *Scaling of transverse energies and multiplicities with atomic number and energy in ultrarelativistic nuclear collisions*, K. J. Eskola, K. Kajantie, P. V. Ruuskanen, and K. Tuominen, Nucl. Phys. **B570**, 379 (2000), hep-ph/9909456.
- [11] *Hadron multiplicities, p_T spectra and net-baryon number in central Pb + Pb collisions at the LHC*, K. J. Eskola, H. Honkanen, H. Niemi, P. V. Ruuskanen, and S. S. Rasanen (2007), 0705.1770.
- [12] *Hard probes in heavy ion collisions at the LHC: Jet physics*, A. Accardi et al. (2004), CERN Yellow Report CERN-2004-009, hep-ph/0310274.
- [13] *Medium modification of jet shapes and jet multiplicities*, C. A. Salgado and U. A. Wiedemann, Phys. Rev. Lett. **93**, 042301 (2004), hep-ph/0310079.

- [14] *Modified fragmentation function and jet quenching at RHIC*, X.-N. Wang, Nucl. Phys. **A702**, 238 (2002), hep-ph/0208094.
- [15] *Simulation of jet quenching and high- p_T particle production at RHIC and LHC*, I. P. Lokhtin, S. V. Petrushanko, A. M. Snigirev, and C. Y. Teplov, PoS **LHC07**, 003 (2006), 0706.0665.
- [16] I.P. Lokhtin, private communication.
- [17] *Drag force in AdS/CFT*, S. S. Gubser, Phys. Rev. **D74**, 126005 (2006), hep-th/0605182.
- [18] *Radiative energy loss and p_T -broadening of high energy partons in nuclei*, R. Baier, Y. L. Dokshitzer, A. H. Mueller, S. Peigne, and D. Schiff, Nucl. Phys. **B484**, 265 (1997), hep-ph/9608322.
- [19] *Heavy Ion Collisions at the LHC - Last Call for Predictions*, e. . Armesto, N. et al., J. Phys. **G35**, 054001 (2008a), 0711.0974.
- [20] *Color Screening Melts Quarkonium*, A. Mocsy and P. Petreczky, Phys. Rev. Lett. **99**, 211602 (2007), 0706.2183.
- [21] *The production of J/ψ in 200-GeV/nucleon Oxygen +Uranium interactions*, C. Baglin et al. (NA38), Phys. Lett. **B220**, 471 (1989).
- [22] *Heavy Ion Physics with the ATLAS Detector* (2004), ATLAS Collaboration, LHCC 2004-009I-013.
- [23] *A detailed study of high- p_T neutral pion suppression and azimuthal anisotropy in Au + Au collisions at $\sqrt{s_{NN}} = 200$ GeV*, S. S. Adler et al. (PHENIX), Phys. Rev. **C76**, 034904 (2007a), nucl-ex/0611007.
- [24] *Modifications to di-jet hadron pair correlations in Au + Au collisions at $\sqrt{s_{NN}} = 200$ GeV*, S. S. Adler et al. (PHENIX), Phys. Rev. Lett. **97**, 052301 (2006a), nucl-ex/0507004.
- [25] *Two particle azimuthal correlations at high transverse momentum in Pb - Au at 158-A GeV/c*, M. Ploskon (CERES), Nucl. Phys. **A783**, 527 (2007), nucl-ex/0701023.
- [26] *Two- and three-particle azimuthal correlations of high- p_T charged hadrons in Pb+Au collisions at 158-A GeV/c*, S. Kniege and M. Ploskon (CERES), J. Phys. **G34**, S697 (2007), nucl-ex/0703008.
- [27] *ATLAS Technical Design Report Volume 1* (1997), ATLAS Collaboration, LHCC 97-16.
- [28] *Simultaneous pattern recognition and track fitting by the Kalman filtering method*, P. Billoir and S. Qian, Nucl. Instrum. Meth. **A294**, 219 (1990).
- [29] *Measuring the pseudo-rapidity density and transverse momentum spectrum of charged particles at $\sqrt{s} = 14$ TeV*, M. Leyton (ATLAS) (2007), ATLAS Note, ATL-COM-PHYS-2007-051.
- [30] *Zero Degree Calorimeters for ATLAS* (2007), CERN/LHCC/2007-001.
- [31] *Eccentricity fluctuations and elliptic flow at RHIC*, R. S. Bhalerao and J.-Y. Ollitrault, Phys. Lett. **B641**, 260 (2006), nucl-th/0607009.
- [32] *Incident-energy and system-size dependence of directed flow*, G. Wang, J. Phys. **G34**, S1093 (2007), nucl-ex/0701045.

- [33] *Probing small x parton densities in ultraperipheral $A+A$ and $p+A$ collisions at the LHC*, M. Strikman, R. Vogt, and S. White, Phys. Rev. Lett. **96**, 082001 (2006), hep-ph/0508296.
- [34] *Multiplicity distributions for jet parton showers in a medium*, N. Borghini and U. A. Wiedemann, Nucl. Phys. **A774**, 549 (2006), hep-ph/0509364.
- [35] *Rapidity and angular distributions of charged secondaries according to the hydrodynamical model of particle production*, P. Carruthers and M. Doung-van, Phys. Rev. **D8**, 859 (1973).
- [36] *Entropy production at high energy and $\mu(B)$* , P. Steinberg, PoS **CPOD2006**, 036 (2006), nucl-ex/0702019.
- [37] *Charged-particle pseudorapidity distributions in $Au + Au$ collisions at $\sqrt{s_{NN}} = 62.4$ GeV*, B. B. Back et al. (PHOBOS), Phys. Rev. **C74**, 021901 (2006a), nucl-ex/0509034.
- [38] *Centrality and energy dependence of charged-particle multiplicities in heavy ion collisions in the context of elementary reactions*, B. B. Back et al. (PHOBOS), Phys. Rev. **C74**, 021902 (2006b).
- [39] *The significance of the fragmentation region in ultrarelativistic heavy ion collisions*, B. B. Back et al., Phys. Rev. Lett. **91**, 052303 (2003), nucl-ex/0210015.
- [40] *Importance of Correlations and Fluctuations on the Initial Source Eccentricity in High-Energy Nucleus-Nucleus Collisions*, B. Alver et al., Phys. Rev. **C77**, 014906 (2008), 0711.3724.
- [41] *Differential elliptic flow prediction at the LHC from parton transport*, D. Molnar (2007), 0707.1251.
- [42] *HIJING 1.0: A Monte Carlo program for parton and particle production in high-energy hadronic and nuclear collisions*, M. Gyulassy and X.-N. Wang, Comput. Phys. Commun. **83**, 307 (1994a), nucl-th/9502021.
- [43] *Geant4 - a simulation toolkit*, S. Agostinelli et al., Nucl. Instr. Meth. **A506**, 250 (2003).
- [44] *Glauber modeling in high energy nuclear collisions*, M. L. Miller, K. Reygers, S. J. Sanders, and P. Steinberg (2007), nucl-ex/0701025.
- [45] *Charged particle multiplicity near mid-rapidity in central $Au+Au$ collisions at $\sqrt{s_{NN}} = 56$ and 130 GeV*, B. B. Back et al. (PHOBOS), Phys. Rev. Lett. **85**, 3100 (2000).
- [46] *ATLAS Experiment at the CERN Large Hadron Collider*, G. Aad et al. (ATLAS), JINST **3**, S08003 (2008).
- [47] *Methods for analyzing anisotropic flow in relativistic nuclear collisions*, A. M. Poskanzer and S. A. Voloshin, Phys. Rev. **C58**, 1671 (1998), nucl-ex/9805001.
- [48] *Measurement of collective flow in heavy-ion collisions using particle-pair correlations*, S. Wang et al., Phys. Rev. **C44**, 1091 (1991).
- [49] *Flow measurements via two-particle azimuthal correlations in $Au + Au$ collisions at $\sqrt{s_{NN}} = 130$ GeV*, K. Adcox et al. (PHENIX), Phys. Rev. Lett. **89**, 212301 (2002a), nucl-ex/0204005.

- [50] *Analysis of anisotropic flow with Lee-Yang zeroes*, N. B. R. S. Bhalerao and J.-Y. Ollitrault, Nucl. Phys. **A727**, 373 (2003).
- [51] *Genuine collective flow from Lee-Yang zeroes*, N. B. R. S. Bhalerao and J.-Y. Ollitrault, Phys. Lett. **B580**, 157 (2004).
- [52] *Flow analysis from multiparticle azimuthal correlations*, P. M. D. N. Borghini and J.-Y. Ollitrault, Phys. Rev. **C64**, 054901 (2001).
- [53] *Multiple collisions and induced gluon Bremsstrahlung in QCD*, M. Gyulassy and X.-n. Wang, Nucl. Phys. **B420**, 583 (1994b), nucl-th/9306003.
- [54] *Jets as a Probe of Quark Gluon Plasma*, D. A. Appel, Phys. Rev. **D33**, 717 (1986).
- [55] *Suppression of hadrons with large transverse momentum in central Au + Au collisions at $\sqrt{s_{NN}} = 130$ GeV*, K. Adcox et al. (PHENIX), Phys. Rev. Lett. **88**, 022301 (2002b), nucl-ex/0109003.
- [56] *Reaction operator approach to non-Abelian energy loss*, M. Gyulassy, P. Levai, and I. Vitev, Nucl. Phys. **B594**, 371 (2001), nucl-th/0006010.
- [57] *Mach cones and dijets: Jet quenching and fireball expansion dynamics*, T. Renk (2006), hep-ph/0608333.
- [58] *High transverse momentum η meson production in p+p, d+Au and Au+Au collisions at $\sqrt{s_{NN}} = 200$ GeV*, S. S. Adler et al. (PHENIX), Phys. Rev. **C75**, 024909 (2007b), nucl-ex/0611006.
- [59] *Evidence from d + Au measurements for final-state suppression of high p_T hadrons in Au + Au collisions at RHIC*, J. Adams et al. (STAR), Phys. Rev. Lett. **91**, 072304 (2003), nucl-ex/0306024.
- [60] *Jet properties from dihadron correlations in p + p collisions at $\sqrt{s} = 200$ GeV*, S. S. Adler et al. (PHENIX), Phys. Rev. **D74**, 072002 (2006b), hep-ex/0605039.
- [61] *Testing AdS/CFT Drag and pQCD Heavy Quark Energy Loss*, W. A. Horowitz and M. Gyulassy (2008), 0804.4330.
- [62] *Transverse momentum and centrality dependence of high-pt non-photonic electron suppression in Au+Au collisions at $\sqrt{s_{NN}} = 200$ GeV*, B. I. Abelev et al. (STAR), Phys. Rev. Lett. **98**, 192301 (2007), nucl-ex/0607012.
- [63] *Heavy quark colorimetry of QCD matter*, Y. L. Dokshitzer and D. E. Kharzeev, Phys. Lett. **B519**, 199 (2001), hep-ph/0106202.
- [64] *Collective Flow signals the Quark Gluon Plasma*, H. Stoecker, Nucl. Phys. **A750**, 121 (2005), nucl-th/0406018.
- [65] *Conical flow induced by quenched QCD jets*, J. Casalderrey-Solana, E. V. Shuryak, and D. Teaney, J. Phys. Conf. Ser. **27**, 22 (2005), hep-ph/0411315.

- [66] *System size and energy dependence of jet-induced hadron pair correlation shapes in Cu + Cu and Au + Au collisions at $\sqrt{s_{NN}} = 200$ GeV and 62.4 GeV*, A. Adare et al. (PHENIX), Phys. Rev. Lett. **98**, 232302 (2007b), nucl-ex/0611019.
- [67] *Two- and three-particle jet correlations from STAR*, J. G. Ulery (STAR), Nucl. Phys. **A774**, 581 (2006), nucl-ex/0510055.
- [68] *Identification of exotic jet topologies via three particle correlations in PHENIX*, N. N. Ajitanand (PHENIX), Acta Phys. Hung. **A27**, 197 (2006), nucl-ex/0511029.
- [69] *Near-side $\Delta\eta$ correlations of high- p_T hadrons from STAR*, J. Putschke (STAR), AIP Conf. Proc. **842**, 119 (2006).
- [70] *High p_T Triggered $\Delta\eta, \Delta\phi$ Correlations over a Broad Range in $\Delta\eta$* , E. Wenger (PHOBOS) (2008), 0804.3038.
- [71] *Low- and intermediate- p_T di-hadron distributions in Au + Au collisions at $\sqrt{s_{NN}} = 200$ GeV from STAR*, M. J. Horner (STAR), J. Phys. **G34**, S995 (2007), nucl-ex/0701069.
- [72] *Medium-evolved fragmentation functions*, N. Armesto, L. Cunqueiro, C. A. Salgado, and W.-C. Xiang, JHEP **02**, 48 (2008b), arXiv 0710.3073.
- [73] *HIJING: A Monte Carlo model for multiple jet production in p+p, p+A and A+A collisions*, X.-N. Wang and M. Gyulassy, Phys. Rev. **D44**, 3501 (1991).
- [74] *Jets from Quantum Chromodynamics*, G. Sterman and S. Weinberg, Phys. Rev. Lett. **39**, 1436 (1977).
- [75] *QCD studies using a cone based jet finding algorithm for $e^+ + e^-$ collisions at LEP*, R. Akers et al. (OPAL), Z. Phys. **C63**, 197 (1994).
- [76] *Experimental Investigation of the Energy Dependence of the Strong Coupling Strength*, S. Bethke et al. (JADE), Phys. Lett. **B213**, 235 (1988).
- [77] *Longitudinally invariant k_T clustering algorithms for hadron hadron collisions*, S. Catani, Y. L. Dokshitzer, M. H. Seymour, and B. R. Webber, Nucl. Phys. **B406**, 187 (1993).
- [78] *Successive combination jet algorithm for hadron collisions*, S. D. Ellis and D. E. Soper, Phys. Rev. **D48**, 3160 (1993), hep-ph/9305266.
- [79] *FastJet: Dispelling the N^3 myth for the k_T jet-finder*, M. Cacciari (2006), hep-ph/0607071.
- [80] *PYTHIA 6.3: Physics and manual*, T. Sjostrand, L. Lonnblad, S. Mrenna, and P. Skands (2003), hep-ph/0308153.
- [81] ATLAS offline reconstruction and analysis environment (Athena), version 12.0.6.
- [82] *Prompt Photon Production at Large p_T Scheme Invariant QCD Predictions and Comparison with Experiment*, P. Aurenche, R. Baier, M. Fontannaz, and D. Schiff, Nucl. Phys. **B297**, 661 (1988).
- [83] *Energy loss of leading hadrons and direct photon production in evolving quark-gluon plasma*, S. Turbide, C. Gale, S. Jeon, and G. D. Moore, Phys. Rev. **C72**, 014906 (2005), hep-ph/0502248.

- [84] *ATLAS high-level trigger, data acquisition and controls: Technical design report*, CERN-LHCC-2003-022.
- [85] *ATLAS first-level trigger: Technical design report*, CERN-LHCC-98-14.
- [86] *The LHC as a Nucleus-Nucleus Collider*, J. Jowett, plenary talk at the Quark Matter 2008 conference (2008).
- [87] *Hard scattering cross sections at LHC in the Glauber approach: From $p+p$ to $p+A$ and $A+A$ collisions*, D. G. d'Enterria (2003), nucl-ex/0302016.